

Advances in Terahertz Frequency Combs

by

Robert A. Stead

MSci, Imperial College, London, 2004

A THESIS SUBMITTED IN PARTIAL FULFILLMENT OF
THE REQUIREMENTS FOR THE DEGREE OF

DOCTOR OF PHILOSOPHY

in

The Faculty of Graduate Studies

(Physics)

THE UNIVERSITY OF BRITISH COLUMBIA

(Vancouver)

October 2012

© Robert A. Stead 2012

Abstract

Following a review of the theory of terahertz generation via optical rectification in nonlinear crystals, a method for enhancing the nonlinear conversion efficiency of this process is proposed. A nonlinear crystal is placed at the intracavity focus of a passive optical resonator, which is seeded by an ytterbium-doped fibre laser. Models of this arrangement indicate that an enhancement of the optical field of several orders of magnitude is possible. As the difference frequency radiation produced through the optical rectification process results from a mixing of the spectral components of the optical field, one expects a corresponding increase in the terahertz field. We present a design of optical resonator that compensates for the large group velocity dispersion of the nonlinear crystal. Our experimental results indicate that below bandgap absorption in the crystal severely limits the resulting enhancement of the optical field, and hence the terahertz field one would expect from this nonlinear process. A scanning-delay terahertz time-domain spectrometer has been constructed, using a gallium phosphide guiding structure to increase the interaction length of the optical and terahertz fields, thereby increasing the terahertz power produced. Our experiment demonstrates 20 dB signal to noise ratio over the spectral range of 0.5-1 THz. We propose a method for increasing the spectral resolution, whilst simultaneously reducing the required data acquisition time of such a terahertz spectrometer, through the use of two femtosecond optical frequency combs. One of these fields drives the nonlinear optical rectification process, whilst the second serves as a sampling local oscillator field to probe the terahertz field via electro-optic sampling in a second nonlinear crystal. By precisely controlling the relative pulse repetition rates of the two oscillators, we show that the full spectral content of the terahertz field can be acquired at rf

Abstract

frequencies, and without the slow mechanical delay lines associated with conventional terahertz time-domain spectroscopy. Finally, we present experimental efforts towards the demonstration of this technique, and show that, to be effective, steps must be taken to increase the strength of the expected rf signal over that of the measurement noise floor.

Preface

The initial proposal for the cavity-enhanced terahertz generation was devised by David J. Jones, with initial modelling and calculations performed by Jesse C. Petersen. I developed the modelling work to produce the results of section 3.3.3, and this led to the design of the optical cavity presented in section 3.3. The method for coupling the terahertz radiation out of the non-linear crystal was developed by Jesse C. Petersen. I was responsible for the experimental effort and results presented in sections 3.4 through 3.9. The single-comb terahertz spectroscopy work presented in Chapter 4 was entirely my own effort, and this was used as a precursor to the dual-comb work presented later in Chapter 6. The initial concept for the heterodyne detection scheme presented in Chapter 5 was my own work, but benefited greatly from discussions with David J. Jones and Arthur K. Mills. This formed the basis of work presented by David J. Jones at an invited talk of the 2010 March Meeting of the American Physical Society, entitled “Multi-frequency THz Heterodyne Spectroscopy Using Electro-optic Sampling.” This work was then subsequently developed and forms the basis of discussions included in Chapter 5. I performed all modelling and calculations presented. This more detailed analysis has been accepted for publication as Robert A. Stead, Arthur K. Mills, and David J. Jones. “Method for High Resolution and Wide Band Spectroscopy in the Terahertz and Far-Infrared Region”, *Journal of the Optical Society of America B*. The manuscript and discussions contained within were prepared in conjunction with the co-authors. Finally, the experimental efforts of Chapter 6 were performed by myself, save for the design and fabrication of the bandwidth-limited balanced photodetector presented in Appendix A, which was designed and built by Pavel Trochtchanovitch, to specifications provided by David J. Jones.

Table of Contents

Abstract	ii
Preface	iv
Table of Contents	v
List of Tables	ix
List of Figures	x
Acknowledgements	xvi
1 Introduction	1
1.1 Motivation	1
1.1.1 Terahertz Spectroscopy	1
1.1.2 The Terahertz Gap	3
1.1.3 Frequency Comb Spectroscopy	5
1.2 Outline of Thesis	5
2 Background	8
2.1 Optical Rectification	8
2.1.1 Calculation of the Radiated Field	13
2.2 Beam Polarisation and Crystal Orientations	17
2.3 Phase-matching	21
2.4 Lasers	25
2.4.1 Oscillator Design	25

Table of Contents

2.4.2	Compensation of Pulse Chirp due to Dispersion of Fibre Components	28
2.4.3	Pump Diode Line Noise	33
3	Use of a Passive Enhancement Cavity for High Efficiency Terahertz Generation	37
3.1	Cavity Basics	37
3.2	Amplification of a Femtosecond Optical Comb Using a Passive Enhancement Cavity	42
3.3	Cavity Design	48
3.3.1	Mirror Choice and Dispersion Compensation	48
3.3.2	Terahertz Output Coupling	53
3.3.3	Cavity Performance Calculations	55
3.4	Cavity Locking	61
3.5	Spatial Mode-matching into the Optical Resonator	68
3.5.1	Gaussian Mode of the Optical Resonator	68
3.5.2	Beam Profiling	70
3.5.3	Mode-matching Solution	71
3.6	Characterisation of the Passive Enhancement Cavity - Results and Analysis	72
3.7	Measurement of the Cavity Finesse	73
3.7.1	Results of Finesse Measurements	76
3.8	Enhancement Bandwidth of the Cavity	77
3.9	Linear Optical Loss of Gallium Phosphide	84
3.9.1	Loss Mechanisms in Gallium Phosphide	87
3.9.2	Characterisation of the Spectral Absorption of Gallium Phosphide	90
3.10	Conclusions on the use of a Passive Enhancement Cavity for High Efficiency Generation of Terahertz Radiation	92
4	A Single Comb Terahertz Time-domain Spectrometer with Detection Using Conventional Electro-optic Sampling	96
4.1	Introduction	96

Table of Contents

4.2	Experimental Arrangement	97
4.3	Detection of the Terahertz Frequency Comb via Electro-optic Sampling	101
4.3.1	The Linear Electro-optic Effect	101
4.3.2	Comparison of Detection Schemes	109
4.4	Results of Single Comb Detection Scheme	112
4.4.1	Signal Scaling with Optical Probe Power	115
4.5	Conclusions	115
5	Dual-comb Spectroscopy in the Terahertz and Far-IR Region	119
5.1	Introduction	119
5.2	Mapping of a Terahertz Frequency Comb to the Radio Frequency Spectral Region via Asynchronous Electro-optic Sampling	123
5.3	Effect of Spectral Phase on Heterodyne Beat Signal	135
5.4	Effect of Phase-matching on the Heterodyne Beat Signal	139
5.5	Bandwidth and Choice of Detuning	144
5.6	Signal to Noise Scaling	146
6	Experimental Demonstration of Dual-comb Terahertz Spectroscopy	148
6.1	Coupling of Detuned Local Oscillator Pulse	148
6.2	Controlling The Laser Repetition Rates	149
6.2.1	RF Locking Scheme	149
6.2.2	Component Testing and Characterisation	152
6.3	Cross Correlation of Laser Pulses to Verify Timing Jitter	156
6.4	Schemes for Detection of the Heterodyne Beat	161
6.4.1	High Gain Balanced Detector With High Extinction of Frequencies Greater than 80 MHz	161
6.4.2	RF Heterodyne Detection Using VCO Reference	164
6.5	Results and Conclusions from Dual-comb Spectroscopy Measurement	169

Table of Contents

7 Final Conclusions 175

Bibliography 177

Appendices

A Technical Information Regarding High Gain, Low-pass Filtered, Balanced Detector for Detection of the Heterodyne Beat in the Dual-comb Spectrometer Setup 188

List of Tables

3.1	Part numbers and specifications for Layertec mirrors used in the design of the passive enhancement cavity.	53
3.2	Properties of a Gaussian beam	68
3.3	Optical enhancement, resonant bandwidths, and net cavity dispersions for various cavity configurations used to verify the effect of dispersion on the available enhancement.	81
3.4	Thermal properties of gallium phosphide.	87

List of Figures

1.1	Terahertz transitions of some simple molecules.	2
1.2	Major transitions of the water vapour molecule in the spectral region 0.5 to 1.5 THz.	3
2.1	Time and domain descriptions of a mode-locked laser oscillator.	11
2.2	Decomposition of material response to pulsed radiation into sum and difference frequency terms.	12
2.3	DFG for the case of a frequency comb input.	13
2.4	Growth of the difference frequency field, $E_2(z)$ with propagation distance for the case of perfect phase-matching, $\Delta k = 0$.	17
2.5	Coordinate system used for deriving the optimum optical beam orientation for terahertz generation.	19
2.6	Relative nonlinear polarisation as a function of incidence angle, ϕ , and azimuthal angle, α	20
2.7	Dimensions, cuts, and orientation of gallium phosphide crystal for enhancement cavity work.	21
2.8	Variation of refractive index throughout the optical and terahertz spectral ranges, along with an experimental fit of the effective refractive index for optical wavelengths, as per equation 2.33	23
2.9	Coherence length for terahertz frequency generation via optical rectification in gallium phosphide, as predicted by equation 2.34.	24
2.10	Design of the two mode-locked ytterbium fibre lasers.	27

List of Figures

(a)	Laser oscillator design used to provide the high-power (following two subsequent amplification stages) pulses for both the cavity work and the single-comb, terahertz time-domain spectroscopy work described later.	27
(b)	Laser oscillator design used to provide the local oscillator pulses for the work described in Chapter 6.	27
2.11	Configuration of the diffraction grating pulse compressor used for dispersion compensation.	31
2.12	Typical autocorrelation trace of the laser output pulse of the pump laser following compression.	32
2.13	Comparison of modulation sidebands on the optical pulse train repetition rate of 104.3 MHz following the high-power amplifier stage with the controller in its original configuration, and following modifications to allow the regulation of the transistor control voltage with an external linear dc supply.	34
2.14	Comparison of noise on the electrical current used to drive the Apollo Instruments pump diode, as measured across a shunt resistor.	35
2.15	Schematic of the Apollo Instruments laser diode driver, model no. D-560.	36
3.1	A simple two-mirror optical resonator.	39
3.2	Resonant modes of an optical resonator.	41
3.3	Varying overlap of the resonant modes of the passive enhancement cavity with the longitudinal modes of the mode-locked laser used as the seed.	45
3.4	Resonance map of a dispersion-free enhancement cavity.	47
3.5	Resonance map for a passive enhancement cavity exhibiting a large net group velocity dispersion.	49
3.6	Experimental arrangement for the passive enhancement cavity.	50
3.7	Refractive Index and dispersion of gallium phosphide as predicted by the Sellmeier equation.	52
3.8	Crystal geometry for output coupling of the terahertz radiation.	54

List of Figures

3.9	Optical design for output coupling of terahertz radiation for a gallium phosphide crystal at Brewster incidence.	56
3.10	Effective enhancement of the range of optical frequencies effectively coupled into the enhancement cavity for various input couplers.	59
3.11	Calculated residual GDD of the cavity components for the cavity configuration shown in figure 3.6.	60
3.12	Estimated broadening of a 200 fs input optical input pulse within a passive enhancement cavity of the same design of that used in figure 3.10.	60
3.13	Circulating pulse energy enhancement and duration as a function of input coupler reflectivity for the cavity configuration of 3.12.	61
3.14	The reflection signal measured from the enhancement cavity near a position of resonance.	63
3.15	Calculated error signal for a passive enhancement cavity having a finesse of $\mathcal{F} = 2 \times 10^5$	66
3.16	Beam waist (radius) profile following a 250 mm focal length converging lens.	71
3.17	Schematic of optics used for mode-matching into the passive enhancement cavity.	73
3.18	Ring down measurement for the passive enhancement cavity without the gallium phosphide crystal, the cavity having a predicted finesse of $\simeq 960$	77
3.19	Ring down measurement for the passive enhancement cavity without the gallium phosphide crystal, the cavity having a predicted finesse of $\simeq 1800$	78
3.20	Intracavity enhancement for varying amounts of residual GDD.	83
3.21	Optical spectra supported by the passive enhancement cavity with the gallium phosphide crystal placed at the intracavity focus.	84

List of Figures

3.22	Variation of the voltage bias applied to the piezoelectric actuator (PZT) as a function of time following locking of the enhancement cavity.	86
3.23	Effect of parasitic loss on the optimal enhancement factor that can be obtained from a passive enhancement cavity. . . .	88
3.24	Average power transmitted through the gallium phosphide crystal as a function of incident average power.	89
3.25	Spectral absorption of gallium phosphide.	91
3.26	Maximum possible enhancement factor provided by an impedance-matched enhancement cavity containing a nonlinear crystal having absorption coefficient, $\alpha = 0.5 \text{ cm}^{-1}$ and varying length.	94
4.1	Experimental arrangement of single-comb terahertz time-domain spectrometer	100
4.2	Beam propagation in the gallium phosphide waveguide structure.	101
4.3	Crystal geometry for the electro-optic detection scheme. . . .	105
4.4	Deformation of the two-dimensional refractive index ellipsoid in the (110) crystal plane.	107
4.5	Time-domain electro-optic sampling (EOS) traces of the generated terahertz field	113
	(a) Electro-optic sampling trace with single channel detector	113
	(b) Electro-optic sampling trace acquired using balanced detection scheme.	113
4.6	Resulting time-domain EOS traces for varying average powers of the optical probe pulse.	116
4.7	Scaling of the peak photocurrent observed from the single channel electro-optic sampling apparatus as a function of average power of the optical pulse.	117
5.1	Overview of the multi-frequency heterodyne detection scheme for the dual-comb terahertz spectrometer.	122

List of Figures

5.2	Schematic of a terahertz spectrometer where the pump femtosecond frequency comb (FFC) and local oscillator (LO FFC) frequency combs differ in pulse repetition rate by an amount Δf_{rep}	124
5.3	Frequency components [produced through mixing of the terahertz frequency comb with the detuned LO comb.	132
5.4	Effect of various spectral phase contributions on the expected signal magnitude predicted by equation 5.23.	140
5.5	Variation of phase and amplitude of A-EOS sidebands as a function of optical wavelength for a ZnTe detection crystal of 0.4 mm length.	142
5.6	Variation of phase and amplitude of A-EOS sidebands as a function of optical wavelength for a ZnTe detection crystal of 0.8 mm length.	142
5.7	Variation of phase and amplitude of A-EOS sidebands as a function of optical wavelength for a ZnTe detection crystal of 1.6 mm length.	143
5.8	Calculated heterodyne beat signal for a THz frequency of 0.85 THz, as a function of nonlinear crystal length for a ZnTe detection crystal, and an LO FFC of 7 nm bandwidth, centred at 1030 nm.	144
5.9	Map of the expected bandwidth performance one can reasonably expect from the dual-comb terahertz spectrometer system for given constraints in oscillator design and acquisition methods.	145
6.1	Experimental arrangement of the dual-comb terahertz spectrometer	150
6.2	Schematic of the rf locking scheme used to control the pulse repetition rates of the two lasers.	151
6.3	Arrangement for measuring of the noise floor of the available low frequency mixers.	153

List of Figures

6.4	Measured noise floors for the three available low frequency mixers.	154
6.5	Spectrum of the residual noise on the error signal for the range of high frequency mixers available.	155
6.6	Pulse trains from two lasers, with pulse repetition rates $f_{rep,1}$ and $f_{rep,2} = f_{rep,1} + \Delta f_{rep}$	157
6.7	Experimental arrangement for the cross-correlation measurement.	158
6.8	Cross-correlation trace of the femtosecond optical combs in β -BBO with the repetition rate detuning set to 400 Hz.	159
6.9	RF spectral output for the cross-correlation measurement depicted in figure 6.7.	160
6.10	Output of the custom-designed balanced detector for a typical balanced input with additional external amplification.	162
6.11	Noise spectrum for the high-speed balanced detector used for detection of the heterodyne beat signal.	163
6.12	Schematic of the rf circuitry used to provide a reference signal at the expected rf heterodyne beat frequency.	166
6.13	Circuit schematic for the active filter used to lock the voltage control oscillator (VCO) to the expected frequency of the heterodyne beat signal.	167
6.14	Measured residual noise level on the VCO control signal for locking of the VCO to the detuning and a reference oscillator.	168
A.1	Circuit schematic of the custom-designed, bandwidth-limited balanced photodetector.	189

Acknowledgements

I would like to first thank Professor David Jones for taking me into his research group and providing me with the opportunity to learn from him over the course of my studies. I am sure many other graduate students would be envious of having a supervisor who spends so much time in the lab, and who makes himself so accessible for discussions regarding ideas and problems.

In addition, I owe a great deal of thanks to Arthur Mills, whose seemingly endless time, patience and enthusiasm were invaluable throughout my time at UBC. Art never failed to offer insightful input, regardless of the subject material! My gratitude also goes to Jie Jang, another Post-doc whom I had the pleasure of working with in the initial part of my research at UBC. Jie's magic touch when it came to lasers never ceased to amaze me. Thank you also to Jesse Petersen, who completed his Ph.D at Simon Fraser University shortly after I began my research, and who provided many interesting technical discussions and ideas regarding the cavity enhanced terahertz generation work. Thanks too to Professor Steve Dodge, who supervised Jesse and invited me to visit their lab to see their terahertz spectrometer system in action. I am also grateful to Mario Beaudoin who kindly offered the use of his spectrometer setup for measurement of the band-gap edge profile of gallium phosphide, and who provided useful input on the topic of absorption mechanisms.

Of course, my time at UBC was made all the more enjoyable thanks to the company of the other students I had the good fortune to work with. TJ Hammond, whose experiences and frustrations always served as an indicator of what I could look forward to, as well as encouraging me that there is, indeed, light at the end of the tunnel! Thank you also to Matt Lam, with

Acknowledgements

whom I shared many interesting discussions, and had the pleasure of working alongside during many teaching assignments.

I would like to thank the many project students and undergraduate students I had the opportunity to engage with during my time at UBC. Your enthusiasm and thirst for knowledge were a constant source of inspiration, and I sincerely hope that I was able to inspire in return, as well as offer counsel on research and life as a postgraduate student.

Finally, thank you to my friends and family for your patience, understanding and encouragement. I consider myself incredibly lucky to have had the support I have enjoyed regardless of the path I choose to pursue.

Chapter 1

Introduction

1.1 Motivation

1.1.1 Terahertz Spectroscopy

Optical spectroscopy is now a well established tool for the characterisation of many chemical substances. Indeed, there exists many spectroscopic techniques, spanning the electromagnetic spectrum from microwave frequencies to extreme ultraviolet and x-ray wavelengths. Recently, there has been much interest in developing spectroscopic tools in the far infra-red (IR) range and at longer wavelengths, in what is commonly referred to as the ‘terahertz gap’, so called due to the in-availability of sources and detectors in this frequency range. Whilst the exact definition of the terahertz gap is often disputed, it is commonly used to refer to frequencies between 1 and 100 THz, or wavelengths between 300 and 3 μm . It is of considerable interest to develop spectroscopic tools in this range, as many molecules exhibit characteristic transitions at terahertz wavelengths. Indeed, lighter molecules and, in particular, those containing carbon-oxygen bonds [1], as well as ammonia and water vapour [2], have been found to have transitions corresponding to rotational and vibrational excited states in the terahertz range. Further, the scaling of the strength of these spectral features as the square or even the cube of the frequency makes the increased sensitivity of terahertz spectroscopy over more established microwave spectroscopy a draw unto itself. The unique nature of the spectroscopic signatures of many molecules in the terahertz range has led to the moniker of the ‘fingerprint range’ when referring to these wavelengths. Terahertz spectroscopy has been shown to be an excellent method for distinguishing molecular structures of otherwise similar

1.1. Motivation

molecules. See, for example, [3].

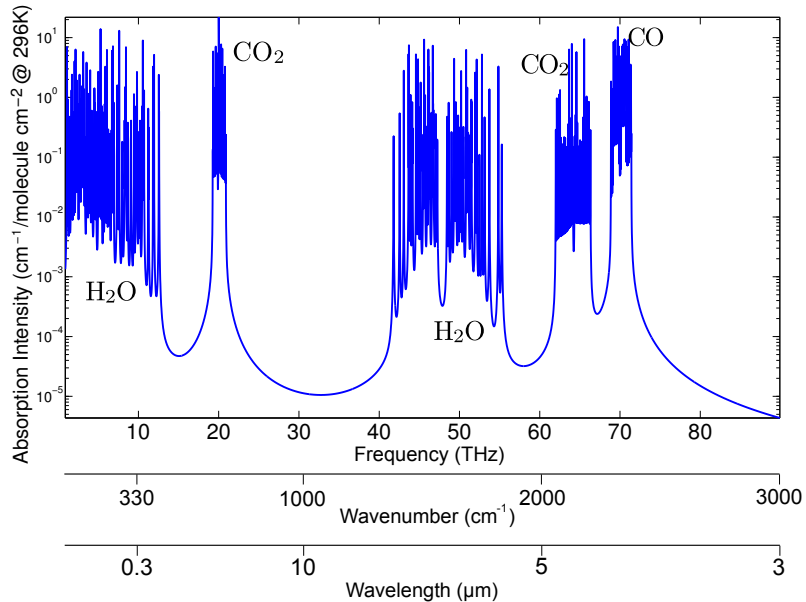


Figure 1.1: Terahertz transitions of some simple molecules [4].

This capability has led to work towards devices capable of remotely identifying and characterising gas leaks and potentially dangerous or noxious gas leaks and plumes, [5], as well as considerable interest in the use of terahertz radiation for detection and characterisation of various drugs and pharmaceutical agents [6], explosives [7],[8], DNA and other materials [9], [10].

Of particular interest to this project is the spectral range 0.5-1.5 THz. Water vapour has some particularly strong molecular transitions in this range, at 1.16 and 1.11 THz. These correspond to rotational molecular transitions [4]. There is currently great interest in the absorption characteristics of water vapour due to its role in atmospheric radiation budgets. Indeed, some studies have attributed up to 50% of the Earth's greenhouse effect to

1.1. Motivation

absorption of THz and far IR radiation [11]. Further, there is also great interest in the use of THz sensing methods for terrain mapping, verification of atmospheric models, and meteorological predictions [12], [13]. In order to develop these tools, a detailed understanding of terahertz propagation in humid air is necessary. See, for example, recent measurements conducted by Grishkowsky et al. [14] using a scanning Fourier transform terahertz spectrometer from 0.2 to 2 THz. Whilst these measurements represent state of the art accuracy, we note for later discussions that the authors state limitations due to the thermal and mechanical stability of the apparatus, as well as long data acquisition times of around three minutes.

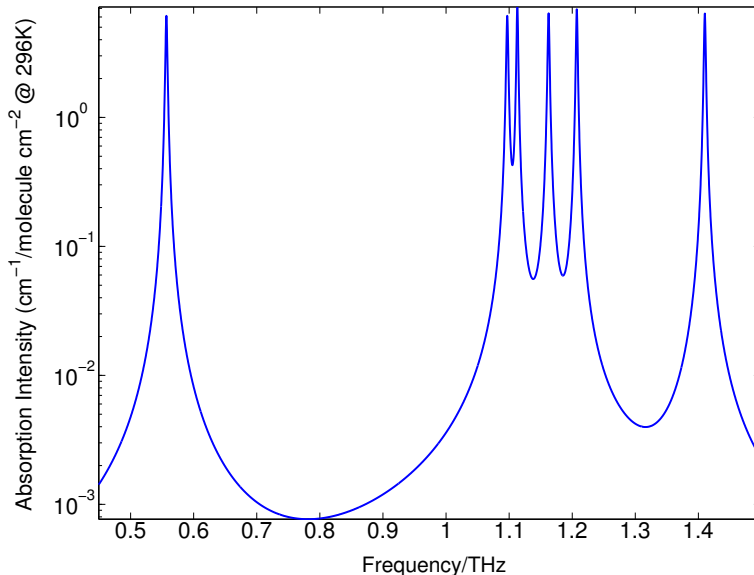


Figure 1.2: Major transitions of the water vapour molecule in the spectral region 0.5 to 1.5 THz. Fitted from data in [4]

1.1.2 The Terahertz Gap

There remains much debate about how best to generate radiation in this wavelength range, at the intersection of spectral regions typically dominated by electronic generation methods, such as Gunn oscillators and Schottky

diodes on the low frequency side, and optical methods, such as semiconductor diodes on the high frequency side. Whilst efforts have been made to extend the capabilities of electronic, radio frequency (rf) methods into the terahertz range, difficulties typically arise due to the limited carrier transit-times, and the simple fact that many of the conventional components used show resistive losses that give rise to high frequency roll-off at terahertz frequencies [5]. Instead, optical approaches have been developed in order to access this difficult wavelength range. Of these, quantum cascade lasers have shown promise in generating high powers. In these devices, photons are emitted by electrons making transitions not across the bandgap, as in conventional semiconductor sources, which are typically limited to frequencies above 15 THz due to the in-availability of materials with smaller bandgaps [15], but between conduction subbands of periodic structures, synthetically grown to give the desired gain characteristics. Whilst quantum cascade lasers have been demonstrated capable of producing up to 250 mW pulsed power [16], operation in the terahertz range usually requires cryogenic cooling due to the scaling of free carrier absorption with the radiation wavelength, as well as practical difficulties in building the quantum well structure [17]. Electro-optic antennas, where a high intensity optical pulse is incident on a semiconductor material, “strained” by a large electrical bias, have also been used, both for the generation and detection of terahertz radiation [18]. Bartels et al. [19] demonstrated a THz time domain spectrometer system using this technique, with a generated THz power of 40 μ W. However, at higher powers, these techniques suffer from saturation effects of the excited carriers. Likewise, the THz bandwidth is limited by the relaxation lifetime of the carriers to around 5 THz [20]. An alternative scheme is that of optical rectification, where an ultrashort, and therefore broadband, optical pulse is focused onto a nonlinear crystal, and difference frequency generation occurs within the bandwidth of the optical pulse. Because this technique is not limited by saturation effects, the advent of high power, femtosecond pulsed fibre lasers has made optical rectification an exciting method for the generation of terahertz radiation for spectroscopy [21].

1.1.3 Frequency Comb Spectroscopy

It has been shown (see, for example, [22]) that the output of a mode-locked laser can be described in the frequency domain by a comb of evenly spaced frequency elements, with each element being separated from its neighbouring elements by the laser pulse repetition rate. Diddams et al. [23] showed that this frequency comb can be used for high resolution optical spectroscopy. Indeed, these authors were able to record spectra of transitions in iodine vapour with a resolution of $\simeq 330$ MHz, or $\simeq 5 \times 10^{-4}$ nm at 633 nm. Since this work, the benefits of femtosecond comb spectroscopy have been extended into the near-IR spectral region [24],[25] but have yet to be extended to the terahertz region due to the lack of suitable frequency comb sources. Such high spectral resolution is particularly desirable at terahertz frequencies, due to the abundance of rotational molecular transitions in this frequency range, as shown in figure 1.2 for water vapour. Further, the study of vibrational transitions, with their long lifetimes and correspondingly narrow spectral widths would benefit greatly from high spectral resolution at terahertz frequencies, aiding electron dipole moment investigations in molecules such as ThO (895 cm⁻¹) [26] and YbF (501 cm⁻¹) [27].

In this work, we use optical rectification to produce, via difference frequency generation within a broad spectral bandwidth, a terahertz frequency comb. Further, we show that the power of such a frequency comb may be increased for a given driving optical power using resonant enhancement of the optical field. In addition, we show that the resulting comb nature of the terahertz field allows novel detection schemes capable of extending the methods of frequency comb spectroscopy to the terahertz spectral range.

1.2 Outline of Thesis

In order to increase the signal to noise performance of a terahertz frequency comb spectrometer, it is desirable that the incident comb be of high power so as to allow the detection of low intensity absorption features. In this thesis, we begin in Chapter 2 by reviewing the basic principles underlying

terahertz generation via optical rectification. Further, we extend this theory to the case where the optical rectification process is driven by a mode-locked optical frequency comb. In Chapter 3 we consider a method of generating a high-power terahertz frequency comb by increasing the power in the driving optical frequency comb. The enhancement of the optical field is achieved through the use of a passive optical resonator, similar in operating principle to those used to increase the efficiency of other nonlinear optical processes, namely high harmonic generation [28], [29]. The theory of operation of such an enhancement cavity is reviewed before studying the design of the cavity in detail. In particular, the effect of various orders of phase delay on the optical enhancement within the cavity are considered. To this end, we present a scheme for controlling the average resonant frequency of the enhancement cavity, along with methods of compensating for the large group velocity dispersion of the nonlinear crystal used to generate the terahertz field. Performance estimates of the enhancement cavity are made before reviewing experimental measurements of the optical enhancement achieved. Factors limiting the optical enhancement are discussed.

In Chapter 4 we demonstrate a terahertz time-domain spectrometer using free space electro-optic sampling and a swept mechanical delay to vary the overlap of the terahertz field with a sampling optical probe field in a nonlinear detection crystal. In order to enhance the nonlinear conversion efficiency of the terahertz generation process, we use a gallium phosphide waveguide structure to confine the strongly diverging terahertz field to the interaction region of this long crystal. Whilst our experimental arrangement demonstrates good signal to noise over the spectral range of 0.5-1 THz, data acquisition is time consuming due to the need to vary the length of the optical path of the probe field using the mechanical delay. Further, the translating delay line leads to instabilities in alignment, which gives rise to drifts in the time-domain signal.

Chapter 5 outlines in detail a method for high resolution terahertz comb spectroscopy with high speed data acquisition. Instead of a mechanical delay line, the proposed scheme makes use of a heterodyne detection scheme whereby detection of the terahertz frequency comb is performed using an

optical frequency comb differing slightly in pulse repetition rate to that of the terahertz comb. In this sense, we refer to this method as dual-comb terahertz spectroscopy. We show, with a fully frequency domain analysis, that frequency resolution limited only by the relative stability of the laser pulse repetition rates can be achieved. At the same time, the technique is shown to offer data acquisition rates far greater than those of conventional swept delay terahertz time domain spectrometers. Finally, we discuss experimental progress towards implementing this detection scheme in Chapter 6. A method of controlling the repetition rate detuning of the terahertz and sampling optical combs is presented and characterised. Having determined the central frequency and bandwidth of the terahertz field in the work of Chapter 4, several methods of measuring the terahertz frequency comb at the rf heterodyne beat frequency calculated in Chapter 5 are presented and discussed.

Chapter 2

Background

2.1 Optical Rectification

It is well known that the response of a dielectric material to a strong monochromatic optical field can be divided into a linear and a nonlinear portion. More specifically, when driven by a monochromatic, plane wave of the form

$$E(t) = E_0 e^{-i\omega t} + \text{c.c.}, \quad (2.1)$$

the material will exhibit a polarisation given by

$$P(t) = \varepsilon_0 \chi^{(1)} E(t) + \chi^{(2)} E(t)E(t) + \chi^{(3)} E(t)E(t)E(t) + \dots \quad (2.2)$$

where $\chi^{(n)}$ is the n th order nonlinear susceptibility of the medium. Note that, for clarity, we consider only scalar fields and neglect any spatial dependence of the field for the present discussion. In principle, the above relations apply to each vector component of the field and resulting polarisation, in which case the susceptibilities become tensors. See, for example, [30]. The first term in equation 2.2 is the usual linear response, whilst the second and third constitute the second and third order responses respectively. Considering in more detail the second order response to the electric field of equation 2.1, we obtain a second order nonlinear response given by

$$P^{(2)}(t) = (\chi^{(2)} E_0^2 e^{-2i\omega t} + \text{c.c.}) + 2\chi^{(2)} E_0 E_0^*. \quad (2.3)$$

The first of these terms is the commonly recognised sum frequency term, whilst the $E_0 E_0^*$ term represents a contribution at zero frequency, and describes optical rectification. It is this latter term that interests us. Whilst

2.1. Optical Rectification

the above is true for the monochromatic field of equation 2.1, for pulsed radiation with a broadband spectral profile this dc polarisation follows the temporal envelope of the incident optical pulse as shown in figure 2.2, an effect first experimentally detected by Bass et al. in 1962, [31]. To analyse the effect of this optical rectification process on the output pulse train of a mode-locked oscillator, we consider the latter in more detail.

For a mode-locked oscillator, the laser output can be described in the time domain as a train of pulses, of separation $\tau_{rep} = \frac{1}{f_{rep}}$, where f_{rep} is the pulse repetition rate and the duration of each pulse, τ , is assumed to be much less than τ_{rep} . The electric field is of the form of a high frequency carrier wave at the central optical frequency $\omega_c = 2\pi f_c$, modulated by an envelope function which is periodic in τ_{rep} , as shown in figure 2.1. Further, the maxima of the high frequency carrier wave are offset from the maxima of the envelope by a phase ϕ_{ce} , known as the carrier-envelope phase. Following the methodology of [22], the electric field of the pulse train is given by

$$E(t) = \sum_{n=-\infty}^{\infty} \mathcal{E}(t - n\tau_{rep}) e^{i(\omega_c t + n(\Delta\phi_{ce} - \omega_c \tau_{rep}) + \phi_0)}, \quad (2.4)$$

where the infinite limits on n imply that the pulse train contains an infinite number of pulses. In this expression, $\phi_{ce} = n\Delta\phi_{ce} + \phi_0$ is the carrier-envelope phase of the n th pulse, $\Delta\phi_{ce}$ being the pulse-to-pulse carrier-envelope phase shift. $\mathcal{E}(t - n\tau_{rep})$ is the temporal envelope function which, as required, is periodic in τ_{rep} and has a maximum for $t - n\tau_{rep} = 0$. Taking the Fourier transform of this expression, and rearranging, we obtain [22]

$$\begin{aligned} \tilde{E}(\omega) &= \sum_n e^{i(n(\Delta\phi_{ce} - \omega_c \tau_{rep}) + \phi_0)} e^{-i(n\omega - \omega_c)\tau_{rep}} \tilde{E}(\omega - \omega_c) \\ &= e^{i\phi_0} \tilde{E}(\omega - \omega_c) \sum_M \delta(\Delta\phi_{ce} - \omega\tau_{rep} - 2\pi M), \end{aligned} \quad (2.5)$$

where M runs over the frequency bandwidth of the optical pulse. The delta

2.1. Optical Rectification

function in the final term describes a comb of frequency elements at

$$\omega_M = \frac{2M\pi}{\tau_{rep}} - \frac{\Delta\phi_{ce}}{\tau_{rep}}. \quad (2.6)$$

Or, equivalently,

$$f_M = Mf_{rep} + f_0 \quad (2.7)$$

where $f_0 = -\frac{\Delta\phi_{ce}f_{rep}}{2\pi}$ is the offset of the lowest frequency from zero (dc) frequency. The laser spectrum therefore has the form of a comb of evenly-spaced frequencies of spacing f_{rep} with offset from dc by an amount f_0 , determined by the pulse-to-pulse phase-shift, $\Delta\phi_{ce}$, as illustrated in figure 2.1. The time domain expression for the electric field, equation 2.4, can therefore be expressed as a sum of these spectral frequency components as

$$E(t) = \sum_M A(\omega_M) e^{-2\pi i(Mf_{rep} + f_0)t} \quad (2.8)$$

where $A(\omega_M)$ is the complex spectral amplitude of the spectral line at frequency ω_M . In equation 2.8 the sum over M again runs over the entire bandwidth of the optical spectrum.

Having derived an expression for the output of a mode-locked oscillator as a function of time, we now return to our consideration of the nonlinear polarisation of equation 2.3. Substituting equation 2.8 into the optical rectification term of equation 2.3 gives

$$P_{DFG}^{(2)}(t) = \sum_{\substack{M, N=0 \\ N < M}}^{\infty} \chi^{(2)}(\omega_M - \omega_N; \omega_M, \omega_N) A(\omega_M) A^*(\omega_N) e^{-2\pi i(Mf_{rep} + f_0)t} e^{2\pi i(Nf_{rep} + f_0)t}. \quad (2.9)$$

The limits on the sum now arise from assuming there is no contribution to a polarisation at negative frequency, and we assume the same conditions on M and N in the expression to follow. Simplifying, and using the fact that

2.1. Optical Rectification

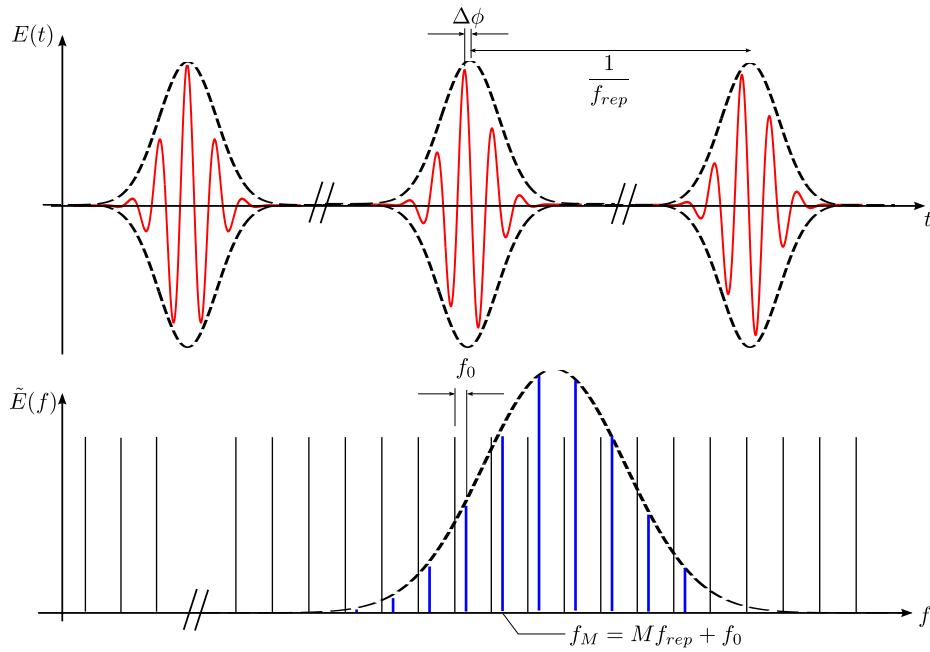


Figure 2.1: The laser pulse train from a mode-locked oscillator can be described in either the time domain (top) or the frequency domain (bottom). In the time domain, the carrier-envelope phase evolves by an amount $\Delta\phi$ between pulses. In the frequency domain, the output of the laser is equivalent to a discrete comb of frequencies, each separated by the laser pulse repetition rate, f_{rep} and offset from zero frequency by an amount $f_0 = \frac{\Delta\phi f_{rep}}{2\pi}$.

2.1. Optical Rectification

$A(\omega)$ is real:

$$P_{DFG}^{(2)}(t) = \sum_{M,N} \chi^{(2)}(\omega_M - \omega_N; \omega_M, \omega_N) A(\omega_M) A^*(\omega_N) e^{-2\pi i(M-N)f_{rep}t}. \quad (2.10)$$

Equation 2.10 shows that every frequency component in the input optical

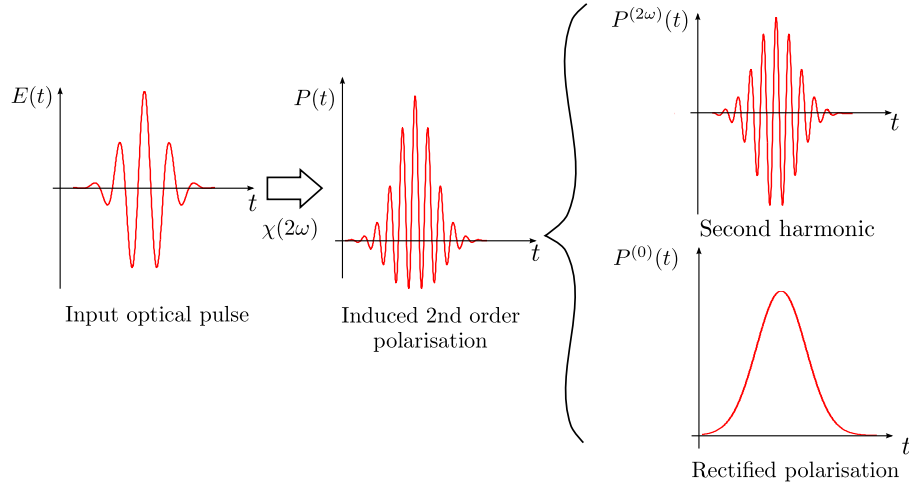


Figure 2.2: Decomposition of material response to pulsed radiation into sum and difference frequency terms. The difference frequency term gives rise to a dc polarisation that will rise and fall with the pulse envelope.

pulse mixes with every other frequency component, producing a comb of difference frequencies at

$$f_{THz} = \sum_{M,N} (M - N) f_{rep}. \quad (2.11)$$

We note that this new comb necessarily has a zero carrier-envelope offset frequency. It is also important to note that, whilst the input frequencies are all entirely in the optical range of frequencies, that is, around 290 THz for optical wavelengths of 1030 nm, the difference frequencies will be centred at dc, and extend out to the bandwidth of the original optical pulse, as shown

2.1. Optical Rectification

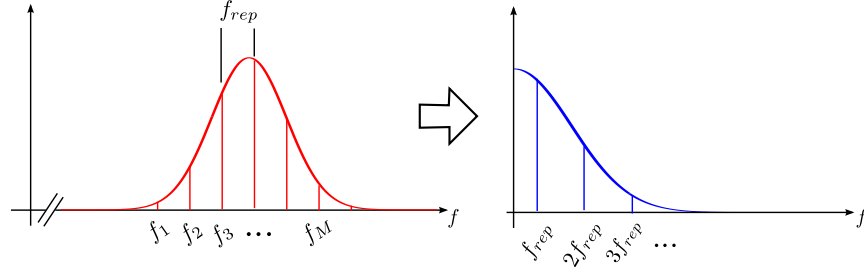


Figure 2.3: DFG for a frequency comb gives rise to a second frequency comb, centred at dc and with a necessarily zero offset frequency.

in figure 2.3.

2.1.1 Calculation of the Radiated Field

In order to determine the power radiated at each of the difference frequencies as a result of the nonlinear polarisation of equation 2.10, we treat each frequency component of the driving optical field as a continuous wave (CW). We then compute the magnitude of the field radiated at each of the resulting difference frequencies using the nonlinear wave equation:

$$\nabla^2 E = \mu_0 \epsilon \frac{\partial^2 E}{\partial t^2} + \mu_0 \frac{\partial^2 P_{NL}}{\partial t^2}, \quad (2.12)$$

where E is the sum of the three field components involved. That is, the mixing components of the driving optical field, and the resulting radiated field due to the nonlinear polarisation component P_{NL} . Away from a resonance, Kleinman symmetry dictates that the second order nonlinear susceptibility, $\chi^{(2)}(\omega_M - \omega_N; \omega_M, \omega_N)$ is independent of frequency. We will see that terahertz generation via optical rectification often relies on some frequencies being near an optical resonance so as to satisfy the condition of phase-matching. Regardless, this approximation is adequate for the purposes of this discussion. In the case of the nonlinear susceptibility being independent of frequency, we use the effective nonlinear coefficient,

2.1. Optical Rectification

$d_{eff} = \frac{1}{2}\chi^{(2)}(\omega_M - \omega_N; \omega_M, \omega_N)$. Further, third and higher order contributions to the nonlinear polarisation are neglected, such that $P_{NL}(t) \simeq P^{(2)}(t) = 2d_{eff}E(t)E^*(t)$. Finally note that, in the semiconductor crystals considered in this work, d_{eff} will vary in magnitude depending on the polarisation of the fields, due to the rotational asymmetry of the crystal lattice.

We consider the generation of a single difference frequency, ω_2 , generated from the nonlinear interaction between two input optical frequencies at ω_1 and ω_3 , with $\omega_2 = \omega_3 - \omega_1$. Further, in order to account for the growth of the difference frequency field with propagation, we include the dependence of the electric field with propagation direction, such that, for the three fields, the field at frequency ω_i is described by

$$E^{\omega_i}(t, z) = E_i e^{-i(\omega_i t - k_i z)} + \text{c.c.} \quad (2.13)$$

where k_i is the magnitude of the wavevector \vec{k}_i of the field E^{ω_i} , and E_i is the complex envelope. By virtue of the fact that E in 2.12 is the sum of the three fields in 2.13, the nonlinear polarisation serves to couple the field amplitudes and it is necessary to find all of the sum and difference frequency components of the nonlinear polarisation, such that we may solve the wave equation. The nonlinear polarisation at the difference frequency $\omega_3 - \omega_1$ is given by

$$P_{NL}^{\omega_3 - \omega_1}(t, z) = d_{eff} E_3 E_1^* e^{i[(\omega_3 - \omega_1)t - (k_3 - k_1)z]} + \text{c.c.} \quad (2.14)$$

Similarly for the other frequency components

$$P_{NL}^{\omega_3 - \omega_2}(t, z) = d_{eff} E_3 E_2^* e^{i[(\omega_3 - \omega_2)t - (k_3 - k_2)z]} + \text{c.c.} \quad (2.15)$$

$$P_{NL}^{\omega_1 + \omega_2}(t, z) = d_{eff} E_3 E_2^* e^{i[(\omega_1 + \omega_2)t - (k_1 + k_2)z]} + \text{c.c.} \quad (2.16)$$

It is these nonlinear polarisations that serve as dipole sources for the radi-

2.1. Optical Rectification

ated difference frequency signal. In order to obtain the set of coupled wave equations, we substitute these expressions into 2.12 and make the slowly varying amplitude approximation,

$$\frac{d^2}{dz^2}E_N \ll k_N \frac{d}{dz}E_N. \quad (2.17)$$

That is to say that the amplitude of any one field varies slowly on the scale of one wavelength. The final result yields

$$\frac{d}{dz}E_1 = -i2\pi \frac{\omega_1^2}{c^2} \frac{1}{k_1} d_{eff} E_3 E_2^* e^{-i(k_3 - k_2 - k_1)z} \quad (2.18)$$

$$\frac{d}{dz}E_2 = -i2\pi \frac{\omega_2^2}{c^2} \frac{1}{k_2} d_{eff} E_1^* E_3 e^{-i(k_3 - k_2 - k_1)z} \quad (2.19)$$

$$(2.20)$$

We now make the assumption of perfect phase-matching such that $\Delta k = k_3 - k_2 - k_1 = 0$ which allows us to drop the exponential dependence. We also make the important assumption of an undepleted pump for the field E^{ω_3} . That is, that d_{eff} is small such that the field amplitude E_3 remains unchanged. This allows us to define the constants

$$\begin{aligned} K_1 &= -2\pi i \frac{\omega_1^2}{c^2} \frac{1}{k_1} d_{eff} E_3 \\ K_2 &= -2\pi i \frac{\omega_2^2}{c^2} \frac{1}{k_2} d_{eff} E_3, \end{aligned} \quad (2.21)$$

such that equation 2.18 and 2.19 can be written

$$\frac{d}{dz}E_1 = K_1 E_2^* \quad (2.22)$$

$$\frac{d}{dz}E_2 = K_2 E_1^* \quad (2.23)$$

$$(2.24)$$

2.1. Optical Rectification

Differentiating and substituting yields

$$\frac{d^2 E_1}{dz^2} = K_1 K_2^* E_1, \quad (2.25)$$

which has the solution

$$E_1(z) = C \sinh(Kz) + D \cosh(Kz), \quad (2.26)$$

where C and D are constants to be determined by boundary conditions, and $K = \sqrt{K_1 K_2^*}$. Substituting this into the expression for E_2 yields

$$E_2(z) = \frac{-K}{K_1^*} [C \cosh(Kz) + D \sinh(Kz)]. \quad (2.27)$$

Applying the boundary condition that the difference frequency field, $E_2(z = 0) = 0$ at the crystal entrance face, so that $C = 0$. The final solution for the difference frequency field is then

$$E_2(z) = -i \frac{E_3}{|E_3|} E_1(0) \sqrt{\frac{k_2 n_1}{k_1 n_2}} \sinh(Kz), \quad (2.28)$$

which can be squared to yield the intensity of the difference frequency field

$$I_2 = [|E_1(0)|^2 \frac{k_2 n_1}{k_1 n_2} \sinh^2(Kz)]. \quad (2.29)$$

For perfect phase-matching, the intensity of the difference frequency field therefore grows exponentially with propagation length, as shown in figure 2.4. The topic of phase-matching will be reserved for section 2.3. For a single pass configuration, it is therefore desirable to use as long a nonlinear crystal as possible. However, typically the condition of perfect phase-matching can only be satisfied for narrow terahertz bandwidths. For broadband generation of terahertz radiation it will be necessary to reduce the crystal length so as to not exceed the propagation length over which the optical and difference frequency fields remain in phase. Further, optimal use of such a nonlinear crystal in an optical resonator requires certain other crystal properties to

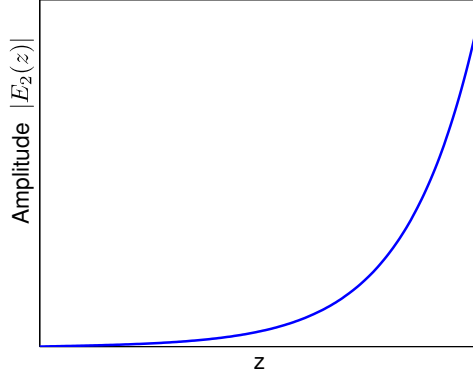


Figure 2.4: Growth of the difference frequency field, $E_2(z)$ with propagation distance for the case of perfect phase-matching, $\Delta k = 0$.

be accounted for, namely, the material dispersion and the symmetry of the crystal lattice. These issues form the basis of the following discussions.

2.2 Beam Polarisation and Crystal Orientations

In order to determine the optimum beam polarisations and crystal orientation so as to maximise the efficiency of terahertz generation, it is necessary to account for the vector nature of the fields in equations 2.14-2.16. We use the notation \vec{E}^{ω_N} to denote the time-dependent field at ω_N . Further, the nonlinear crystals used are in general not isotropic, such that the effective nonlinear optical coefficient, d_{eff} is a tensor that depends on the crystal structure. However, for cubic crystals as per gallium phosphide and zinc telluride, all elements of the nonlinear optical coefficient must vanish,

2.2. Beam Polarisation and Crystal Orientations

except for $d_{14} = d_{25} = d_{36} = d$, giving

$$\begin{pmatrix} P_x^{\omega_2} & P_y^{\omega_2} & P_z^{\omega_2} \end{pmatrix} = \begin{pmatrix} 0 & 0 & 0 & d & 0 & 0 \\ 0 & 0 & 0 & 0 & d & 0 \\ 0 & 0 & 0 & 0 & 0 & d \end{pmatrix} \begin{pmatrix} E_x^{\omega_1} E_x^{\omega_3} \\ E_y^{\omega_1} E_y^{\omega_3} \\ E_z^{\omega_1} E_z^{\omega_3} \\ E_y^{\omega_1} E_z^{\omega_3} + E_z^{\omega_3} E_y^{\omega_1} \\ E_x^{\omega_1} E_z^{\omega_3} + E_x^{\omega_3} E_z^{\omega_1} \\ E_x^{\omega_1} E_y^{\omega_3} + E_x^{\omega_3} E_y^{\omega_1} \end{pmatrix}, \quad (2.30)$$

For the case of optical rectification of a broadband optical pulse from a single laser source, the input fields \vec{E}^{ω_1} and \vec{E}^{ω_3} are clearly parallel, ie. $E_i^{\omega_1} = E_i^{\omega_3} = E_i$. The matrix expression above then simplifies to

$$\begin{pmatrix} P_x^{\omega_2} & P_y^{\omega_2} & P_z^{\omega_2} \end{pmatrix} = 2d \begin{pmatrix} E_y E_z \\ E_x E_z \\ E_x E_y \end{pmatrix}. \quad (2.31)$$

In order to determine the optimum beam polarisation for terahertz generation, we define the coordinate system of figure 2.5. The optical pulse is incident on a [110] gallium phosphide crystal [32] at an angle of incidence, ϕ , and with an azimuth angle α . The electric field is tangentially polarised, so as to minimise reflections from the crystal surface at Brewster's angle of incidence, calculated from Sellmeier data in [33] to be 73° . Transforming into the frame of the crystal, calculating the polarisation according to equation 2.31, and transforming back into the frame of the input field allows the resulting nonlinear polarisation to be expressed as sagittal and tangential components

$$P^{\omega_2} \propto \left(-\frac{1}{2} \sin \alpha ((3 \cos 2\alpha + 1) \cos^2 \phi + 2 \sin^2 \phi) \right. \\ \left. 3 \cos \alpha \cos \phi (\sin^2 \phi - \cos^2 \phi - \sin^2 \alpha) \right). \quad (2.32)$$

In figure 2.6 the relative magnitude of the nonlinear polarisation is plotted

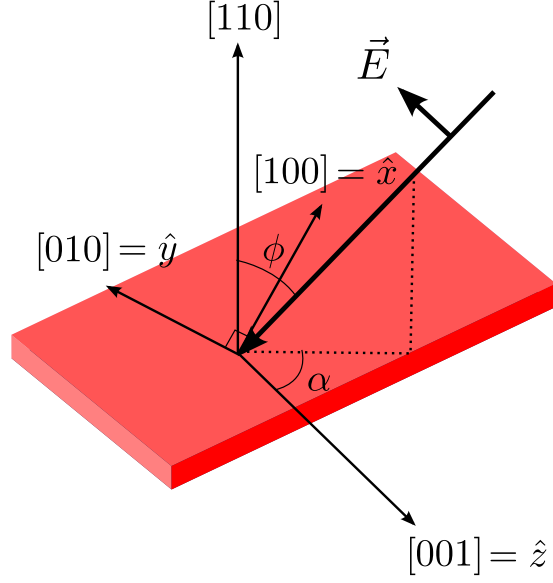


Figure 2.5: Coordinate system used for deriving the optimum optical beam orientation for terahertz generation.

for varying ϕ and α , along with the transects through this plot for normal incidence, ($\phi = 0$) and at Brewster incidence, where refraction leads to $\phi = 17.8^\circ$. It is seen that, at Brewster incidence, the amplitude of the nonlinear polarisation is $\simeq 25\%$ down on the maximum that can be obtained at normal incidence. Whilst further increases in efficiency could therefore be achieved by using a custom-grown crystal where the $[110]$ crystal axis is at Brewster's angle to the surface normal, we instead use here a more readily-available $[110]$ crystal for reasons of economics. Further, we note that, in order to maximise the terahertz generation efficiency, the optimal azimuthal angle α is 57° to the $[001]$ crystal axis. Mounting the crystal in a conventional rotation mount allows this to be tuned experimentally. For the cavity experiment, where we couple the generated terahertz radiation out of the polished end face, the edges are cut as in figure 2.7.

2.2. Beam Polarisation and Crystal Orientations

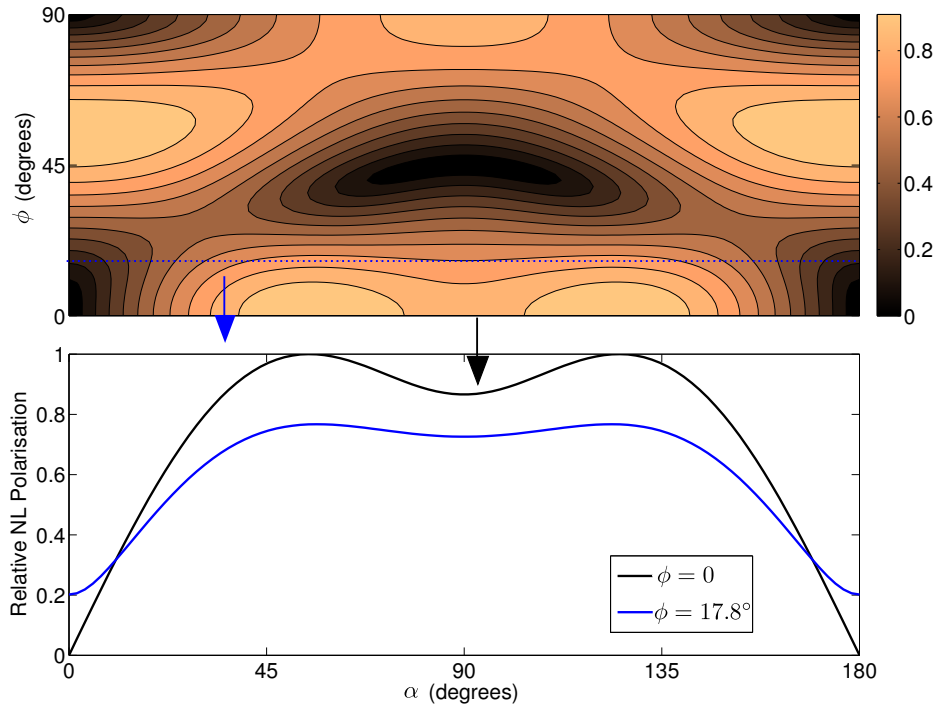


Figure 2.6: Relative nonlinear polarisation as a function of incidence angle, ϕ , and azimuthal angle, α , as defined in figure 2.5. Cuts are shown for normal incidence, $\phi = 0$, and for incidence at Brewster's angle, which leads to a propagation direction in the crystal such that $\phi = 17.8^\circ$.

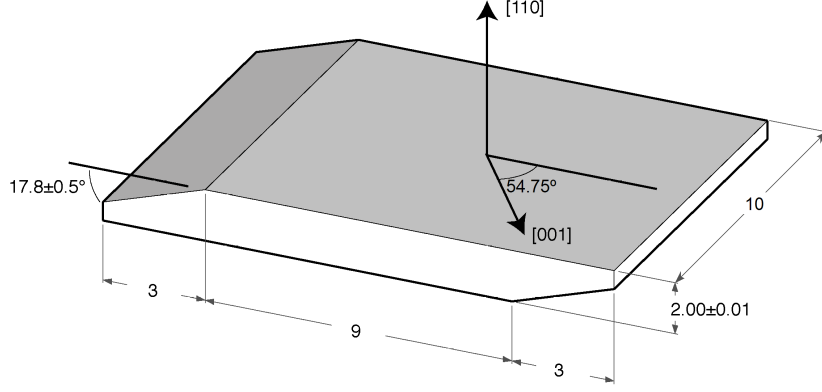


Figure 2.7: Dimensions, cuts, and orientation of gallium phosphide crystal for enhancement cavity work.

2.3 Phase-matching

The nonlinear polarisation produced by the driving optical field will propagate with the envelope of the driving optical pulse, that is, with the optical *group* velocity, v_{opt}^g . In order that this generated polarisation remain in phase with the radiated terahertz field, we seek to match this optical group velocity to the phase velocity of the terahertz field, v_{THz}^p . The distance over which the constructive interference between the radiated terahertz field and the nonlinear polarisation due to the driving optical field is maintained is the coherence length of the interaction. In contrast to other nonlinear optical processes, where one seeks to match the phase velocities of the driving and generated radiation, optical rectification requires the matching of the optical group velocity to the terahertz phase velocity. In order to determine the coherence length, we follow the method of [34] in defining an effective optical refractive index, or optical group index:

$$n_{opt}^{(group)} = n_{opt} - \lambda_{opt} \left. \frac{dn_{opt}}{d\lambda} \right|_{\lambda_{opt}} \quad (2.33)$$

2.3. Phase-matching

where n_{opt} is the conventional optical refractive index of the material in which the radiation propagates, and λ_{opt} is the wavelength of the optical radiation. The coherence length for the nonlinear optical process can then be written

$$L_c = \frac{\pi c}{\omega_{THz} |n_{opt}^{(group)} - n_{THz}|}. \quad (2.34)$$

Many nonlinear materials used for terahertz generation exhibit large dispersion at terahertz frequencies owing to a number of absorption features. For example, gallium phosphide exhibits a phonon resonance around 10 THz, and therefore n_{THz} is significantly greater than the optical refractive index. However, the absorption edge at 2.25 eV (540 THz, 550 nm) gives rise to substantial dispersion at optical wavelengths, such that $\frac{dn_{opt}}{d\lambda}$ is significantly less than zero. Careful tuning of the optical wavelength can then give rise to excellent phase-matching at around 1 μm , where the effective optical refractive index is equal to the terahertz refractive index, as shown in figure 2.8. To emphasise this point, the coherence length for a range of terahertz frequencies and optical wavelengths, as predicted by equation 2.34 in gallium phosphide at room temperature is plotted in figure 2.9. Further, cuts through this contour plot are given for the optical wavelength of 1030 nm produced by an ytterbium fibre laser system, and at a terahertz frequency of 1 THz. The former cut shows that, under such operating conditions, long coherence lengths of up to several millimetres can be generated. In addition, the coherence length as a function of driving optical wavelength is plotted for a terahertz frequency of 1 THz. It is seen that the optimal optical wavelength falls conveniently near that of an ytterbium fibre laser system. Driving a gallium phosphide nonlinear crystal with the 1030 nm output of a mode-locked ytterbium-doped glass fibre laser therefore represents a very attractive method for the generation of terahertz radiation via optical rectification.

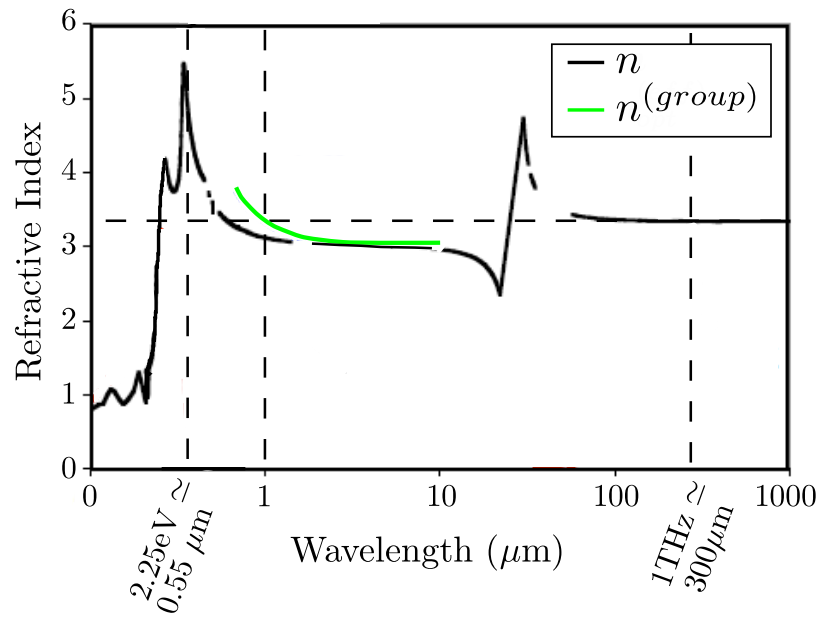


Figure 2.8: Variation of refractive index throughout the optical and terahertz spectral ranges from data in [33], along with an experimental fit of the effective refractive index for optical wavelengths, as per equation 2.33. Note that, due to the resonance at 2.25 eV, tuning of the optical wavelength allows the effective refractive index to be matched to the terahertz refractive index, therefore satisfying the phase-matching condition.

2.3. Phase-matching

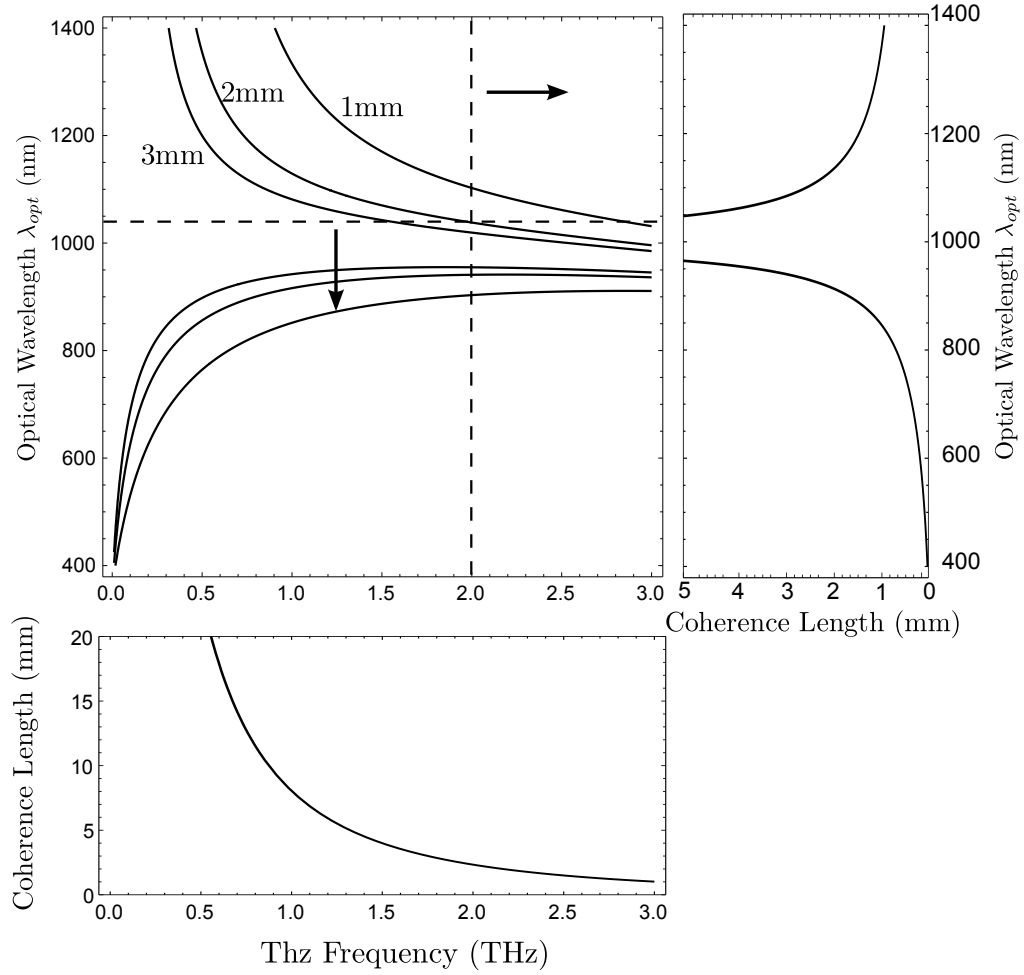


Figure 2.9: Coherence length for terahertz frequency generation via optical rectification in gallium phosphide, as predicted by equation 2.34. Cuts are shown for optical wavelengths of 1030 nm, and for terahertz frequencies of 1 THz.

2.4 Lasers

2.4.1 Oscillator Design

Due to the quadratic dependence of the generated nonlinear polarisation on the input electric field predicted by equation 2.3, it is desirable to use short pulses of intense optical radiation to drive the process, rather than a constant amplitude, continuous wave (CW) beam. Further, a broad optical spectrum is necessary to generate difference frequency components in the terahertz frequency range. By far the most common method of generating short, broadband optical pulses is to use mode-locked lasers.

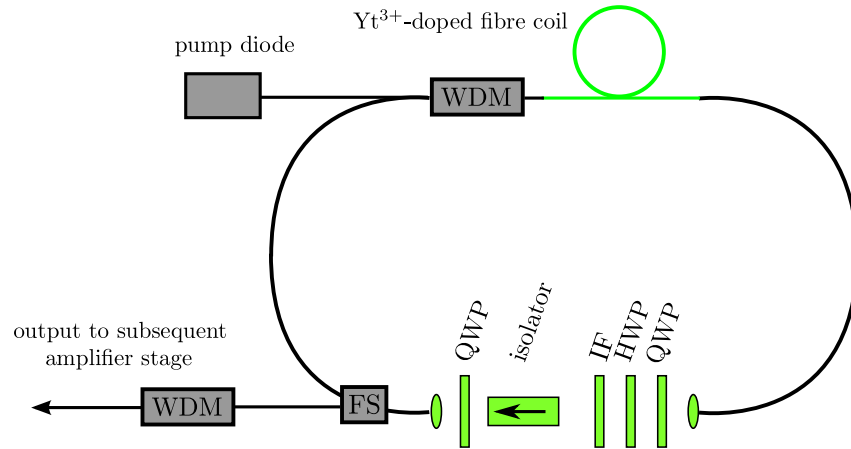
In order to generate the short pulses required for this experiment, mode-locked ytterbium fibre lasers of the type described in [35] are used. An overview of each laser is given in figure 2.10. The first, identical in design to that of [35], is mode-locked by virtue of the nonlinear polarisation in the optical fibre components. (SMF Corning Hi-1060). High peak intensity pulses generated in a length of ytterbium-doped gain fibre (Cor-Activ DC-170-40-YB-2) exhibit a stronger nonlinear polarisation rotation (NPR) than the low peak intensity CW case. This polarisation rotation is converted into an amplitude modulation at the repetition rate of the pulse in a section of bulk polarisation optics arranged as in figure 2.10a) [36]. The combined effect of the NPR and polarisation optics is therefore analogous to that of a saturable absorber, such that intense pulses experience reduced intracavity losses compared to those of the continuous wave (CW) case. In order to give stable mode-locked operation, the bandwidth, and therefore the minimum pulse duration, is limited by spectrally filtering the intracavity pulses using a 10 nm bandwidth birefringent filter centred at 1030 nm. Further, the constant normal dispersion of the laser, combined with gain saturation, means that the intracavity pulse undergoes strong spectral breathing in a single cavity roundtrip. Further details are given in reference [35]. The second laser was modified from a cavity configuration initially assembled by Simon Bret, and relies on the same physical principles as the laser discussed previously, but the components are arranged such that a bulk high reflectivity mirror can be incorporated into the cavity. This mirror can then be

mounted on a piezzo-electric actuator and used to make small scale, but high speed adjustments to the cavity length, and hence the pulse repetition rate. For both laser designs, a portion of the intracavity power is coupled out of the cavity using a 90/10% fibre coupler (FS). A fibre-coupled wavelength-division multiplexer (WDM) is used to further isolate the pump radiation of subsequent amplification stages from the laser cavity.

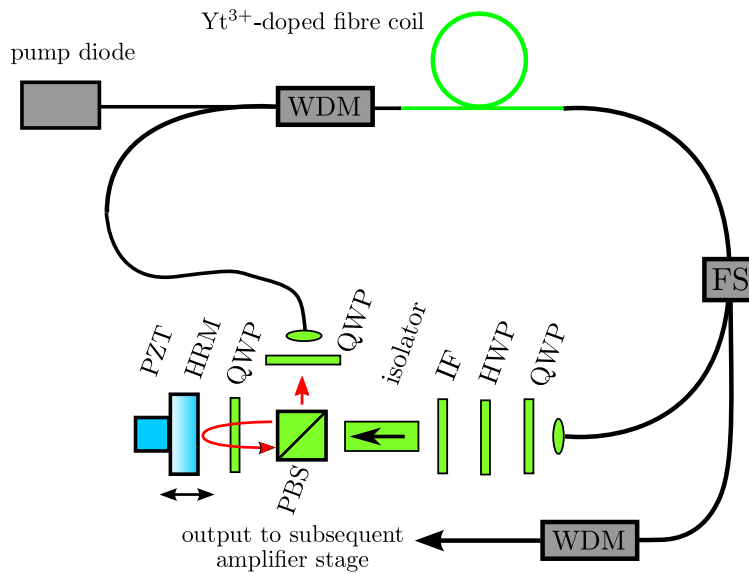
For each laser, 10% of the intracavity power is coupled out of the cavity to provide an output power of approximately 12 mW. A further 10% of this output power is picked off using fibre splitters for the purpose of triggering the rf electronics used in the dual-comb experiment. This fraction of the laser output serves only as a diagnostic port in the case of the cavity experiment. The outputs of each laser are amplified in fibre coupled, forwards-pumped ytterbium-doped fibre amplifiers, henceforth referred to as pre-amplifiers so as to distinguish this stage from the later power-amplification stage. Each preamplifier gives an average power output of about 180 mW. In the case of the first laser, the output of the pre-amplifier stage is passed through a large aperture optical isolator (IsoWave part no:I-106-T5-L), and coupled into a 1.5m length of ytterbium-doped photonic crystal fibre (PCF) for the final amplification stage, henceforth the power amplifier. The PCF is backwards pumped with a 40 W 976 nm pump diode (Apollo Instruments part no:F20-976-1) which has had the drive circuitry modified to reduce the amplitude of line harmonics on the high current supply (see section 2.4.3).

Due to the fact that none of the fibre components used in this apparatus are polarisation maintaining (PM) fibres, the output of any fibre stage is, in general, elliptically polarised. In order to obtain linear polarisation it is necessary to use a quarter wave plate-half wave plate pair to provide adjustment of an arbitrary elliptical polarisation to a given linear polarisation state, as required for use with optical isolators, diffraction gratings, efficient coupling into the enhancement cavity, and optimum terahertz generation in electro-optic crystals.

2.4. Lasers



(a) Laser oscillator design used to provide the high-power (following two subsequent amplification stages) pulses for both the cavity work and the single-comb, terahertz time-domain spectroscopy work described later.



(b) Laser oscillator design used to provide the local oscillator pulses for the work described in Chapter 6.

Figure 2.10: Design of the two mode-locked ytterbium fibre lasers. The operation of each laser is described in the text. Parts labelled are: quarter wave plate (QWP), half wave plate (HWP), interference filter (IF), piezo-electric actuator (PZT), polarisation beam splitter (PBS), 90/10% fibre coupler (FS), and fibre-coupled wavelength-division multiplexer (WDM).

2.4.2 Compensation of Pulse Chirp due to Dispersion of Fibre Components

Due to dispersive effects in the fibre components used in the oscillator and amplifier stages, the output pulses are highly chirped. The dependence of the material refractive index on radiation wavelength means that, within the broad spectral amplitude of the pulse, each spectral component will propagate with a slightly different phase velocity. This is the effect of material dispersion. In addition, the confinement of the electric field within the dielectric medium of the fibre, and the resulting dependence of the degree of field confinement on the wavelength of the radiation leads to waveguide dispersion. We neglect the effect of dispersion between transverse modes here as the fibre components used only allow propagation of a single transverse mode at our wavelengths. The combined effects of waveguide and material dispersion are encompassed in the mode propagation constant $\beta(\omega)$ and produce a frequency-dependent phase delay on the optical pulse. Writing the pulse as the product of a carrier wave at the central optical frequency ω_c , and an envelope function describing the pulse propagation, a pulse having a continuous spectral amplitude is described as

$$E(z = 0, t) = e^{i\omega_c t} \int \tilde{E}(\Omega) e^{i\Omega t} d\Omega, \quad (2.35)$$

where ω_c represents the optical carrier frequency, and $\tilde{E}(\Omega)$ is the Fourier transform of the pulse envelope. Propagation of this pulse over a length z of a dispersive medium writes a frequency-dependent phase onto the field, such that

$$E(z, t) = e^{i\omega_c t} \int \tilde{E}(\Omega) e^{i(\Omega t - \beta(\omega_c + \Omega)z)} d\Omega \quad (2.36)$$

where $\beta(\omega_c + \Omega)$ is the mode propagation constant at frequency $\omega = \omega_c + \Omega$. It is common to expand β near the optical carrier frequency in a Taylor series thus:

$$\beta(\omega_c + \Omega) = \beta(\omega_c) + \left. \frac{d\beta}{d\omega} \right|_{\omega_c} \Omega + \frac{1}{2} \left. \frac{d^2\beta}{d\omega^2} \right|_{\omega_c} \Omega^2 + \frac{1}{6} \left. \frac{d^3\beta}{d\omega^3} \right|_{\omega_c} \Omega^3 + \dots \quad (2.37)$$

It can be shown that $\frac{d\beta}{d\omega} = \frac{1}{v_g}$ where v_g is the group velocity, and that therefore the group velocity dispersion is given by

$$\frac{d}{d\omega} \left(\frac{1}{v_g} \right) = \frac{d^2\beta}{d\omega^2}. \quad (2.38)$$

It is common to define the group velocity dispersion parameter, D , to characterise the optical fibre in which the pulse propagates by

$$D = \frac{2\pi c}{v_g^2 \lambda^2} \frac{dv_g}{d\omega} = -\frac{2\pi c}{\lambda^2} \left(\frac{d^2\beta}{d\omega^2} \right), \quad (2.39)$$

The frequency dependent phase-shift in equation 2.36 gives rise to a temporal broadening of the pulse and therefore a lowering of the peak electric field intensity. As optical rectification is a nonlinear effect whose efficiency will increase with the amplitude of the driving electric field, it is highly desirable to use the shortest pulses possible. To second order, this is the case when the quantity

$$\frac{d^2\phi(\omega)}{d\omega^2} = -\frac{2\pi c}{\lambda^2} \left(\frac{d^2\beta}{d\omega^2} \right) z = zD \quad (2.40)$$

is minimised. $\frac{d^2\phi(\omega)}{d\omega^2}$ is termed the group delay dispersion (GDD). $\frac{d^3\phi(\omega)}{d\omega^3}$, as given by the fourth term in equation 2.37, is the third order dispersion (TOD) delay.

In order to correct for the dispersive effect of the fibre components and re-compress the optical pulses, an optical pulse compressor employing a diffraction grating pair is used for each laser. The principal of operation of such a device was first outlined by Treacy [37]. Fork et al. [38] showed that the amount of GDD induced by propagating an optical pulse through a system of diffraction gratings, configured as in figure 2.11, is given by

$$\frac{d^2\phi_g}{d\omega^2} = \frac{\lambda^3 l_g}{\pi c^2 d^2} \left[1 - \left(\frac{\lambda}{d} - \sin \gamma \right)^2 \right]^{-\frac{3}{2}} \quad (2.41)$$

where l_g is the separation of the gratings, γ is the angle of incidence and d is the groove spacing for the gratings. In order to estimate the required separation of the grating compressor, we start from manufacturers data for the single mode fibre used in the laser system. In the case of the lasers used here, the total length of fibre is 15 m, and the GVD is given as 27 ps²/km. The gratings used are transmission diffraction gratings with a ruling of 1200 lines/mm, or $d \simeq 830$ nm, and an optimum angle of incidence of 41.7°. From equation 2.41 the approximate required separation is therefore 4 cm. Note that this estimate neglects third order dispersion (TOD) of both the grating compressor and fibre components. Treacy et al. showed that, for a typical grating compressor, the sign of the TOD term is positive, as opposed to the negative GVD term. In contrast, in typical single mode fibres, both the TOD and GVD terms are positive. The use of a grating compressor to compensate for the GVD of the fibre components therefore increases the amount of TOD in the total optical system, which leads to the temporal duration of the resulting pulse being greater than the predicted transform limit [39]. In practice l_g was set to the predicted value of 4 cm, and then adjusted experimentally to give optimum pulse compression. The optimum grating separation was found to be 37 mm, and the resulting pulse compression is shown in figure 2.12, together with fits to Gaussian and sech² pulse shapes of 240 fs full width at half maximum durations. Note that, for the observed 7 nm spectral bandwidth, one expects a temporal duration of 160 fs at the Fourier transform limit. The fact that the minimum pulse width attainable is 240 fs is attributed to TOD, arising both in the fibre components and in the grating compressor. Whilst methods have been demonstrated that produce an output pulse closer to the transform limit by minimising the effects of both GVD and TOD, [40], the additional components required significantly reduce the final pulse energy. For this work, therefore, we choose not to employ such techniques.

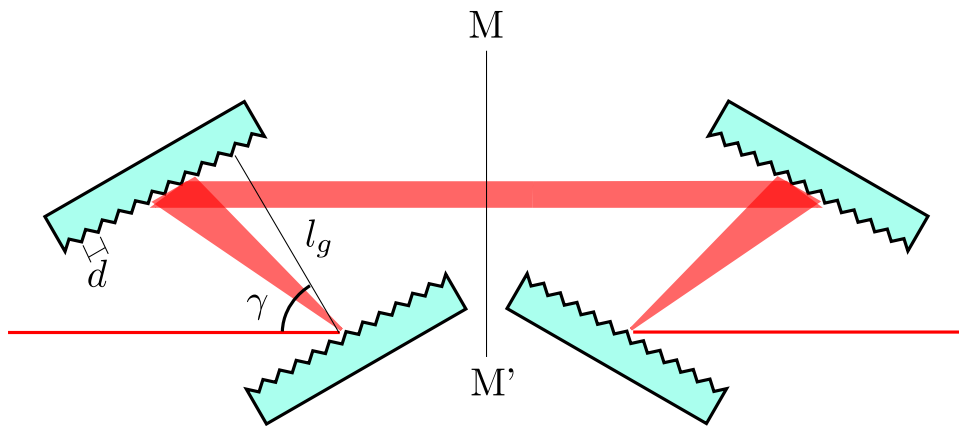


Figure 2.11: Configuration of the diffraction grating pulse compressor used for dispersion compensation. l_g is the separation of the two component gratings along the grating normal, γ is the angle of incidence, and is determined by the blaze angle of the grating. The transect MM' shows the line of symmetry of the system. In practice, the beam is reflected back through the same pair of diffraction gratings using a metal mirror, thereby compensating for the spatial chirp across the beam profile arising from a single pass.

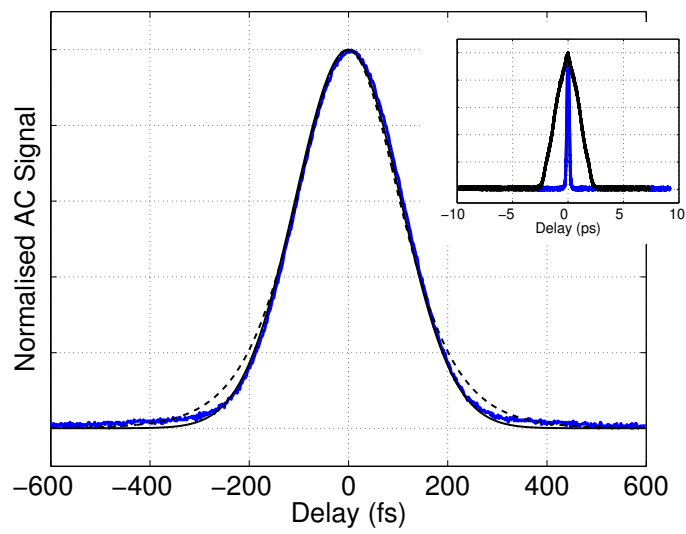


Figure 2.12: Typical autocorrelation trace of the laser output pulse (blue line) of the pump laser following compression, together with fits to Gaussian (solid black line) and sech^2 (dashed line) pulse shapes, both of 240 fs full width at half maximum. Inset: Comparison of compressed and uncompressed pulse widths.

2.4.3 Pump Diode Line Noise

During the experimental work, it was noticed that the optical output of the pump diode used for the power amplifier stage displayed modulations at harmonics of the 60 Hz line frequency, and that these modulations were written onto the pulse train of the mode-locked oscillator at the output of the high-power amplification stage, as indicated in figure 2.13. This was measured using a fast photodiode and rf amplifier circuit positioned behind the dichroic mirror used to couple the seed pulse into the input collimator of the PCF at the power amplifier stage. The origins of these modulations were eventually traced to the linear voltage supply used to provide a control signal to a power transistor, internal to the diode controller provided by Apollo instruments, a schematic of which is shown in figure 2.15 with the linear voltage supply in question indicated by $V_{control}$. Whilst exact specifications of the controller were not made available, it was found that deriving this control voltage from a known clean linear dc supply lessened the amplitude of the line harmonics on the controller output current (figure 2.14) with a corresponding reduction in noise on the optical output. The ultimate benefit of driving the laser in this way can be seen from figure 2.13 to be a reduction in the amplitude of the line harmonics out to 360 Hz of approximately 5-10 dB.

In addition to replacing the control voltage with that from a clean, linear supply, the effect of replacing the fixed 12V, 60A supply (labelled V_{drive} in figure 2.15) was examined, but it was found that this gave no further benefit over the data shown in figure 2.13.

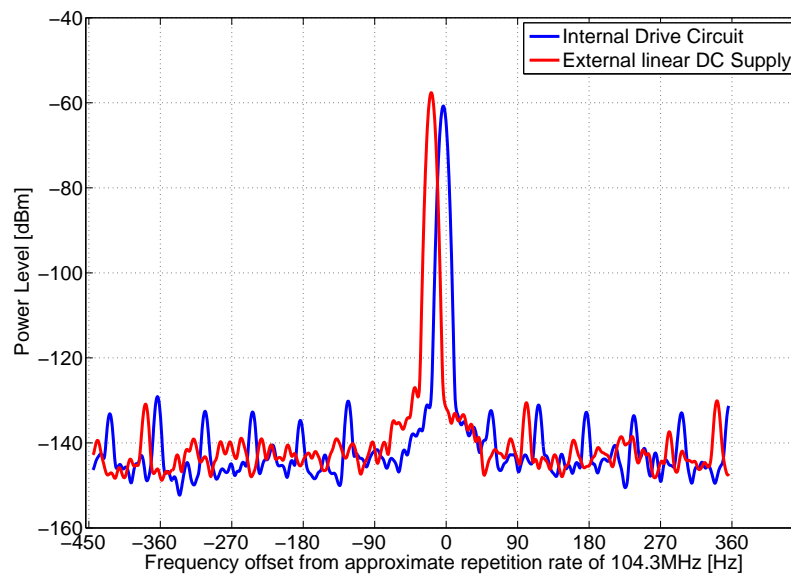


Figure 2.13: Comparison of modulation sidebands on the optical pulse train repetition rate of 104.3 MHz following the high-power amplifier stage with the controller in its original configuration, and following modifications to allow the regulation of the transistor control voltage with an external linear dc supply.

2.4. Lasers

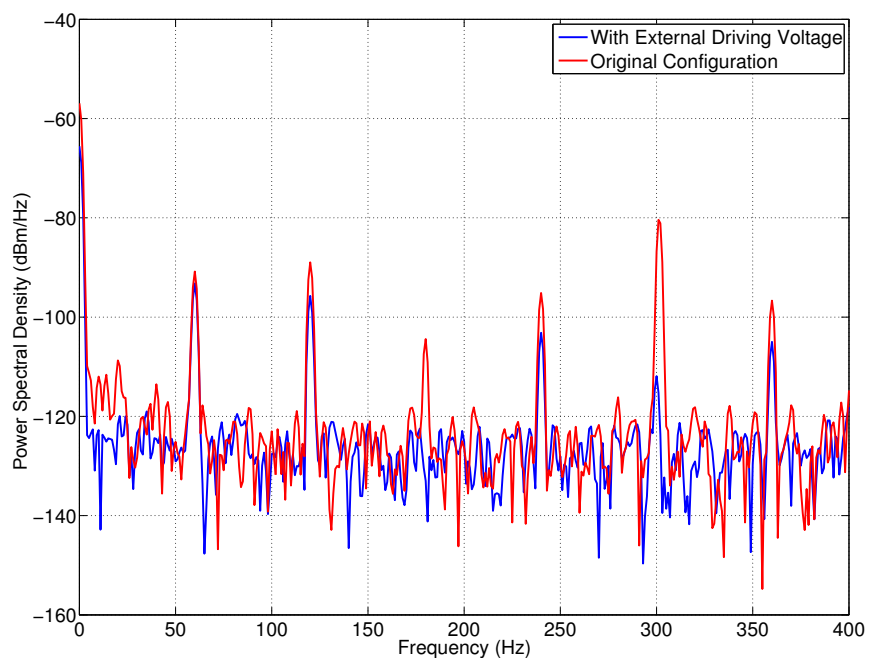


Figure 2.14: Comparison of noise on the electrical current used to drive the Apollo Instruments pump diode, as measured across the shunt resistor, R shown in figure 2.15. Of particular note are the complete elimination of modulations at 180 Hz, and the substantial reduction of harmonics at 300 Hz.

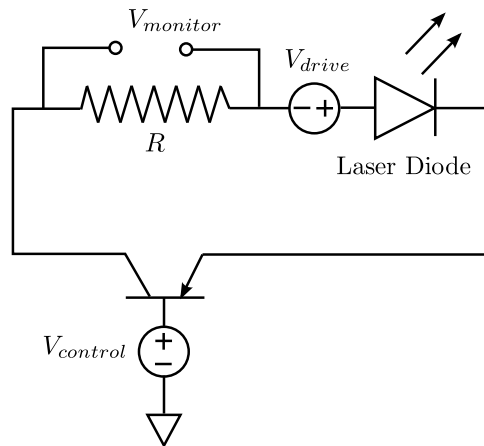


Figure 2.15: Schematic of the Apollo Instruments laser diode driver, model no. D-560. The basic principal of operation is the use of a variable dc voltage, $V_{control}$ to regulate the current flowing through a power transistor. The laser diode itself is connected in series with a fixed 12V, 60A supply, V_{drive} , and with the collector emitter terminals of the control transistor. It should be noted that actual schematics were not made available, and that this figure serves only to document the process involved in reducing the line harmonics on the optical output of the diode. It was found that replacing the internal supply used to provide $V_{control}$ reduced the appearance of line harmonics on the laser output, and that no further improvement was gained by replacing the fixed 60A supply.

Chapter 3

Use of a Passive Enhancement Cavity for High Efficiency Terahertz Generation

3.1 Cavity Basics

Equation 2.3 predicts that the second order nonlinear polarisation increases quadratically with the intensity of the driving electric field, as is the case for all second order nonlinear optical processes. It is therefore desirable to increase the pump intensity as much as possible so as to increase the polarisation intensity, and therefore the intensity of the radiated difference frequency field. A number of options exist for doing this. For an input field provided by a fibre laser, it is possible to increase the laser pulse energy using single pass fibre amplifier stages, but at higher pulse energies the variation of the fibre refractive index with optical intensity will lead to self phase modulation. The resulting new spectral components generated in this process lead to frequency chirping of the optical pulse, which cannot be simply compensated for at the laser output as was shown in section 2.4.2 for the case of GVD. This therefore increases the minimum pulse duration, and hence reduces the peak intensity, with which it is possible to drive the nonlinear crystal, reducing the potential gain in nonlinear conversion efficiency. Alternatively, regenerative amplifiers can be used. These however typically operate on a ‘pulse-picking’ scheme, whereby one in $\simeq 10^5$ seed

3.1. Cavity Basics

pulses are amplified, thereby sacrificing repetition rate for peak power. Further, by reducing the pulse repetition rate in such a manner, the spacing of the frequency comb elements is reduced, resulting in difficulties resolving individual frequency elements.

A third option to increase the amplitude of the driving laser field is to use a passive enhancement cavity in which the laser pulse is resonantly enhanced. This is particularly appealing for enhancement of nonlinear optical processes due to the relatively low single-pass conversion efficiency implied by the low values of d_{eff} . Essentially, in the enhancement cavity, the pump radiation not converted in the first pass of the optical field through the nonlinear crystal is “recycled”, increasing the efficiency of conversion.

In order to understand the enhancement process in more detail, consider a monochromatic plane wave incident on an optical resonator consisting of a pair of highly reflecting mirrors, as shown in figure 3.1. The incident field is written E_{inc} and that portion coupled into the resonator is denoted E_{in} . After one roundtrip, the field is E_1 , after two roundtrips, E_2 , and so on. The total field at the input mirror is then the sum of these fields:

$$E_T = E_{in} + E_1 + E_2 + E_3\dots \quad (3.1)$$

Upon travelling one roundtrip of the cavity, the wave undergoes a phase change $\phi = kd + \Phi_M$ where d is the optical path length of the cavity, and Φ_M is the total roundtrip phase-shift due to reflection at the cavity mirrors. We can therefore define a complex roundtrip attenuation factor

$$h = |\mathbf{r}|e^{-i\phi}, \quad (3.2)$$

where \mathbf{r} is the roundtrip reflectivity factor for the **field** that accounts for reflectivity losses at the mirrors, as well as any losses due to propagation through the cavity itself. This complex roundtrip attenuation factor then

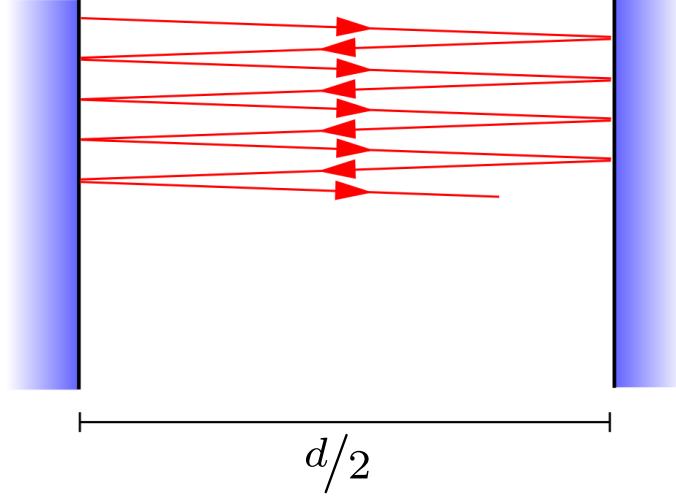


Figure 3.1: A simple two-mirror optical resonator.

relates each successive term in equation 3.1. Ie:

$$\begin{aligned}
 E_T &= E_{in} + hE_0 + h^2E_{in} + h^3E_{in} + \dots \\
 &= E_{in}(1 + h + h^2 + h^3 + \dots) \\
 &= \frac{E_{in}}{1 - h}
 \end{aligned} \tag{3.3}$$

The intensity then varies as the square of this electric field:

$$I \propto |E|^2 = \frac{|E_{in}|^2}{|1 - h|^2} = \frac{|E_{in}|^2}{|1 - |\mathbf{r}|e^{-i\phi}|^2}. \tag{3.4}$$

Using trigonometric identities, we rewrite this as

$$I = \frac{I_{in}}{1 + |\mathbf{r}|^2 - 2|\mathbf{r}| \cos \phi}, \tag{3.5}$$

where $I_{in} = \frac{c\mathcal{E}}{2}|E_{in}|^2$ is the intensity transmitted by the input mirror. It is

3.1. Cavity Basics

common to characterise the resonator in terms of its finesse,

$$\mathcal{F} = \frac{\pi\sqrt{|\mathbf{r}|}}{1 - |\mathbf{r}|}, \quad (3.6)$$

to give

$$I = \frac{I_{max}}{1 + \left(\frac{2\mathcal{F}}{\pi}\right)^2 \sin^2\left(\frac{\phi}{2}\right)}. \quad (3.7)$$

Here, I_{max} is the maximum intracavity intensity one can hope to maintain given the cavity is tuned to perfect resonance, where

$$\sin\left(\frac{\phi}{2}\right) = 0. \quad (3.8)$$

I_{max} is therefore given by

$$I_{max} = \frac{I_{in}}{(1 - |\mathbf{r}|)^2} = I_{inc} \frac{1 - R_{ic}}{(1 - \sqrt{R_{ic}R})^2}, \quad (3.9)$$

where I_{inc} is the input intensity and R is the cumulative product of the more commonly known power reflectivity magnitude of all the mirrors except the mirror upon which the input beam is incident, known as the input coupler, with power reflectivity R_{ic} . Ie. $R = \prod_i R_i$ where R_i is the power reflectivity of the i th mirror, and the product runs over the i mirrors in the cavity. We note that it is straightforward to include cavity parasitic losses due to scattering etc in the factor R thus:

$$R = (1 - L_{cav}) \times \prod_i R_i \quad (3.10)$$

where L_{cav} is the roundtrip loss factor. The finesse of the cavity can be rewritten in terms of the power reflectivities as

$$\mathcal{F} = \frac{\pi\sqrt[4]{RR_{ic}}}{1 - \sqrt{RR_{ic}}} \quad (3.11)$$

A high finesse cavity is therefore produced when the roundtrip optical loss is low. Furthermore, the peak intensity, I_{max} is produced when on res-

3.1. Cavity Basics

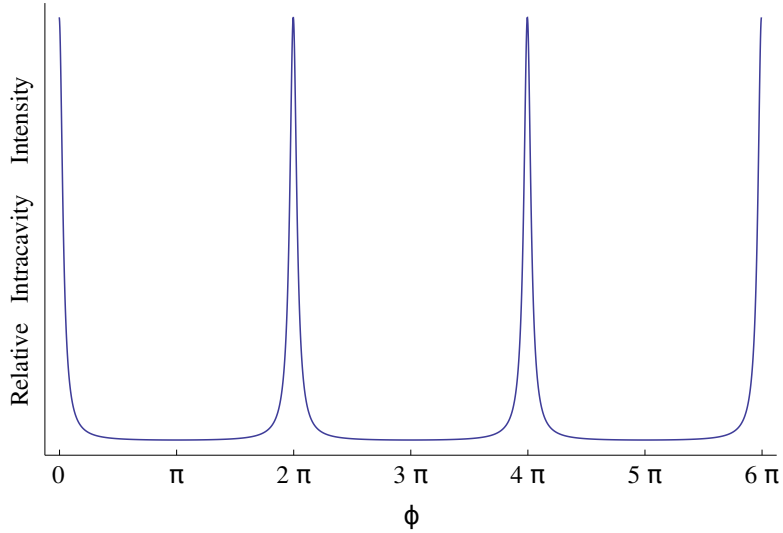


Figure 3.2: Resonant modes of an optical resonator. The cavity shows maxima for roundtrip phases of $\phi = 0, 2\pi, 4\pi, \dots$

onance, that is to say that the roundtrip phase, $\phi = 0, 2\pi, 4\pi, \dots$. The cavity therefore shows maxima in intracavity intensity (and therefore transmission via the non-unity reflectivity of any of the resonator mirrors) for roundtrip phase changes of integer multiples of 2π . When tuned to resonance, the cavity therefore gives an ideal amplification factor of

$$\frac{I_{max}}{I_{in}} = \frac{1 - R_{ic}}{(1 - \sqrt{RR_{ic}})^2} \quad (3.12)$$

which, for given $R \sim 1$, has a maximum

$$\frac{I_{max}}{I_{inc}} = \frac{1}{1 - R} \simeq \frac{\mathcal{F}}{\pi} \text{ at } R_{ic} = R. \quad (3.13)$$

Therefore, in order to obtain the maximum intracavity intensity, the losses at the input coupler should be equal to the roundtrip losses due to all other components in the cavity. Under these conditions, the cavity is said to be impedance-matched.

3.2 Amplification of a Femtosecond Optical Comb Using a Passive Enhancement Cavity

Section 3.1 focussed on how a passive enhancement cavity can be used to increase the amplitude of an electromagnetic field at a single laser frequency. For the purposes of this work, we wish to optimise the efficiency of the optical rectification process described by equation 2.3, where the amplitude of the nonlinear polarisation scales with the square of the driving optical field. It is therefore desirable to use short pulses to increase the efficiency of the optical rectification process. We therefore seek to use a passive optical resonator to simultaneously enhance the frequency content of the broad optical bandwidth produced by the mode-locked laser described in section 2.4.

In section 2.4, a mode-locked oscillator was shown to have an output that can be described in the frequency domain as a broad spectrum of evenly spaced laser comb lines. In order to calculate the amplification of such a broadband output, we consider the amplification of each of the $\simeq 10^5$ laser modes within the cavity. Recall equation 3.7 describing the enhancement of a monochromatic field inside a passive enhancement cavity.

$$I = \frac{I_{max}}{1 + \left(\frac{2\mathcal{F}}{\pi}\right)^2 \sin^2\left(\frac{\phi}{2}\right)}. \quad (3.14)$$

Further, recall that the roundtrip phase of the enhancement cavity was written as $\phi = 2kd + \Phi_M$, where where d is the optical path length of the cavity, and Φ_M is the sum of the phase-shifts occurring due to reflection at each of the cavity mirrors over a single roundtrip. For the following discussion, we generalise this by including the frequency dependence of ϕ explicitly, such that $\phi \rightarrow \phi(\omega)$ thereby allowing for the effects of dispersion as the pulse propagates within the cavity. Further, we include in ϕ an additional term $\Phi_X(\omega)$ corresponding to the frequency dependent phase delay due to transmission through a dispersive optic (in our case, this will be the non-linear crystal) placed within the cavity. The resonance condition therefore

3.2. Amplification of a Femtosecond Optical Comb Using a Passive Enhancement Cavity

becomes

$$\phi(\omega) = k(\omega)d + \Phi_M(\omega) + \Phi_X(\omega) = 2m\pi, \quad (3.15)$$

where $\Phi_M(\omega)$ accounts for the frequency dependence of the phase delay due to reflection of the field at the cavity mirrors. The dispersion due to the air within the cavity is included in the dependence of the wavevector, $k(\omega)$ on frequency. For the case of zero group velocity dispersion, where Φ_M and Φ_X do not depend on frequency, and the wavevector $k(\omega)$ varies linearly with frequency such that $k(\omega) = k(\omega_c) + (\omega - \omega_c)\frac{1}{v_g}$, we can apply the methods of section 2.4.2 to obtain ¹

$$\begin{aligned} \phi(\omega) &= k(\omega)d + \Phi_M + \Phi_X \\ &= d \left(k(\omega_c) + (\omega - \omega_c)\frac{1}{v_g} \right) + \Phi_M + \Phi_X. \end{aligned} \quad (3.16)$$

The resonant modes of the enhancement cavity therefore satisfy

$$\omega_m = \frac{2v_g m \pi}{d} + \frac{v_g}{d} \left(dk(\omega_c) + \frac{d\omega_c}{v_g} - \Phi_M - \Phi_X \right). \quad (3.17)$$

In this dispersion-free case, the resonant spectrum of the cavity therefore has the form of an evenly spaced comb of frequencies, spaced from zero frequency by an amount given by the second term of equation 3.17. We note that, in the absence of dispersion, the phase and group velocities are equal such that $v_g = c$, and equation 3.17 predicts a spacing of the cavity modes in frequency of

$$\Omega_{FSR} = 2\pi \frac{c}{d}, \quad (3.18)$$

which is the familiar cavity free spectral range.

Recall now the frequencies of a mode-locked oscillator, as described by

¹In section 2.4.2 we use the mode propagation constant, $\beta(\omega)$ to describe the evolution of the phase with propagation distance in the fibre components of the laser system. In freespace, where it is not necessary to include the added effect of waveguide dispersion, we use the wavevector, $k(\omega)$.

3.2. Amplification of a Femtosecond Optical Comb Using a Passive Enhancement Cavity

equation 2.6,

$$\begin{aligned}\omega_M &= \frac{2M\pi}{\tau_{rep}} - \frac{\Delta\phi_{ce}}{\tau_{rep}} \\ &= M\omega_{rep} + \omega_0.\end{aligned}\tag{3.19}$$

which shows that the output of a mode-locked laser has a similar form of a comb of evenly spaced frequencies, spaced from zero frequency by the laser carrier-envelope offset frequency $\omega_0 = \Delta\phi_{ce}f_{rep}$. The angular pulse repetition frequency is simply $\omega_{rep} = 2\pi f_{rep}$.

In the dispersion-free case of equation 3.17, it is therefore possible to obtain complete overlap of the resonant modes of the enhancement cavity with the frequency comb elements of the laser, as in figure 3.2a), such that each and every laser mode is enhanced within the cavity by an amount determined by equation 3.9. Doing so requires control of both the mode spacing and mode offset of the frequencies being amplified [28].

In order to study the behaviour of the cavity for the case where the modes do not overlap with those of the seed laser completely, we define the offset, p , of the cavity modes with respect to the laser modes thus:

$$\begin{aligned}m &= M + p \\ &= \frac{\omega_M - \omega_0}{\omega_{rep}} + p\end{aligned}\tag{3.20}$$

Substituting this expression into equation 3.15 yields the cavity length for which each M th laser mode is resonant

$$\begin{aligned}d(\omega_M) &= \left[2\pi \left(\frac{\omega_M - \omega_0}{\omega_{rep}} + p \right) - \Phi_M(\omega_M) - \Phi_X(\omega_M) \right] \frac{1}{k(\omega_M)} \\ &= \frac{2\pi c}{n(\omega_M)} \left[\frac{1}{\omega_{rep}} - \frac{1}{\omega_M} \left(\frac{\omega_0}{\omega_{rep}} - p \right) \right] - \frac{(\Phi_M(\omega_M) + \Phi_X(\omega_M))c}{\omega_M n(\omega_M)}\end{aligned}\tag{3.21}$$

Again, consider a simple case where the laser carrier-envelope offset frequency, $\omega_0 = 0$, and the phase contributions of Φ_M and Φ_X are zero. Fur-

3.2. Amplification of a Femtosecond Optical Comb Using a Passive Enhancement Cavity

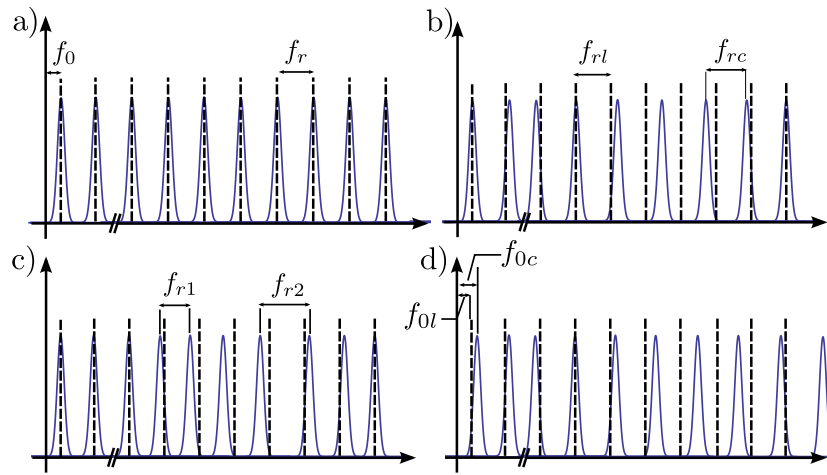


Figure 3.3: Varying overlap of the resonant modes of the passive enhancement cavity (in blue) with the longitudinal modes of the mode-locked laser used as the seed (dashed lines). a) Both the mode spacing and offset from zero frequency are matched, giving complete overlap, and therefore optimal enhancement of every frequency emitted by the laser. In this case, every mode of the laser is enhanced by a factor determined by equation 3.9. b) The repetition rate of the cavity, f_{rc} is greater than that of the laser, f_{rl} giving only complete overlap for certain modes. Only these modes circulate within the cavity, with the remainder being reflected at the input coupler. The power circulating within the cavity is therefore reduced with respect to that of a). c) The cavity shows dispersion, as indicated by the frequency-dependent spacing of the cavity modes. Whilst it is possible to vary the degree of overlap by varying the mode spacing and offset, the even spacing of the laser modes is such that complete overlap is not possible for this case. d) The offset frequency of the cavity f_{0c} is greater than that of the laser, f_{0l} . Again, mode overlap, and hence enhancement is reduced.

3.2. Amplification of a Femtosecond Optical Comb Using a Passive Enhancement Cavity

ther, assume the M th mode of the laser is resonant with the m th mode of the cavity, such that $p = 0$. In this case, we obtain,

$$d(\omega_M) = \frac{2\pi c}{\omega_{rep}}. \quad (3.22)$$

We can therefore satisfy the resonance condition for every single laser mode simultaneously, providing

$$\Omega_{FSR} = \omega_{rep}. \quad (3.23)$$

In the more general case where the cavity displays dispersion, the cavity mode spacing varies with frequency, as shown in figure 3.3c). In this case, it is not possible to obtain complete overlap of the laser and cavity modes, even with independent control of the mode spacing and offset frequencies. In this case, only those modes of the cavity corresponding to output modes of the laser will be amplified (the remaining modes of the cavity are not excited), reducing the power circulating within the cavity.

In order to better understand the effect of dispersion on the enhancement of the broadband optical field, we use the method developed in [41], and consider the power circulating within the enhancement cavity when seeded with the field of a mode-locked oscillator having the form of equation 2.5. Figure 3.4 shows the resonance map as a function of cavity length and optical wavelength. It is seen that, for $p \neq 0$, when the cavity length is varied away from that satisfying equation 3.23, the enhancement is reduced by virtue of laser modes at the edges of the pulse bandwidth not satisfying equation 3.15. In contrast, when the cavity is on resonance such that $p = 0$, the entire bandwidth of the seed laser resonates within the cavity. In this case, every single laser mode (and therefore the total optical power) is amplified according to equation 3.9.

In the presence of cavity dispersion, the length at which each laser mode exhibits maximum enhancement varies with frequency, as predicted by equation 3.21. For example, if the cavity exhibits a net roundtrip phase delay that is quadratic in frequency, as for the case of group velocity dispersion, one observes a ‘bending’ of the resonance map as shown in figure 3.5. As a

3.2. Amplification of a Femtosecond Optical Comb Using a Passive Enhancement Cavity

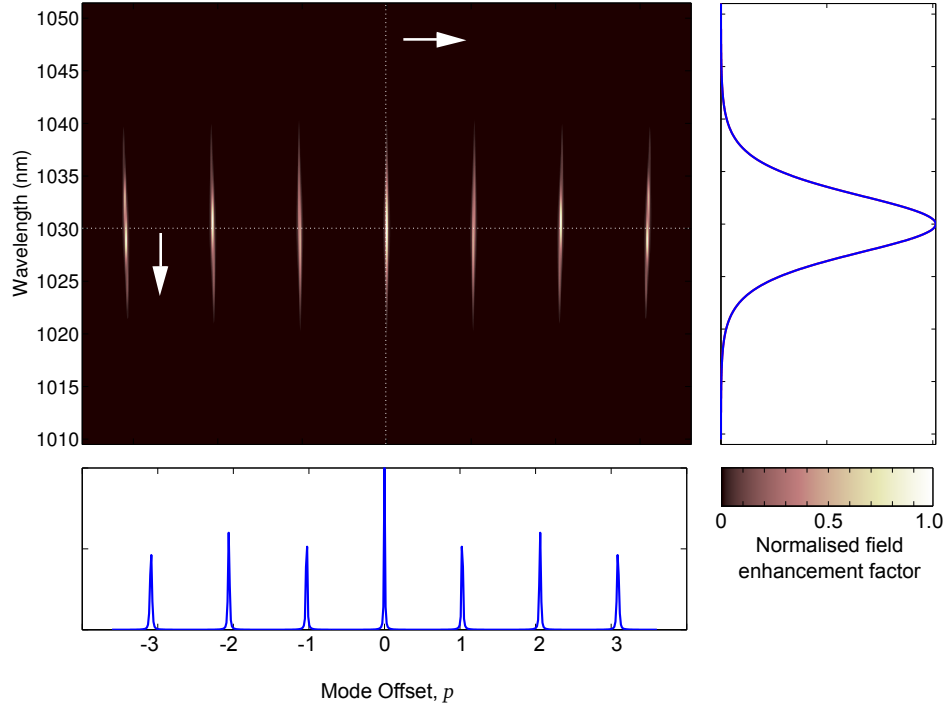


Figure 3.4: Main: Resonance map of a dispersion-free enhancement cavity seeded with a mode-locked laser with central wavelength $\lambda_0 = 1030$ nm, optical bandwidth $\Delta\lambda = 7$ nm, and repetition rate $f_{rep} = 100$ MHz. The finesse of the cavity is $\simeq 100$ to better show the resonance features. Bottom: Intensity enhancement as a function of cavity length, showing the decreased performance of the cavity for $p \neq 0$. Right: Intensity spectrum circulating within the cavity for $p = 0$, where the cavity length = $\frac{c}{f_{rep}}$.

result of this spectral phase-shift, the number of laser modes that are resonant within the cavity at any given length is reduced, leading to a reduction in the power circulating within the cavity. Further, the spectral narrowing that occurs leads to a temporal broadening of the pulse, further reducing the peak power. This is undesirable in our case due to the quadratic dependence of the expected amplitude of the terahertz field on the electric field amplitude. We will see later that the nonlinear crystals typically used for generation of terahertz radiation via optical rectification typically have large dispersion. For example, the group velocity dispersion of gallium phosphide is $\simeq 1250 \frac{\text{fs}^2}{\text{mm}}$. In order to compensate for this large dispersion, we use Gires-Tournois interferometric mirrors with a specified group delay, such that the roundtrip group delay of the cavity is minimised. We model the expected performance of this cavity in the following section.

3.3 Cavity Design

3.3.1 Mirror Choice and Dispersion Compensation

The passive enhancement cavity design studied here is portrayed in figure 3.6. We use a ring cavity design consisting of six mirrors in total.

Section 3.2 showed that, in order that the maximum possible optical bandwidth resonates in the enhancement cavity it is necessary that the resonance condition, equation 3.9, is satisfied for each spectral component of the laser output with which the cavity is seeded. Further, in the frequency domain this can be pictured as ensuring that the longitudinal modes of the enhancement cavity overlap with those of the seed laser. Equation 3.23 predicts that this requires that the free spectral range of the enhancement cavity, Ω_{FSR} is equal to the pulse repetition rate of the laser, ω_{rep} . For this work, a pump laser with a pulse repetition rate of nominally 104 MHz was used, such that the required optical path length in air of the enhancement cavity is 2.88 metres.

The optical cavity consists of a pair of curved mirrors, an input coupler, and several flat ‘fold’ mirrors. The curved mirrors serve two purposes.

3.3. Cavity Design

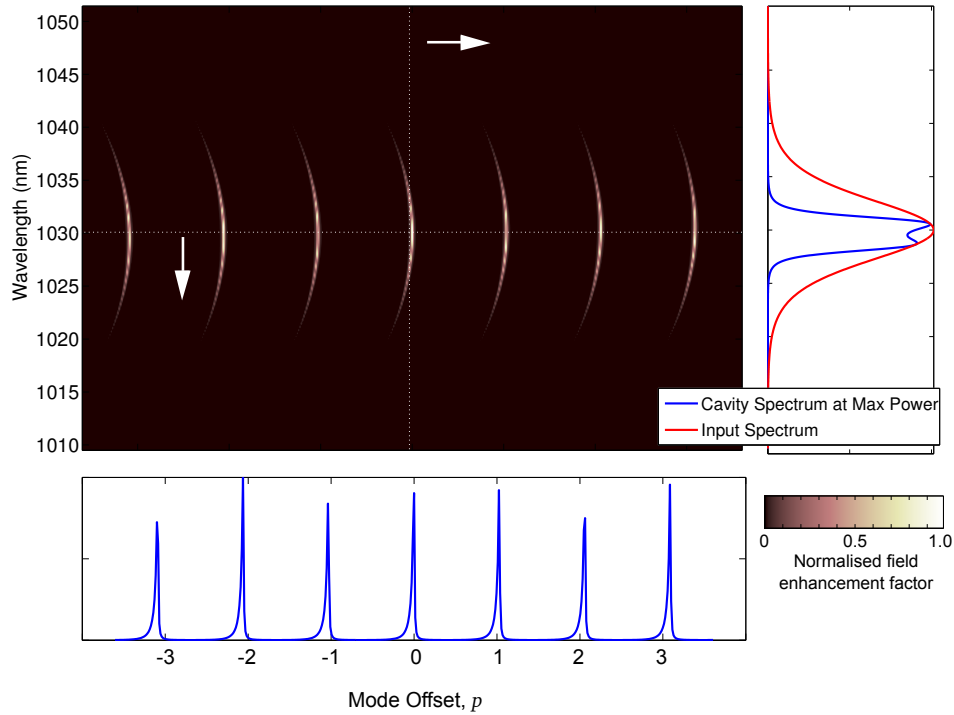


Figure 3.5: Main: Resonance map for a passive enhancement cavity seeded with an identical mode-locked oscillator to that of figure 3.4. The cavity has the same finesse, but now exhibits a net group delay of 10^4 fs². Right: Due to this mode bending, the maximum intracavity power is obtained for a cavity length that is slightly detuned from the resonance length for the central wavelength. Further, wavelengths at the edge of the laser bandwidth are not resonant, leading to a narrowing of the optical bandwidth circulating in the cavity. Bottom: There is an accompanying distortion of the intensity supported in the cavity as a function of cavity length, as previously reported in [41].

3.3. Cavity Design

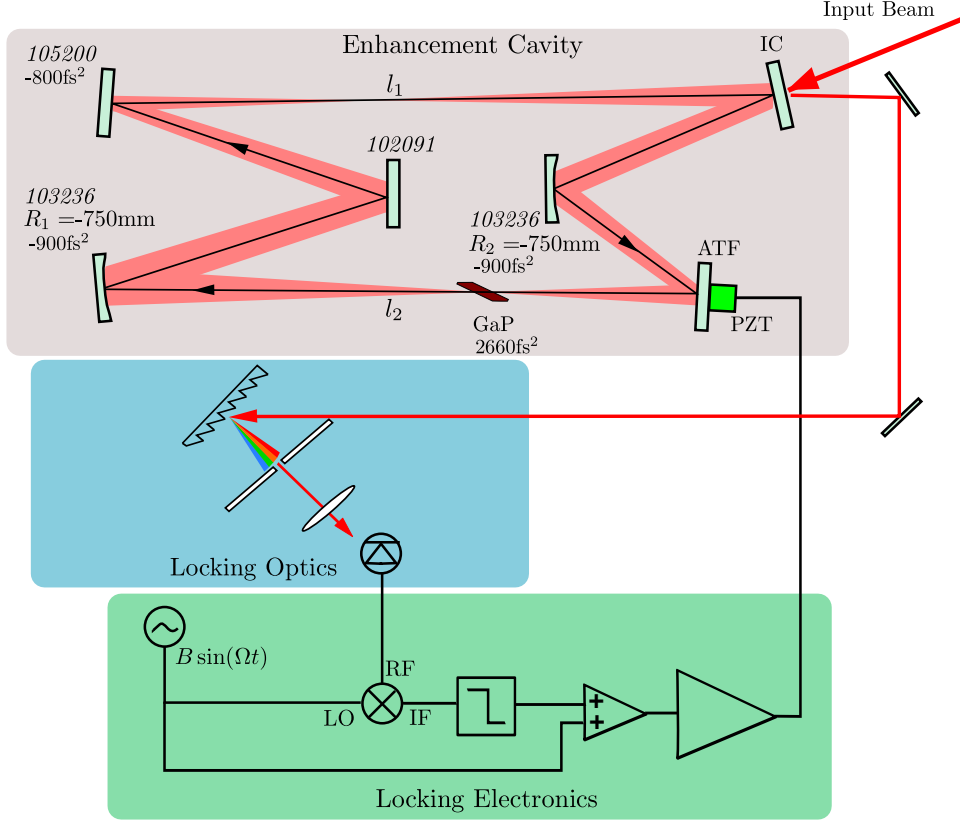


Figure 3.6: Experimental arrangement for the passive enhancement cavity. Layertec part numbers are given in italics. The cavity is a folded six mirror arrangement, with the input field incident on the low-reflectivity face of a Layertec input coupler (IC) which is changed to vary the cavity finesse. Mirror and IC specifications are given in table 3.1. The nonlinear gallium phosphide crystal is placed at the focus of two concave mirrors, having radius of curvature R_i as shown, so as to further increase the efficiency of the nonlinear process. The optical path length, as measured in air, between the two curved mirrors is l_1 along the path including the IC, and l_2 along the path including the nonlinear crystal. In order to maintain the resonance condition required by equation 3.9 a spectral portion of the power reflected by the optical cavity is monitored on a fast photodetector, and an appropriate locking scheme used to control the position of one of the cavity mirrors (ATF) using a piezoelectric actuator (PZT). This mirror has 7.75 mm diameter and 3 mm thickness so as to minimise the load on the PZT. The mirror itself has a specified power reflectivity of 99.99% at normal incidence, and negligible GDD.

3.3. Cavity Design

Firstly, to increase cavity stability over that of a planar mirror resonator and, secondly, to create an intracavity focus at which to place the nonlinear crystal, where the incident optical field intensity is increased, enhancing the efficiency of the difference frequency generation process. Various input couplers, as listed in table 3.1, were used in order to yield the required cavity finesse. An arbitrary number of flat mirrors can be used to yield the required beam path and dispersion characteristics, although it should be noted that the small losses from reflection at each mirror are not inconsiderable over many cavity roundtrips. In order to minimise reflection losses at the entry face, the nonlinear crystal is placed at Brewster's angle to the horizontally polarised incident optical beam. For gallium phosphide, this is calculated to be 72.2° for the optical wavelength of 1030 nm.

In selecting the curved mirrors and their separation, one must satisfy the resonator stability condition of equation 3.50. For the ring cavity considered here, we obtain

$$-2 \leq \frac{1}{R_1 R_2} [(R_1 + R_2)(l_1 + l_2) + l_1 l_2] \leq 0, \quad (3.24)$$

where l_1 and l_2 are the cavity lengths between the intracavity curved mirrors, as shown in figure 3.6, and R_1 and R_2 are the radii of curvature of these curved mirrors. The resonator used in this work uses two identical convex mirrors with radius of curvature 750 mm, such that a beam waist of $190 \mu\text{m}$ is formed halfway between the two curved mirrors. This spot size was chosen so as to maximise the efficiency of terahertz radiation generation in accordance with the findings of Zhang et al. [42] who found experimentally that terahertz generation was maximised when the radius of the optical spot size was comparable to the terahertz wavelength. For a frequency of 2 THz, a spot radius of $150 \mu\text{m}$ is therefore optimal. Numerical simulations of the Gaussian beam parameters (see section 3.5.1) for a cavity resonator produced the cavity design in figure 3.6.

Recall the conclusion of section 3.2 that, for a pulsed laser, the condition of resonance requires that the roundtrip phase of the cavity must satisfy the resonance condition, equation 3.8 for the entire pulse bandwidth. If

3.3. Cavity Design

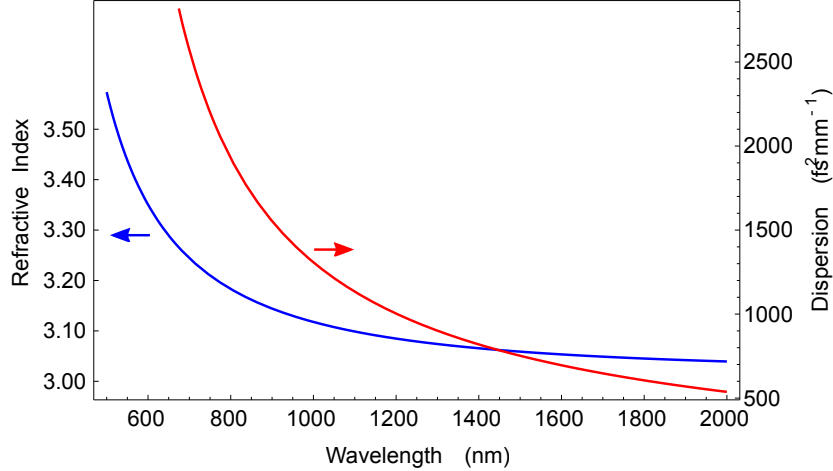


Figure 3.7: Refractive Index (in blue) and dispersion (in red) of gallium phosphide as predicted by the Sellmeier equation and data in [33].

there is no dispersion in the cavity, that is, the roundtrip phase of the cavity is the same for all optical frequencies, this is relatively easy to achieve with careful control of the cavity length. However, if there exist dispersive elements within the cavity, $\phi = \phi(\omega)$, and only those frequencies for which the resonance condition is satisfied will interfere constructively within the cavity, reducing the overall enhancement.

Gallium phosphide, by virtue of the absorption edge at 2.25 eV (550 nm), exhibits strong dispersion near 1030 nm, as shown in figure 3.7. In this work, we compensate for this large material dispersion by using dispersive Gires-Tournois interferometric (GTI) mirrors from Layertec corporation. GTI mirrors tune the design of the dielectric stack so as to impart a controlled amount of group delay dispersion on the reflected optical pulse. It is therefore necessary to establish the required crystal length prior to specifying the mirrors. Section 2.3 established that, for an optical pump of 1030 nm, gallium phosphide demonstrates a long coherence length of a few millimetres. So as not to excessively limit the terahertz bandwidth, a thickness of 2.1 mm is used in this work. Because the crystal is to be mounted at Brew-

3.3. Cavity Design

ster’s angle, the actual physical thickness is $2.1 \sin \theta_B = 2$ mm. The amount of intracavity group velocity dispersion (GVD) for the 2.1 mm optical path length is then 2625 fs^2 . Possible GTI mirrors for dispersion compensation are listed in table 3.1 along with the pertinent specifications. We see that, with the cavity configuration as shown in figure 3.6, it is possible to correct for the GVD of gallium phosphide to within 50 fs^2 .

Layertec part no.	Description	Power Reflectivity @ 1030 nm	GVD fs^2/mm
103236	-75cm ROC GTI	$>99.85\%$	-900 ± 100
105200	Planar GTI	$>99.9\%$	-800 ± 100
102091	Planar GTI	$>99.9\%$	<20
103143	5% IC	$95\pm 0.75\%$	<20
103141	1.6%IC	$98.4-0.3, \pm 0.1\%$	<20
102316	0.4%IC	$99.6\pm 0.1\%$	<20
108251	0.8%IC	$99.2-0.1, \pm 0.4\%$	<20
101147	0.5%IC	$99.5\pm 0.3\%$	N/A

Table 3.1: Part numbers and specifications for Layertec mirrors used in the design of the passive enhancement cavity. Group velocity dispersion (GVD) is given for the dispersive mirrors over the range 1030 ± 5 nm. Source: Layertec GmbH

3.3.2 Terahertz Output Coupling

The refractive index of gallium phosphide at a frequency of 1 THz is 3.24 [33]. This means that the critical angle for the terahertz radiation at the gallium phosphide-air boundary upon exiting the crystal is 18.2° . Careful consideration is therefore needed in order to increase the efficiency with which the terahertz radiation is coupled out of the nonlinear crystal so as to avoid high losses due to total internal reflection of the terahertz wave at the crystal boundary. A proposed scheme for doing this is shown in figure 3.8. Geometrical considerations show that, following total internal reflection at the crystal face through which the optical beam exits, (henceforth the ‘back’ face) the terahertz radiation propagates at 90° to the incident optical beam.

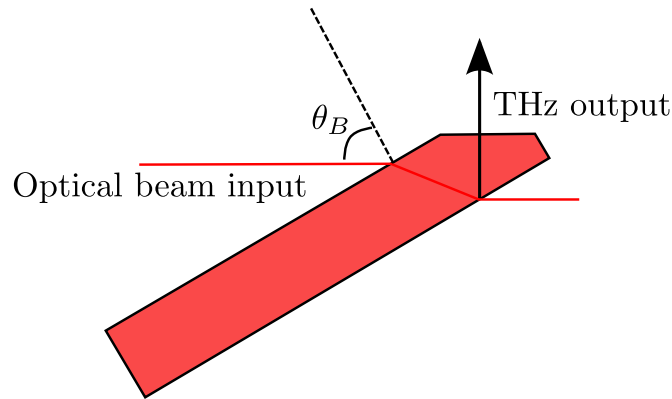


Figure 3.8: Crystal geometry for output coupling of the terahertz radiation. The end of the gallium phosphide crystal is cut at the Brewster angle to ensure the terahertz radiation, internally reflected at the back crystal face, is normally incident on the cut surface. In this way, output coupling efficiencies are maximised.

In order to maximise the output coupling efficiency of the terahertz radiation, the end of the gallium phosphide crystal was polished at the Brewster angle of 72.2° , such that the terahertz radiation is normally incident on the crystal boundary, as shown in figure 3.8.

A further consequence of the high refractive index of gallium phosphide in the terahertz is that the radiation will strongly diverge upon exiting the crystal. In order to collimate this output beam, a silicon lens is used [43], together with an off-axis parabolic mirror. Ray tracing models performed by Jesse Petersen [44] have shown that a silicon hypohemisphere of diameter 7.0 mm and radius of curvature 4.0 mm will give aplanatic imaging and move the virtual focus back to 17 mm behind the lens, reducing the maximum THz divergence half-angle to about 7° . This is calculated for THz radiation emitted halfway through the gallium phosphide crystal along the optical path. A 25.4 mm focal length, 90° off-axis parabolic mirror is used to collect and collimate the radiation. Ray tracing has shown that an off-axis mirror of 25.4 mm diameter is sufficient to collect the output radiation, and the compact size makes the physical arrangement within the cavity more

straightforward. The resulting ray traces are shown in figure 3.9

3.3.3 Cavity Performance Calculations

In section 3.2 it was shown that, for a cavity exhibiting a net roundtrip dispersion, such that there is a frequency dependence on the net roundtrip phase delay, there is a reduction in the spectral bandwidth that is able to resonate in the cavity. This leads to a reduction in the intracavity power. In the following section, we study in detail the optical characteristics of the cavity design of figure 3.6, and include explicitly the dispersion of the intracavity gallium phosphide crystal in which the terahertz radiation is generated.

The modelling work performed builds on that carried out by Jesse Petersen [44], in which the enhancement cavity is seeded with an unchirped, Gaussian input pulse of the form

$$\mathcal{E}_{inc}(t) = \sqrt{\frac{2}{\tau} \sqrt{\frac{2 \ln 2}{\pi}}} \exp\left(-2 \ln 2 \frac{t^2}{\tau^2}\right), \quad (3.25)$$

where the temporal power full width at half maximum (FWHM) is τ , and oscillations at the carrier frequency are neglected. $\mathcal{E}_{inc}(t)$ therefore describes the envelope of the incident pulse. Equation 3.25 normalises $\mathcal{E}_{inc}(t)$ such that

$$\int_{-\infty}^{\infty} |\mathcal{E}_{inc}(t)|^2 dt = 1, \quad (3.26)$$

thus the average power can be described in terms of the pulse energy, \mathbb{E}_{pulse} by

$$P(t) = \mathbb{E}_{pulse} |\mathcal{E}_{inc}(t)|^2. \quad (3.27)$$

Taking the Fourier transform of this input pulse yields the spectrum

$$\tilde{\mathcal{E}}_{inc}(\Omega) = \sqrt{\frac{\tau}{2\sqrt{\pi} \ln 2}} \exp\left(-\frac{\Omega^2 \tau^2}{8 \ln 2}\right) \quad (3.28)$$

where Ω is the frequency offset from the central frequency of the pulse, $\Omega = \omega - \omega_c$ due to the neglecting of the optical carrier frequency in 3.25.

3.3. Cavity Design

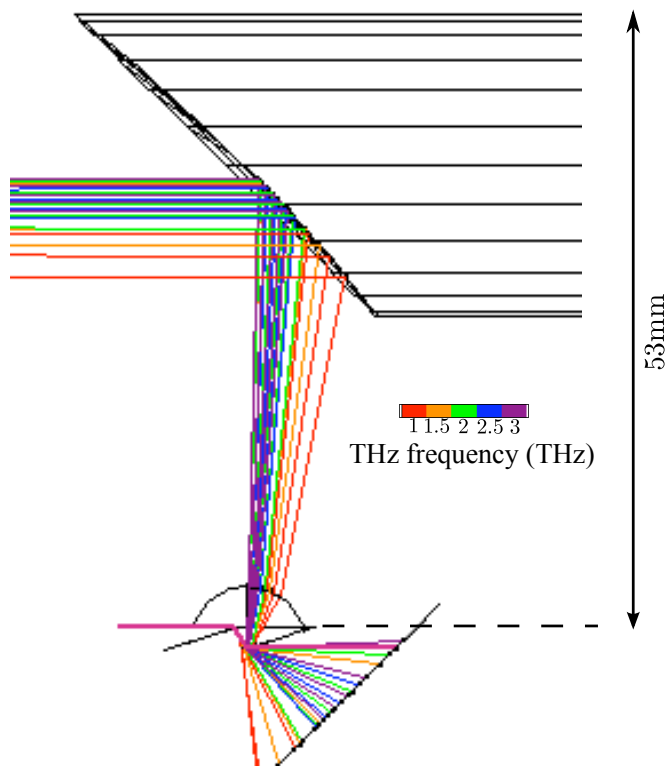


Figure 3.9: Optical design for output coupling of terahertz radiation for a gallium phosphide crystal at Brewster incidence. The silicon lens is a hypo-hemisphere of diameter 7 mm and radius of curvature 4 mm. The parabolic mirror for collimating the collected radiation is JANOS optic part no. A8037-101, with a 1" diameter and 1" focal length (2" effective focal length). Source [44].

3.3. Cavity Design

The effect of dispersion is incorporated by rewriting equation 3.15 in the form

$$\begin{aligned}\phi(\omega) &= k(\omega)d + \Phi_M(\omega) + \Phi_X(\omega) \\ &= \phi_0 + \Omega\phi'_0 + \delta\phi(\Omega) = 2m\pi.\end{aligned}\quad (3.29)$$

In this way, the constant part of the spectral phase shift accumulated from one cavity roundtrip is included in ϕ_0

$$\phi_0 = \phi(\omega_c) = k(\omega_c)d + \Phi_M(\omega_c) + \Phi_X(\omega_c). \quad (3.30)$$

Similarly, the part of the spectral phase that varies linearly with frequency Ω is included in ϕ'_0

$$\phi'_0 = \frac{d}{v_g} + \frac{d\Phi_M}{d\omega} + \frac{d\Phi_X}{d\omega}. \quad (3.31)$$

Finally, terms of higher order in Ω are grouped together in the term $\delta\phi(\omega)$,

$$\delta\phi(\omega) = \Omega^2 \frac{d^2\phi}{d\omega^2} + \Omega^3 \frac{d^3\phi}{d\omega^3} + \dots \quad (3.32)$$

The effects of GVD, TOD, and higher orders of dispersion are therefore all included in the final term $\delta\phi(\omega)$. Equation 3.17, where we now include dispersion, becomes

$$\omega_m = \frac{c}{d + c\phi'_0} (2\pi m - \phi_0 + \omega_c\phi'_0 - \delta\phi(\omega_m - \omega_c)), \quad (3.33)$$

any variation in the mode spacing of the cavity as a function of optical frequency is therefore attributed to $\delta\phi(\omega)$.

The cavity is assumed to be tuned to resonance such that, for the laser modes near the centre of the output spectrum (ie: where $\Omega = 0$), equation 3.23 is satisfied (The method used to control this is discussed in the following section). Therefore, for these frequencies, the mode offset, p is zero. In this case, these modes are perfectly coupled into the cavity and we expect maximum enhancement according to equation 3.9. Further, we assume that, close to line centre the cavity is dispersion compensated such that $\delta\phi(\omega) = 0$.

3.3. Cavity Design

Away from the central optical frequency we calculate the circulating complex amplitude spectrum by defining a complex cavity roundtrip transmissivity

$$h(\Omega) = RR_{ic} \exp(i\delta\phi(\Omega)) \quad (3.34)$$

and, following the methodology of equation 3.3, the intracavity circulating spectrum is calculated thus:

$$\begin{aligned} \tilde{\mathcal{E}}_{circ}(\Omega) &= \sqrt{1 - R_{ic}} \tilde{\mathcal{E}}_{inc}(\Omega) (1 + h(\Omega) + h(\Omega)^2 + \dots) \\ &= \frac{\sqrt{1 - R_{ic}}}{1 - h(\Omega)} \tilde{\mathcal{E}}_{inc}(\Omega). \end{aligned} \quad (3.35)$$

$\delta\phi(\omega)$ is calculated from fits to dispersion data provided by the mirror manufacturer, and Sellmeier data for the nonlinear crystal in [33]. Substitution of equation 3.28 into 3.35 then allows the calculation of intracavity pulse energy and duration, and hence a measure of the enhancement in terahertz generation.

Modelling Results

The first figure of merit we use to characterise the performance of the enhancement cavity is the enhancement bandwidth. Fitting the dispersion and reflectivity data for the mirrors used from Layertec GmbH and applying equation 3.35 we see that optical enhancements of 3000 times are possible for optical frequency bandwidths of around 2 THz. Further, from the plot in figure 3.10 we see that, whilst increasing the reflectivity of the input coupler may move the cavity finesse closer to that of the optimal impedance-matched case suggested by equation 3.9, the increased photon lifetime within the cavity increases the effect of small dispersion mismatches, leading to spectral narrowing and loss of optical bandwidth. Increasing the cavity finesse therefore reduces the bandwidth over which dispersion can be effectively compensated. This is undesirable in our case as the THz bandwidth relies on a large optical bandwidth within which to generate difference frequency components. We therefore expect a trade-off between greater amplification

3.3. Cavity Design

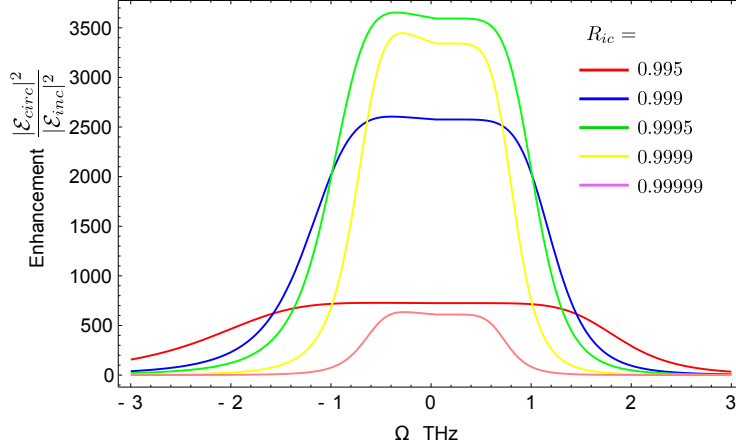


Figure 3.10: Effective enhancement of the range of optical frequencies effectively coupled into the enhancement cavity for various input couplers. The total material dispersion is 2620 fs^2 calculated for 2.14 mm of gallium phosphide. This is compensated for using mirrors from Layertec GmbH of two of part number 103236 and one of 105200, giving a total group velocity delay of 2600 fs^2 at the centre wavelength of 1030 nm. The net roundtrip GDD profile for the cavity is plotted in figure 3.11

of fewer optical modes, as in the case of a high finesse cavity, or reduced amplification of a broader bandwidth, achieved by spoiling the finesse with a lower reflectivity input coupler. In order to determine the optimal cavity configuration, the circulating spectrum is Fourier transformed into the time domain and fitted to Gaussian pulse in order to determine the resulting pulse duration. The resulting pulse broadening for the mirrors specified in figure 3.6 is shown for a 200 fs input pulse in figure 3.12. It is seen that the circulating pulse has approximately twice the duration of the input pulse, owing to the residual GDD of the cavity components, plotted in figure 3.11 as a function of optical frequency Ω .

In order to determine the optimum input coupler, a compromise will be made between amplification of a given frequency, and the total optical bandwidth. In order to study this, we refer to figure 3.13. It is seen that the pulse broadening remains modest, that is, below 20% for the 200 fs input

3.3. Cavity Design

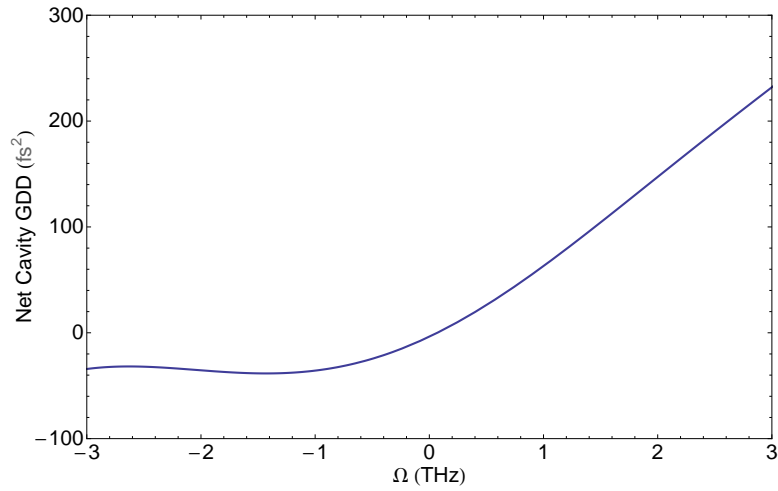


Figure 3.11: Calculated residual GDD of the cavity components for the cavity configuration shown in figure 3.6, and with an optical path length in the gallium phosphide crystal of 2.14 mm. Small negative phase delays are seen for $\Omega < 0$, where the total GDD is close to zero. As Ω increases above 0 a growing positive delay is calculated.

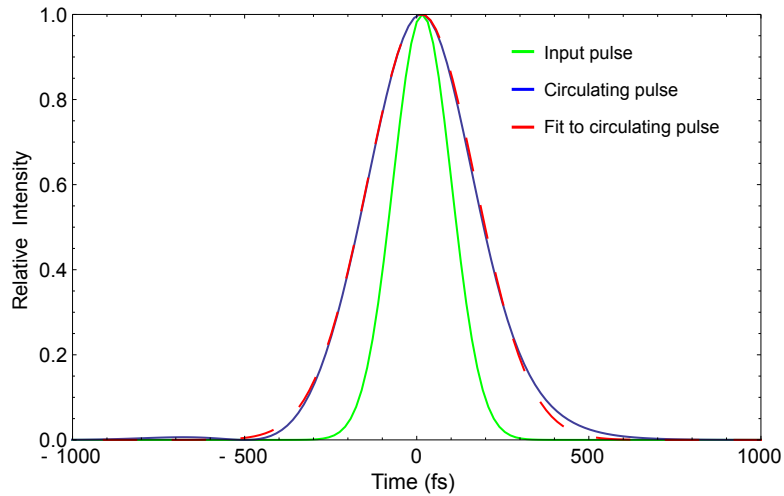


Figure 3.12: Estimated broadening of a 200 fs input optical input pulse within a passive enhancement cavity of the same design of that used in figure 3.10. The circulating pulse is fitted to a Gaussian pulse shape of full width half maximum 350 fs, shown by the dashed red line.

3.4. Cavity Locking

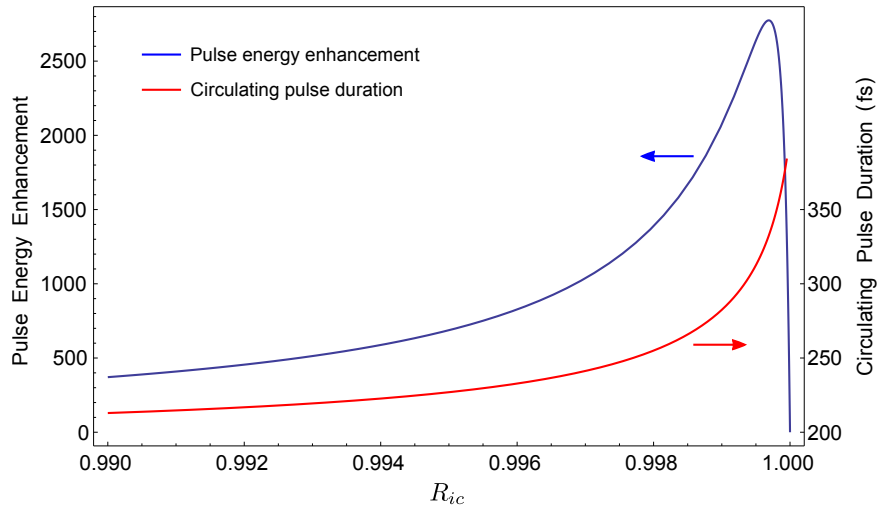


Figure 3.13: Circulating pulse energy enhancement and duration as a function of input coupler reflectivity for the cavity configuration of 3.12.

pulse, for input couplers of up to 99.8% reflectivity. Whilst this will come with a trade-off in enhancement, the lower cavity finesse will also increase the cavity linewidth, (indeed, it is exactly this broadening of the cavity linewidth that increases the optical bandwidth within the cavity) which, in turn, will lessen the demands on locking the cavity mode spacing with that of the laser.

An estimate of the ability of the feedback loop to lock a narrow enhancement cavity resonance to a comb element of the mode-locked laser can only be obtained with a detailed model of the electronic components used. Rather than model this numerically, we therefore choose to optimise the input coupling of the cavity experimentally.

3.4 Cavity Locking

The need for precise control of the longitudinal mode spacing of the passive enhancement cavity has been discussed previously. It was shown that the mode spacing of both the laser and enhancement cavity are determined by

3.4. Cavity Locking

the respective offset frequencies (ω_0 for the laser) and repetition rates (ω_{rep} for the laser). Further, due to the dependence of the frequency of the laser modes on the repetition time, as per equation 2.6, the laser frequencies will exhibit instabilities due to environmental factors such as temperature fluctuations and acoustic vibrations. It is therefore necessary to devise a method of stabilising the cavity modes with respect to the laser modes, such that the maximum amount of laser power is resonant in the cavity at all times. In order to ensure complete mode overlap, one must have independent control of both the relative offset frequencies, and the relative repetition rates. Whilst experiments achieving this have been demonstrated [28], it requires two high-speed servo loops and considerable amount of experimental complexity. Instead, we lock the average frequency of the enhancement cavity to that of the laser. In this way, we ensure the maximum possible power in the cavity for a given offset frequency mismatch and cavity dispersion, as shown in the projections along wavelength of the resonance map picture of figure 3.5.

We make use of a locking scheme developed by Hall et al. [45], originally developed for stabilizing the frequency of a laser by locking it to a passive reference cavity. In our adaptation of the technique, the length of the passive enhancement cavity is modulated at $\simeq 800$ kHz, hitherto referred to as the dither frequency, by driving a piezzo-electric actuator (PZT) onto which one of the cavity mirrors is fixed, as shown in figure 3.6. This frequency is chosen to be high enough so as to exceed any acoustic vibrations, but low enough such that the PZT still has some small response. The signal reflected by the enhancement cavity is spectrally resolved and a portion of the optical bandwidth focussed onto a fast photodiode. The bandwidth and center wavelength of the measured signal were tuned to give the maximum intracavity power. The measured signal is compared to a sample of the electronic signal used to drive the intracavity PZT, henceforth the local oscillator (LO) signal. For any spectral component of the measured optical signal, when the cavity is tuned to the exact resonance of equation 3.8, one observes a minimum in the reflection signal measured by the photodiode. Any deviation from this resonance condition will produce an increase in the

3.4. Cavity Locking

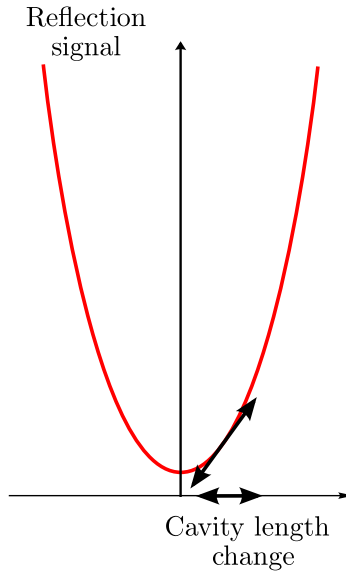


Figure 3.14: The reflection signal measured from the enhancement cavity near a position of resonance. The phase of the reflection signal with respect to a modulation in cavity length provides the direction in which one must adjust the cavity length in order to restore the resonance condition.

field reflected by the cavity at this particular wavelength. The minimum reflected power occurs when the greatest amount of power is supported in the cavity.

The locking scheme discussed here provides the necessary feedback in order to determine which direction to tune the cavity length so as to restore the resonance condition of equation 3.8. By modulating the cavity, the required sign of cavity length change is obtained by determining whether the reflected power measures in phase or 180° out of phase with the dither signal, as shown in figure 3.14. The experimental arrangement is shown in figure 3.6.

To understand the locking process in more detail, we write the electric field incident on the cavity as a monochromatic field of the form of equation 2.1

$$E_{inc}(t) = E_0 e^{-i\omega t} + c.c. \quad (3.36)$$

3.4. Cavity Locking

Whilst in the original technique, demonstrated by Hall et al. the length of the laser cavity (and therefore the phase of the input field) is modulated at the dither frequency, we have found modulation of the length of the enhancement cavity to give analogous results. Further, for the purposes of this discussion, we consider the modulation in frequency arising due to the translating mirror rather than the phase change directly. When modulated at a dither frequency Ω_{dit} with a modulation depth \mathcal{B} the modulated input field is given by

$$\begin{aligned}
 E_{inc}(t) &= E_0 e^{-i(\omega t + \mathcal{B} \sin \Omega_{dit} t)} \\
 &\simeq E_0 (1 + i\mathcal{B} \sin \Omega_{dit} t) e^{-i\omega t} \\
 &= E_0 \left(1 + \frac{\mathcal{B}}{2} (e^{i\Omega_{dit} t} - e^{-i\Omega_{dit} t}) \right) e^{-i\omega t} \\
 &= E_0 e^{-i\omega t} + \frac{E_0 \mathcal{B}}{2} \left(e^{i(\omega + \Omega_{dit})t} - e^{-i(\omega + \Omega_{dit})t} \right) \quad (3.37)
 \end{aligned}$$

We therefore have the familiar result that a monochromatic field at optical frequency ω , modulated at a frequency Ω_{dit} actually consists of three fields. One at the original optical frequency ω , and two optical sidebands at frequencies $\omega \pm \Omega_{dit}$.

The field reflected by the cavity is given by

$$\begin{aligned}
 E_{ref} &= E_T \sqrt{R} h - E_{inc} \\
 &= E_{inc} \left(\frac{\sqrt{R} (e^{-i\phi} - 1)}{1 - \sqrt{R R_{ic}} e^{-i\phi}} \right) \\
 &= E_{inc} F(\omega), \quad (3.38)
 \end{aligned}$$

where $F(\omega)$ is the cavity reflection coefficient. The remaining constants were defined in section 3.1, from which we recall E_T is the total field resonant within the cavity. The frequency dependence arises due to the fact that the roundtrip phase, $\phi = \frac{d\omega}{c} + \phi_M$, where ϕ_M is the phase change due to reflection at the cavity mirrors. Combining equations 3.37 and 3.38, we

3.4. Cavity Locking

obtain

$$E_{ref} = E_0 F(\omega) e^{-i\omega t} + \frac{E_0 \mathcal{B}}{2} F(\omega + \Omega_{dit}) e^{i(\omega + \Omega_{dit})t} - \frac{E_0 \mathcal{B}}{2} F(\omega - \Omega_{dit}) e^{i(\omega - \Omega_{dit})t}. \quad (3.39)$$

The power measured by the photodetector due to this reflected field is given by

$$\begin{aligned} P_{ref} &= |E_{ref}|^2 \\ &= E_0^2 |F(\omega)|^2 + \frac{E_0^2 \mathcal{B}^2}{2} |F(\omega + \Omega_{dit})|^2 + \frac{E_0^2 \mathcal{B}^2}{2} |F(\omega - \Omega_{dit})|^2 \\ &\quad + \frac{E_0^2 \mathcal{B}}{2} [F(\omega) F^*(\omega + \Omega_{dit}) e^{-i\Omega_{dit}t} + F^*(\omega) F(\omega + \Omega_{dit}) e^{i\Omega_{dit}t} \\ &\quad - F(\omega) F^*(\omega - \Omega_{dit}) e^{i\Omega_{dit}t} - F^*(\omega) F(\omega - \Omega_{dit}) e^{-i\Omega_{dit}t}] \\ &\quad + \text{terms in } 2\Omega_{dit}t. \end{aligned} \quad (3.40)$$

Providing the modulation depth is sufficiently small that $\frac{B}{2} \ll E_0$ we may neglect the terms in $2\Omega_{dit}t$ on the grounds they are small in amplitude. Further, the use of a rf mixer allows the rejection of the non time-varying dc terms such that only the terms having a frequency equal to that of the local oscillator (LO) signal are measured. The measured dc signal output at the mixer can then be rewritten

$$\begin{aligned} S &= E_0^2 \mathcal{B} [\text{Re} \{F(\omega) F^*(\omega + \Omega_{dit})\} \cos \Omega_{dit}t + \text{Im} \{F(\omega) F^*(\omega + \Omega_{dit})\} \sin \Omega_{dit}t \\ &\quad - \text{Re} \{F^*(\omega) F(\omega - \Omega_{dit})\} \cos \Omega_{dit}t - \text{Im} \{F^*(\omega) F(\omega - \Omega_{dit})\} \sin \Omega_{dit}t]. \end{aligned} \quad (3.41)$$

We set the phase of the LO signal with respect to the field modulation such that the imaginary term is measured. In this case, the detected error signal is

$$S = E_0^2 \mathcal{B} [\text{Im} \{F(\omega) F^*(\omega + \Omega_{dit}) - F^*(\omega) F(\omega - \Omega_{dit})\}]. \quad (3.42)$$

The resulting error signal is calculated and plotted in figure 3.15.

3.4. Cavity Locking

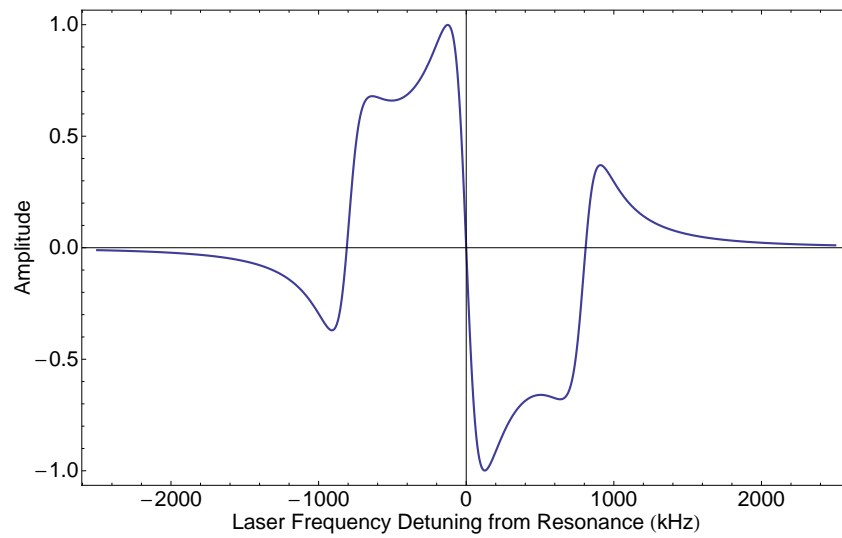


Figure 3.15: Calculated error signal for a passive enhancement cavity having a finesse of $\mathcal{F} = 2 \times 10^5$ as a function of laser frequency detuning from the exact resonance condition of equation 3.8. In this example, the dither frequency, Ω_{dit} is 800 kHz and the optical wavelength is 1030 nm.

3.4. Cavity Locking

If the finesse of the cavity is sufficiently high, and the dither frequency sufficiently large such that the sidebands fall at frequencies for which $F(\omega \pm \Omega_{dit}) \simeq -1$ then only the field at the optical frequency is coupled into the cavity. The power measured at the photodetector, as per equation 3.40, becomes

$$\begin{aligned}
 \simeq P_{ref} &\simeq E_0^2 \left(|F(\omega)|^2 + \frac{\mathcal{B}^2}{2} \right) \\
 &+ \frac{\mathcal{B}E_0}{2} (2iF(\omega) \sin \Omega_{dit}t - 2iF^*(\omega) \sin \Omega_{dit}t) \\
 &= E_0^2 \left(|F(\omega)|^2 + \frac{\mathcal{B}^2}{2} \right) - 2\mathcal{B}E_0 \text{Im} \{ F(\omega) \sin \Omega_{dit}t \}. \quad (3.43)
 \end{aligned}$$

Again, the dc term is rejected by the rf mixer and we measure $S \propto \sin \Omega_{dit}t$.

On resonance, the phase of the field in the cavity at the input coupler is $\phi = 2m\pi$ where m is some integer. If the cavity is shifted away from resonance by some fraction, δl , of the optical wavelength, we obtain

$$\phi \simeq 2m\pi + 4\pi \frac{\delta L}{\lambda}. \quad (3.44)$$

We can then re-write the reflection coefficient of the cavity as

$$\begin{aligned}
 F(\delta L) &\simeq \frac{\sqrt{R}}{1 - \sqrt{R}R_{ic}} \left(4\pi i \frac{\delta L}{\lambda} \right) \\
 &\simeq i \frac{4\mathcal{F}}{\lambda} \delta L, \quad (3.45)
 \end{aligned}$$

such that

$$S \simeq -\frac{8\mathcal{B}E_0\mathcal{F}}{\lambda} \delta L \quad (3.46)$$

Under these conditions, S therefore provides a control signal that varies linearly with the detuning of the cavity from resonance. This control signal is used in a servo loop to control the piezzo-mounted mirror, as shown in figure 3.6. In this way, the average resonance frequency of the enhancement cavity tracks that of the mode-locked laser with which it is seeded, ensuring that the maximum possible power resonates inside the cavity.

3.5. Spatial Mode-matching into the Optical Resonator

$w(z) = w_0 \sqrt{1 + \left(\frac{z}{z_0}\right)^2}$	Beam radius at position z
$R(z) = z \left[1 + \left(\frac{z_0}{z}\right)^2\right]$	Beam wavefront radius of curvature at position z
$\zeta(z) = \tan^{-1} \left(\frac{z}{z_0}\right)$	Guoy phase-shift
$w_0 = \sqrt{\frac{\lambda z_0}{\pi}}$	Beam waist
$2z_0 = \frac{2\pi w_0^2}{\lambda}$	Depth of focus

Table 3.2: Properties of a Gaussian beam

3.5 Spatial Mode-matching into the Optical Resonator

3.5.1 Gaussian Mode of the Optical Resonator

It is well known (see, for example, [46]) that the electric field circulating in an optical resonator has the solution of a Gaussian beam

$$E_0(\vec{r}) = A \frac{w_0}{w(z)} \exp\left[-\frac{x^2 + y^2}{w^2(z)}\right] \exp\left[ik \frac{x^2 + y^2}{2R(z)}\right] \exp[ikz] \exp[i\zeta(z)], \quad (3.47)$$

where A is the amplitude of the electric field in the polarisation direction, $w(z)$ is the beam waist at position z . This leads to the definition of the Gaussian beam parameters in table 3.2.

It is common to further simplify equation 3.47 by defining the q -parameter, $q(z)$ of the Gaussian beam

$$\frac{1}{q(z)} = \frac{1}{R(z)} + i \frac{\lambda}{\pi w^2(z)}. \quad (3.48)$$

3.5. Spatial Mode-matching into the Optical Resonator

It is this q -parameter, having units of metres, that we may propagate through a system of optical components using the commonly used ABCD matrix transfer method, in which the effect of each optical component is described by its specific ABCD matrix, (see, for example, [46]) and the ABCD matrix for the entire optical system, in this case, the enhancement cavity, is given by the matrix product of the ABCD matrices of its components. For a given system of optical components, the q -parameter transforms as

$$q_2 = \frac{Aq_1 + B}{Cq_1 + D}, \quad (3.49)$$

where the values of A , B , C , and D are determined by the specific optical components in the cavity. By requiring that the cavity is stable, that is, that the Gaussian beam parameters of the field contained within the cavity are the same for N round trips as for $N + 1$ round trips, we require that $q_f = q_i$. Further, we require that the determinant of the cavity ABCD matrix be unity. Equation 3.49 therefore gives rise to the familiar resonator stability condition,

$$\frac{1}{2}|A + D| \leq 1. \quad (3.50)$$

It is this condition that determines the appropriate mirror radius of curvature for a given cavity length.

Having established the conditions for a stable resonator, the parameters in table 3.2 can be used to determine the position of the intracavity focal planes, as well as the beam spot sizes at these focal points. Further, the beam q -parameter can be calculated for any point within the enhancement cavity, in particular, we seek to evaluate the q -parameter at the cavity side of the input coupler, such that the q -parameter of the input beam may be manipulated to match it, therefore maximizing the power from the input beam that is coupled into the Gaussian mode of the enhancement cavity. This will be the subject of section 3.5.2.

3.5.2 Beam Profiling

In order to determine the appropriate mode-matching solution for the enhancement cavity work, and the optimum focussing arrangement for the single pass terahertz generation and electro-optic sampling experiments, it was first necessary to determine the Gaussian beam parameters of the field input to the experiment. As the same laser output was used for the case of the enhancement cavity, and for the terahertz generation in the dual-comb spectrometer work, it is sufficient to determine the beam parameters at the output of the compression stage, from which appropriate solutions can be found for each case. An additional set of beam parameters were determined for the laser used as the local oscillator in the dual-comb spectrometer experiments. In order to determine the Gaussian beam parameters, a scanning knife-edge technique [47] was used to determine the beam diameter at several points through the focal region following a lens of known focal length. The clip levels required to block 10% and 90% of the beam power at various points along the optical axis are measured. Following the analysis in [47] for a TEM₀₀ Gaussian beam, the beam waist is then calculated according to

$$2w_0 = \frac{4D_c}{2.563}. \quad (3.51)$$

Figure 3.16 shows the result of such a knife edge measurement, where a 250 mm converging lens is used to focus the beam down to a spot. We define the plane in which this lens is positioned as the compressor output plane. It is seen that the beam waist produced at the focus of this lens is 120 μm , and that the Rayleigh range, that is, the range at which the on-axis intensity falls to half that at the focus, is found to be 20 mm. The half-angle divergence of the beam is found to be 4.5 mrad. We note that this gives an M^2 value, the ratio of the waist-diameter to divergence product to that of the ideal Gaussian beam, of 1.7, which is a typical value for a fibre laser.

Applying the relations in table 3.2 and finding the q-parameter at the focus to be purely imaginary, $\frac{1}{q(\text{focus})} = i\frac{\lambda}{\pi w_0^2}$, we then propagate this q parameter back through to the entry face of the lens using equation 3.48 to

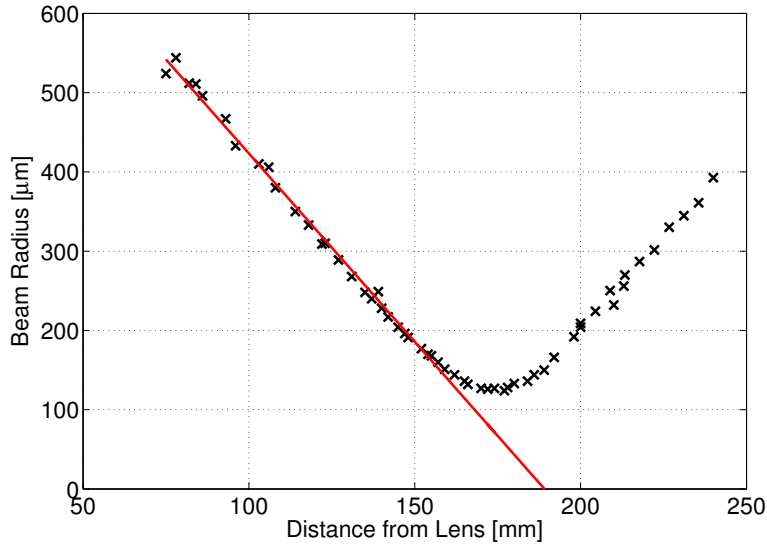


Figure 3.16: Beam waist profile following a 250 mm focal length converging lens, as measured using the knife-edge beam-clipping technique as described in [47].

find

$$q(\text{compressor output}) = -0.17 - 0.04i \text{ metres.} \quad (3.52)$$

This is used as a baseline q -parameter for calculating the required focusing optics, both for mode-matching into the enhancement cavity, and for creating the optimum spot size in the gallium phosphide waveguide for the dual-comb spectrometer work.

3.5.3 Mode-matching Solution

In the case of the cavity depicted in figure 3.6, the required q -parameter at the input coupler is found by first determining the q -parameter at either of the curved mirrors, by recognising that the wavefront radius of curvature must match that of the mirrors, and that the focal points must be halfway between the two curved mirrors in each case. The same method as before is

3.6. Characterisation of the Passive Enhancement Cavity - Results and Analysis

then used to propagate this q -parameter to the input coupler. One obtains

$$q(\text{cavity input}) = -0.52 + 0.59i. \quad (3.53)$$

The task of mode-matching therefore becomes to find some system of optics, having transfer matrix $\begin{pmatrix} A & B \\ C & D \end{pmatrix}$ such that

$$q(\text{cavity input}) = \frac{Aq(\text{compressor output}) + B}{Cq(\text{compressor output}) + D}. \quad (3.54)$$

There are, of course, an infinite number of solutions to this problem given lack of restraint on components available and space, although it should be noted that it is desirable to minimise transmission losses by reducing the number of components as much as possible. For the case here, a pair of lenses of focal lengths 1050 mm and 750 mm were positioned 2.18 and 2.04 metres before the cavity input coupler respectively. The total optical path length between the compressor output plane and input coupler is set to 2.5 metres. Both the lenses used were anti-reflection coated (Newport coating reference AR.16) at 1030 nm to minimise reflection losses. A schematic of this arrangement is shown in figure 3.17.

3.6 Characterisation of the Passive Enhancement Cavity - Results and Analysis

It is clear that enhancement of the optical pulse within the cavity relies on the precise control of a number of factors, namely the cavity finesse, the roundtrip dispersion of the cavity, the mode-matching of the input beam into the stable Gaussian mode of the resonator, and the satisfaction of the resonance condition, equation 3.9. In order to determine satisfactory performance of the measures taken to control these factors, it is desirable to be able to measure them independently.

In accordance with equation 3.13, the enhancement factor of the cavity is defined as

$$\text{Enhancement} = \frac{P_{cav}}{P_{in}} \quad (3.55)$$

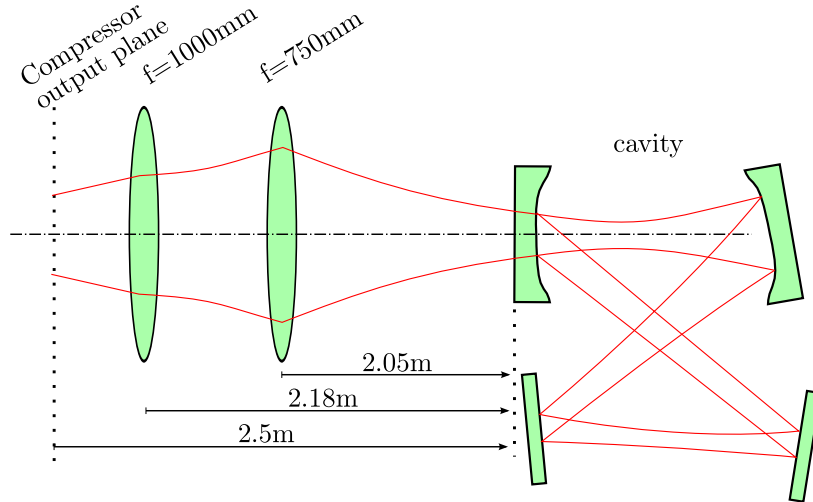


Figure 3.17: Schematic of optics used for mode-matching into the passive enhancement cavity. Some cavity mirrors omitted for clarity.

where P_{cav} is the optical power circulating within the cavity, and P_{in} is the power incident on the input face of the input coupler. It is possible to measure the former using the optical power transmitted by any one of the cavity mirrors due to the non-unity reflectivity, and measurements of the transmissivity of the mirror performed without the cavity. Both the cavity measurement and mirror calibration is performed with a conventional optical power meter, which provides only a measure of the optical power integrated over the entire optical bandwidth, and lacks sensitivity to small changes in the mirror reflectivity. The following section discusses a number of methods used to analyse the cavity in more detail.

3.7 Measurement of the Cavity Finesse

The expected enhancement factor of the cavity depends critically on the cavity finesse, as derived in equation 3.6. The finesse itself is determined by the reflectivity of the cavity mirrors. An accurate measurement of the

3.7. Measurement of the Cavity Finesse

finesse, however, is difficult to attain by simply measuring the mirror reflectivities individually and calculating, as per equation 3.6, as the finesse, and therefore the enhancement factor, changes dramatically with only small changes in mirror reflectivity. Instead, we use a method outlined in [48] to measure the finesse directly.

The length of the enhancement cavity is rapidly swept using the intracavity piezoelectric actuator, such that the cavity is effectively swept through a resonance, allowing light into the cavity, and then rapidly off resonance, preventing further input of light. As the cavity is swept, the transmission through one of the cavity mirrors is monitored with a fast photodiode, where one observes the gradual ringing down of the pulse as it circulates within the cavity. Consider further the analysis of [48], in which the cavity length is increased by translating the intracavity mirror at velocity v , such that the length at time t follows

$$L(t) = L_0 + vt. \quad (3.56)$$

Following the same methodology of equation 3.3, the field transmitted by the cavity as a function of time is the infinite sum of the partial fields $E_n(t)$, where $E_n(t)$ has made $(n - 1)$ roundtrips of the cavity. The total field transmitted is therefore given by

$$E_{out}(t) = T_{out} \sum_{n=1}^{\infty} E_n(t) = T_{out} \sum_{n=1}^{\infty} E_{in} T R^{n-1} e^{i\phi_n(t)}, \quad (3.57)$$

where $\phi_n(t)$ is the phase shift of the partial field $E_n(t)$, and T_{out} is the field transmissivity of the cavity mirror through which the leak is measured. Accounting for the Doppler shift in frequency of $\left(1 - \frac{2v}{c}\right)$ at each reflection

3.7. Measurement of the Cavity Finesse

at the moving mirror, $\phi_n(t)$ can be written

$$\begin{aligned}
 \phi_n(t) = & \phi_1(t) + \frac{\omega}{c} \left(1 - \frac{v}{c}\right) (2d_0 + vt) \\
 & + \frac{\omega}{c} \left(1 - \frac{v}{c}\right)^2 (2d_0 + 3vt) \\
 & + \frac{\omega}{c} \left(1 - \frac{v}{c}\right)^3 (2d_0 + 5vt) \dots \\
 & + \frac{\omega}{c} \left(1 - \frac{v}{c}\right)^{n-1} (2d_0 + (2n-3)vt). \tag{3.58}
 \end{aligned}$$

Under the assumptions that $v \ll c$, and $vt \ll L_0$ such that we can neglect terms in $\left(\frac{v}{c}\right)^2$, we can rewrite this expression as

$$\phi_n(t) = (2n-1)\phi_1(t) - \pi n(n-1) \frac{\Omega_v}{\Omega_{FSR}}, \tag{3.59}$$

where $\phi_1(t) = 2\pi \frac{L(t)}{\lambda}$, $\Omega_v = \frac{2v}{\lambda}$, and $\Omega_{FSR} = \frac{c}{L_0}$ is the cavity free spectral range. For a high finesse cavity, the photon lifetime, $\tau = \frac{\mathcal{F}}{2\pi\Omega_{FSR}}$ becomes large, such that, on average, each pulse completes many roundtrips of the cavity, and the discrete sum of equation 3.57 can be closely approximated by the continuous integral. Taking the square of the final result, so as to find the measured quantity of the intensity, yields

$$I_{out}(t) \propto e^{-\frac{t}{\tau}} |\operatorname{erfc}[\Lambda(t)]|^2, \tag{3.60}$$

where $\operatorname{erfc}[\Lambda(t)]$ is the complimentary error function, and $\Lambda(t)$ is a complex function of the cavity finesse, free spectral range, and sweep parameters [48]:

$$\Lambda(t) = \frac{1-i}{2\sqrt{2}} \left(\frac{\Omega_{FSR}}{\pi\Omega_v}\right)^{\frac{1}{2}} \frac{\pi}{\mathcal{F}} - \frac{1+i}{2\sqrt{2}} \left[\left(\frac{\Omega_{FSR}}{\pi\Omega_v}\right)^{\frac{1}{2}} \times 2\phi_1(t) - \left(\frac{\Omega_{FSR}}{\pi\Omega_v}\right)^{\frac{1}{2}} \right]. \tag{3.61}$$

The decay of the swept cavity is therefore proportional to the decay of the static cavity, multiplied by the $|\operatorname{erfc}[\Lambda(t)]|^2$ term, which manifests itself as a

ringing effect as the cavity is swept through the resonance point. By fitting the decay of the cavity, one can therefore determine the photon lifetime, τ , from which it is a trivial matter to determine the finesse. The first and second maxima of equation 3.60 occur with a temporal separation

$$\Delta t = \frac{\sqrt{5} - 1}{\sqrt{2}\Omega\Omega_{FSR}}. \quad (3.62)$$

In order that the maxima are spaced such that a reliable fit to the cavity decay can be obtained, it is desirable that this time is less than the decay time τ , which requires the cavity mirror be swept with a velocity, v , that satisfies

$$v \gg \frac{15c\lambda}{\mathcal{F}^2 L_0}. \quad (3.63)$$

3.7.1 Results of Finesse Measurements

The cavity was configured as in figure 3.6, with a 0.5% input coupler, and without the nonlinear crystal. It should be noted that, as the cavity is designed to be dispersion compensated with the nonlinear crystal, the ‘empty’ cavity has a total average group delay dispersion of $\sim -2650 \text{ fs}^2$. Therefore, in order to avoid distortion of the ring down data due to different wavelengths arriving with a different roundtrip phase-shift, the measurement was performed with a continuous wave laser at 1064 nm. Figure 3.18 shows the result of measuring the finesse via such a ‘ringdown’ method as described above. For the cavity configuration shown, one expects a finesse of ~ 970 , as predicted by equation 3.6. The exponential fit gives a finesse of 930, in good agreement with the predicted value, demonstrating that, for the seed wavelength of 1064 nm, the mirror reflectivities are as specified. It should be noted that the first maxima shown in figure 3.18 is excluded from the exponential fit, as it typically displays a level higher than that predicted. This is likely due to imperfect mode-matching of the input beam, meaning that some of the optical power escapes the cavity in the $\sim 1\mu\text{s}$ taken for the swept cavity to hit the second resonance. For comparison, the results of a similar measurement where the input coupler has been replaced with one

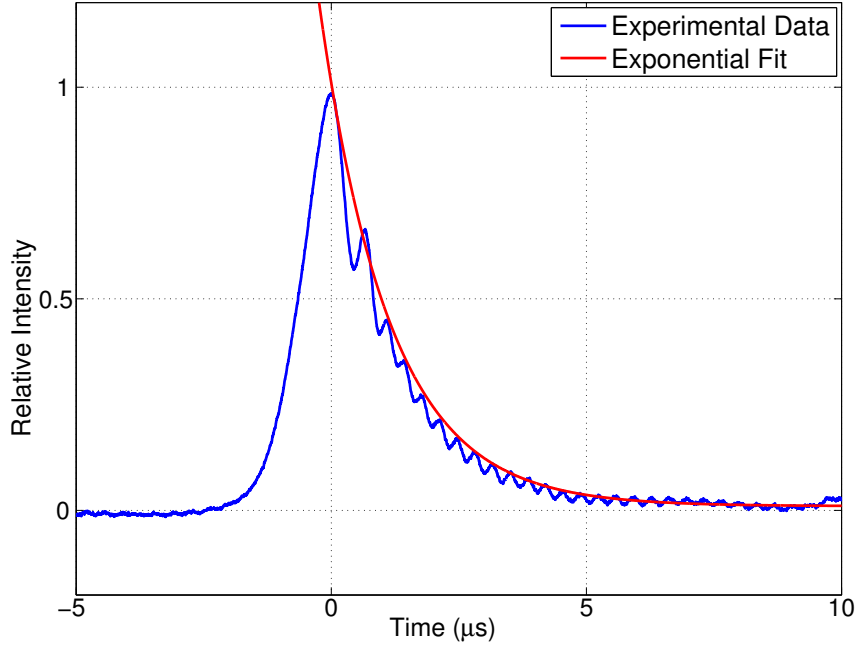


Figure 3.18: Ring down measurement for the passive enhancement cavity without the gallium phosphide crystal. An exponential fit is shown for a photon lifetime of $1.4\mu\text{s}$, or a finesse of ~ 935 . This corresponds well with the expected cavity finesse of 960 for the six mirror cavity with each mirror having $R = 0.9997$ and $R_{ic} = 0.995$, or a transmissivity of 0.5%. For this data, the cavity was swept with mirror velocity of 3 mm/s, in accordance with equation 3.63.

for which $R_{ic} = 0.998$ or transmissivity of 0.2%, is given in figure 3.19. In this case, the predicted finesse is ~ 1800 , in good agreement with the 1730 measured.

3.8 Enhancement Bandwidth of the Cavity

For the cavity finesse indicated in figure 3.18, one expects an optical build-up factor of ~ 470 , as predicted by equation 3.13. It was possible to obtain an intracavity intensity of 290 mW for an input power of 1.2 mW, indicating

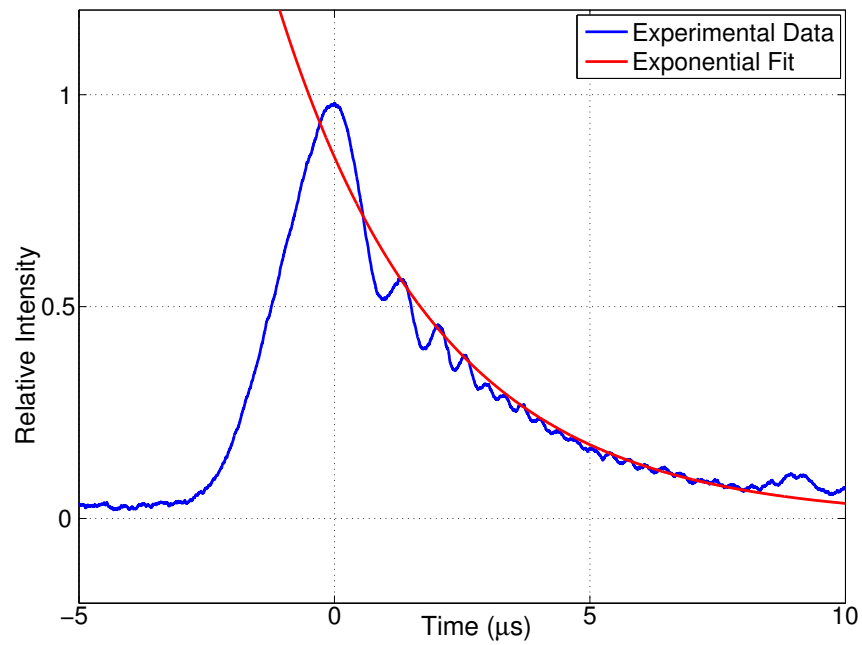


Figure 3.19: Plot of data as for figure 3.18 where the input coupler has been changed to a transmissivity of 0.2%, giving a predicted finesse of 1800. The exponential fitted is for a photon lifetime of $2.7\mu\text{s}$, giving a measured finesse of 1730.

3.8. Enhancement Bandwidth of the Cavity

an amplification of 240, about half of the theoretical maximum predicted by equation 3.6 with the specified mirror reflectivities. This shortcoming in performance is attributed to imperfect mode-matching of the input beam. Indeed, only a single lens was used to give an approximate solution to the mode-matching problem for this CW test laser. Due to the discussions set forth in section 3.2, it is not reasonable to expect similar levels of enhancement for the broadband optical pulse of a mode-locked oscillator for this cavity configuration, due to the large net dispersion of the cavity in the absence of the nonlinear crystal. However, placing the nonlinear crystal at the cavity focus as in figure 3.6, and seeding the cavity with the broadband optical pulses described in section 2.4 resulted in minimal build-up, in spite of the predicted net cavity dispersion being close to zero.

In order to study the effect of dispersion on the cavity enhancement factor for the broadband mode-locked oscillator, and to verify that the GTI mirrors had sufficient group delay to compensate for that due to the material dispersion of the nonlinear gallium phosphide crystal, the crystal was removed, and SF11 glass substrates of various thickness were placed at the Brewster's angle of 60° within the cavity. The total dispersion of the enhancement cavity was then varied according to the optical path length in SF11 glass per roundtrip of the cavity. As was shown in section 3.10, for a cavity with non-zero roundtrip group delay dispersion, the optimum build-up of a broadband pulse is achieved for a cavity configuration that is slightly 'overcoupled'. That is, that the transmissivity of the input coupler is greater than that suggested by the impedance-matching condition of equation 3.9 alone. For the present work, the transmissivity of the input coupler was increased to 1%, thereby allowing sufficient enhancement of the field within the cavity such that a leak through one of the high reflectivity cavity mirrors could be used to measure the stored spectral bandwidth within the cavity, and estimate the intracavity build-up by measurement of the power transmitted through the cavity mirror. In this case, the finesse of the cavity is reduced to ~ 500 , and the predicted optimum enhancement is 300.

The amount of SF11 used and the resulting nominal cavity dispersion based on the Sellmeier coefficients given in [49] are given in table 3.3. Note

that the 17.7 mm thick piece of SF11 glass was chosen specifically to have the same group delay as 2.1 mm of gallium phosphide at Brewster incidence.

In order to illustrate the effect of the cavity dispersion on the obtained enhancement factor, we include in table 3.3 the 10 dB bandwidth of the spectra resonant inside the cavity upon locking of the cavity average frequency to that of the mode-locked laser used to seed it. It is seen that higher enhancement factors are produced for greater resonant spectral bandwidths, as predicted by section 3.2. Close to zero nominal cavity group delay dispersion, the spectrum stored in the enhancement cavity is close in bandwidth to that of the input spectrum. As the cavity dispersion is increased, either positively or negatively, the dependence of roundtrip phase delay on wavelength leads to spectral narrowing, and a loss of intracavity power. In figure 3.20, we plot the measured enhancement against the estimated net group delay of the cavity, along with the measured 10 dB resonant spectral bandwidth. For comparison, the enhancement and 10 dB bandwidths predicted by the resonance map calculations of section 3.2 are included. It is seen that the measured enhancement decreases with increasing net cavity group delay in a manner similar to that calculated. That the measured values fall below those calculated for non-zero cavity group delays may be attributed to the neglecting of third and higher order dispersion in the calculations. Figure 3.20 also shows the strong correlation between the resonant spectral bandwidth and the enhancement, the measured resonant spectral bandwidth being in excellent agreement to the calculated values.

Table 3.3: Optical enhancement, resonant bandwidths, and net cavity dispersions for various cavity configurations used to verify the effect of dispersion on the available enhancement. The enhancement and bandwidth achieved with the ‘empty’ cavity (where the beam propagates only in air) are also given for reference. The seed spectrum incident on the cavity has a 10 dB bandwidth of 13.8 nm. Note that the theoretical maximum enhancement for this cavity configuration, with the 1% input coupler, is $\simeq 300$. The absorption of SF11 glass at 1030 nm [49], combined with slight errors in mode-matching, are likely responsible for the shortfall in performance, even for cavity configurations having minimal roundtrip dispersion.

Thickness of SF11 Glass (mm)	Optical Path Length in SF11 at Brewster’s Angle (mm)	Net. Cavity GDD at 1030 nm (fs ²)	Measured Enhancement Factor	10 dB Bandwidth of Resonant Spectrum (nm)
0	0.00	-2625.00	10.5	4.50
14.0	16.05	-550.70	18.9	6.32
16.8	19.33	-126.92	26.5	10.4
17.7	20.32	0.96	45.5	13.6
31.6	36.38	2075.26	9.5	5.63
Seed	-	-	-	13.8

3.8. Enhancement Bandwidth of the Cavity

Figure 3.21 compares the optical spectrum supported within the enhancement cavity to the input spectrum, where now the gallium phosphide crystal is placed at the intracavity focus. Minimal spectral narrowing is seen when the dispersion of the gallium phosphide contributes to the net group delay dispersion of the cavity. Indeed, in this case, the 10 dB bandwidth of the supported spectrum is 13.2 nm, as opposed to the 13.8 nm of the input spectrum.

The lack of spectral narrowing observed in the case where the nonlinear crystal is placed at the cavity focus suggests that the dispersive GTI mirrors are sufficiently compensating for the material dispersion of the crystal, as was the intent. However, for this cavity configuration, the optical power enhancement was reduced to around a factor of 6. In the absence of significant spectral narrowing, this is attributed to a reduced cavity finesse. Indeed, attempts to measure the finesse via the method outlined in section 3.7 proved unsuccessful, due to the difficulty in driving the cavity mirror with a velocity that satisfies equation 3.63 for this reduced finesse.

Recall the conclusions of section 3.2 and, in particular, figure 3.10, where it was seen that, for given non-zero net cavity dispersion, increasing the cavity finesse results in a narrower range of optical bandwidths being supported in the cavity. Indeed, the resonance map calculations for a cavity showing a 7% roundtrip loss produce a 10 dB resonant spectral bandwidth that varies with cavity group delay as in the black line of figure 3.20, which shows the reduced sensitivity of the resonant bandwidth to cavity group delay under such conditions. The observation of minimal spectral narrowing for the case of a cavity of such low finesse as figure 3.21 should therefore not be taken as proof that the cavity is sufficiently dispersion-compensated to expect significant amplification of large optical bandwidths at higher finesse. Whilst methods of precisely determining the cavity dispersion have been demonstrated [41, 50, 51], these require the cavity to have low roundtrip loss or, equivalently, high finesse, in order to make an accurate measurement of the dispersion. It is therefore not practical to make a measurement of the residual dispersion of the enhancement cavity with the nonlinear crystal in place. We therefore devote the remainder of this section to a discussion of efforts to

3.8. Enhancement Bandwidth of the Cavity

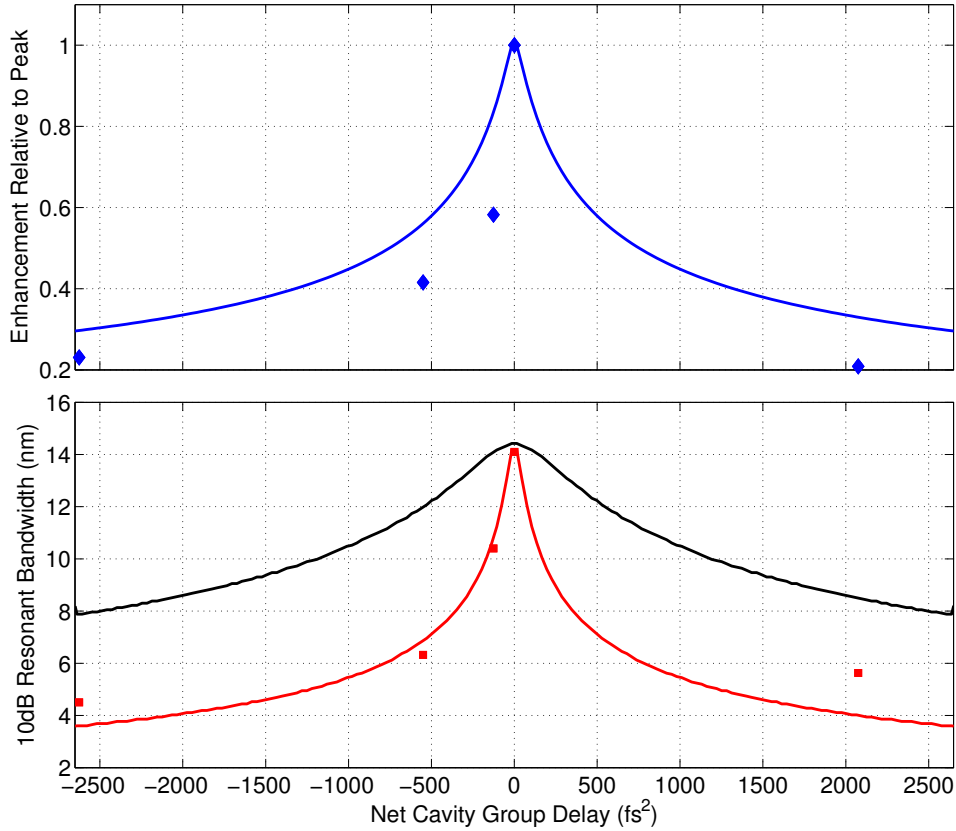


Figure 3.20: Top: Power enhancement of 7 nm full width at half maximum (13.8 nm 10 dB) bandwidth optical field as a function of net group delay dispersion. Blue line: As predicted by resonance map calculations for a passive enhancement cavity having a finesse of 960. Points: Measured enhancements for the cavity configurations of table 3.3. Note that all data is scaled relative to the peak enhancement at zero GDD for each respective data set to account for shortfalls in enhancement due to mode-matching of the seed optical field. Further shortfalls of the measured values with respect to the predicted value at non zero group delays are likely due to the omission of higher order dispersive delays from the simulation. Bottom: Red: Measured and predicted 10 dB resonant spectral bandwidths for a cavity having a finesse of 960. Black: Predicted 10 dB resonant spectral bandwidth for a cavity having a finesse of 100.

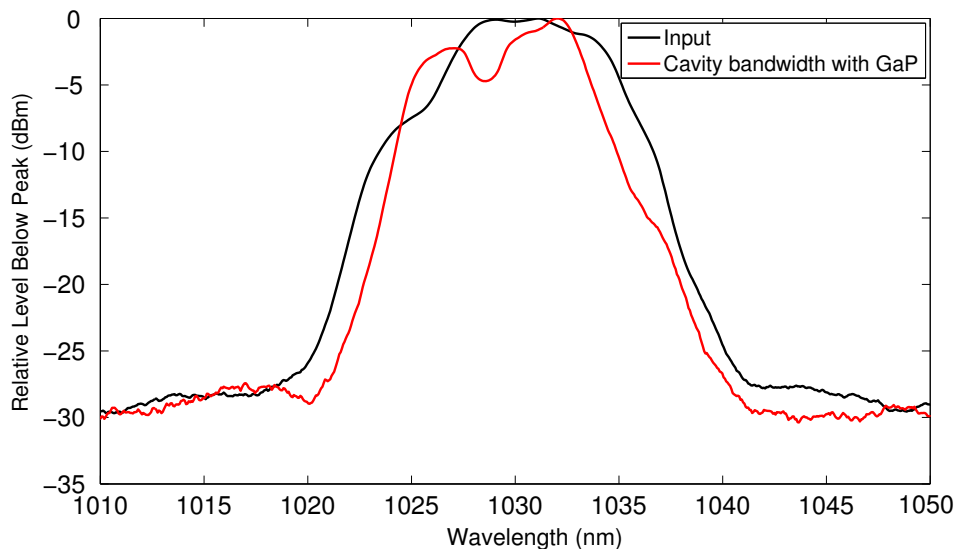


Figure 3.21: Optical spectra supported by the passive enhancement cavity with the gallium phosphide crystal placed at the intracavity focus, compared to the input spectrum. Note that the former is displaced downwards by 10 dB for clarity.

determine the source of the reduced cavity finesse, due to loss mechanisms within the nonlinear crystal.

3.9 Linear Optical Loss of Gallium Phosphide

The previous section demonstrated that, in the absence of the nonlinear crystal, the enhancement cavity has both high finesse and large dispersion. In installing the nonlinear crystal, the finesse of the cavity is significantly reduced, resulting in minimal enhancement of the optical pulses. That it is the finesse of the cavity limiting the build up in this case, and not the dispersion, can be seen in figure 3.21, which shows minimal bandwidth narrowing of the broadband optical pulses used to seed the enhancement cavity.

Having established that, with the nonlinear crystal installed, the dispersion of the cavity is sufficiently minimised such that the cavity is providing

3.9. Linear Optical Loss of Gallium Phosphide

equal enhancement of the entire optical bandwidth and, further, that the cavity exhibits high finesse in the absence of the nonlinear crystal, one's attention turns to the nonlinear crystal itself. Upon locking the enhancement cavity with the gallium phosphide placed at the focus, it was observed that the control loop would continuously increase the voltage at the piezoelectric actuator, thereby effectively reducing the length of the cavity. This behaviour is indicative as to why the gallium phosphide reduced the finesse and enhancement of the cavity. The gallium phosphide exhibits mid-gap, linear absorption of the 1030 nm light inside the cavity, thereby reducing the finesse as per equation 3.11. This absorption leads to thermal expansion of the crystal, which in turn was responsible for the feedback loop applying a continuous ramp to the PZT as the control loop works to keep the cavity on-resonance. In the following section, we determine the voltage ramp applied by the servo to the piezoelectric actuator, and make certain approximations that allow the absorption coefficient, α , of the crystal to be estimated.

As was the case for section 3.8, in order to obtain sufficient optical power in the enhancement cavity such that a leak through one of the cavity high reflectivity mirrors could be measured, the transmission of the input coupler was further increased to 5% (Layertec Part no. 103143). Otherwise, mirrors were as shown in figure 3.6. It is useful to note that, in the absence of any absorption from the nonlinear crystal, the cavity would have a modest finesse of 120. The crystal was placed slightly away from the cavity focus at a point where the beam waist was measured using the technique described in section 3.5.2 as $400 \mu\text{m}$. When the cavity was locked, the power measured at a leak through one of the high reflectivity mirrors was $400 \mu\text{W}$. With the specified mirror reflectivity of 99.97%, found to be in good agreement with a single pass measurement of the transmission, this implies an intracavity power of 1.3W.

A plot of the voltage ramp at a monitor terminal at the servo output is shown in figure 3.22. This monitor port gives $\frac{1}{20}V_{PZT}$, where V_{PZT} is the applied PZT bias. The data shows a clear asymptotic increase in the voltage required to maintain the resonance condition as a function of time, as one expects for the case where the crystal undergoes thermal expansion due to

3.9. Linear Optical Loss of Gallium Phosphide

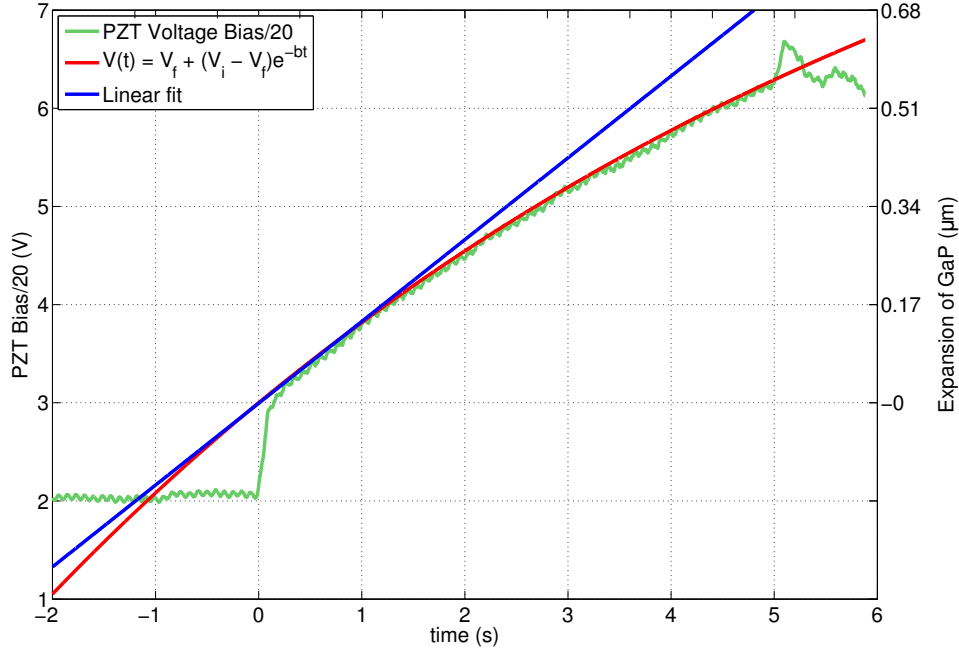


Figure 3.22: Variation of the voltage bias applied to the piezoelectric actuator (PZT) as a function of time following locking of the enhancement cavity. The data is shifted such that the cavity is locked at time = 0 s. An exponential fit is shown with $V_f = 10.5$ V, $V_i = 3$ V, and $b = 0.1155$ s $^{-1}$, as well as a linear fit to the data at early times with $V(t) = 0.8335t + 2.995$ V.

absorption of optical power. The PZT used is model number HPSt 150/6 2-2 from Piezomechanik GmbH. It has a full deflection of $2 \mu\text{m}$ at a maximum 150 V applied bias. Assuming that the length change as a function of applied voltage is linear, using the previously calculated value for the refractive index of gallium phosphide at 1030 nm of 3.11, and using the thermal properties of gallium phosphide listed in table 3.4, one calculates a power absorption of 30 mW, or about 3% given the intracavity power calculated earlier.

We note that this is very much a lower limit on the absorption, as all modes of heat transfer out of the interaction region are neglected. For example, thermal conduction out of the area of the beam waist will mean that an area larger than the beam is heated, which would increase the absorption

3.9. Linear Optical Loss of Gallium Phosphide

Table 3.4: Thermal properties of gallium phosphide, according to [52].

Property	Value at 300K	Units
Coefficient of linear thermal expansion	4.65×10^{-6}	$^{\circ}\text{C}^{-1}$
Specific heat capacity	0.43	$\text{Jg}^{-1}\text{C}^{-1}$
Mass density	4.14	gcm^{-3}

estimate. Radiation of heat to the surroundings will have a similar effect. Still, an absorption of 3% means that, even in the case of perfect locking and zero dispersion, equation 3.13 predicts a maximum amplification factor of 30 times, as opposed to the 700 times if the crystal loss were negligible. The effect of such an additional parasitic loss on the optimal build-up factor is plotted in figure 3.23.

It is clear, therefore, that the optical loss within the gallium phosphide is detrimental to cavity performance. In order to determine if it might be possible to overcome this difficulty, we consider possible mechanisms contributing to this loss.

3.9.1 Loss Mechanisms in Gallium Phosphide

The bandgap of gallium phosphide is 2.26 eV, or 549 nm [33]. One therefore expects minimal linear losses at a wavelength of 1030 nm, or photon energies of 1.21 eV, as this is significantly below the bandgap. We consider first, therefore, the possibility of two photon absorption contributing to the optical loss at these wavelengths. In the presence of such an effect, the intensity of a beam propagating at position z in the medium decreases as

$$\frac{dI(z)}{dz} = -[\alpha + \beta_{TPA}I(z)]I(z), \quad (3.64)$$

where α is the common linear absorption coefficient, and β_{TPA} is the two photon absorption coefficient. In order to determine if the optical loss scaled in the manner expected, the transmission through the crystal was measured in a single-pass configuration using the amplified mode-locked oscillator output described in section 2.4. The power into the crystal was varied using a crossed polariser configuration to avoid possible changes in pulse duration

3.9. Linear Optical Loss of Gallium Phosphide

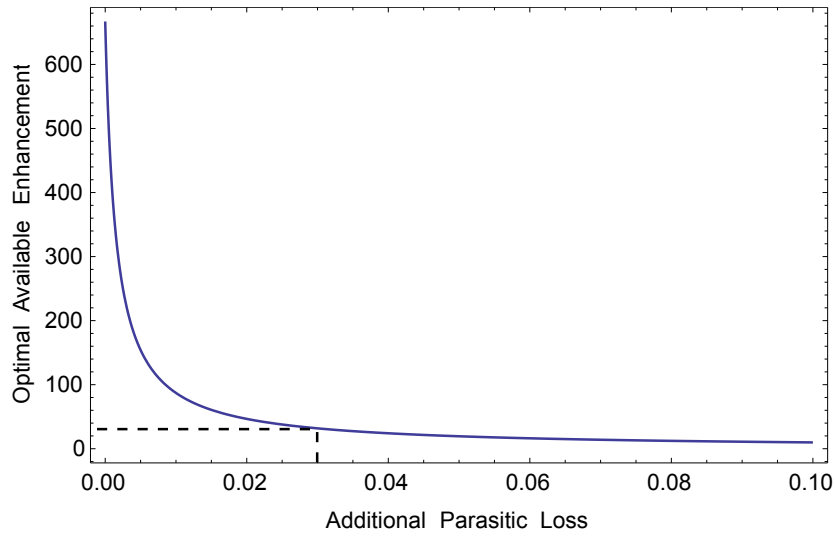


Figure 3.23: Effect of parasitic loss on the optimal enhancement factor that can be obtained from a passive enhancement cavity. The reflectivity of the input coupler is varied such that the cavity is impedance-matched for a given parasitic loss. The reflectivity of the remaining five mirrors is 0.9997. It is useful to note that, in the absence of any parasitic loss, the impedance-matched condition would require an input coupler of transmissivity 0.15%, and this configuration would have a finesse of greater than 2000. Shown in the dotted line is the effect of a 3% parasitic loss on the enhancement factor, as predicted from the thermal expansion data of figure 3.22.

3.9. Linear Optical Loss of Gallium Phosphide

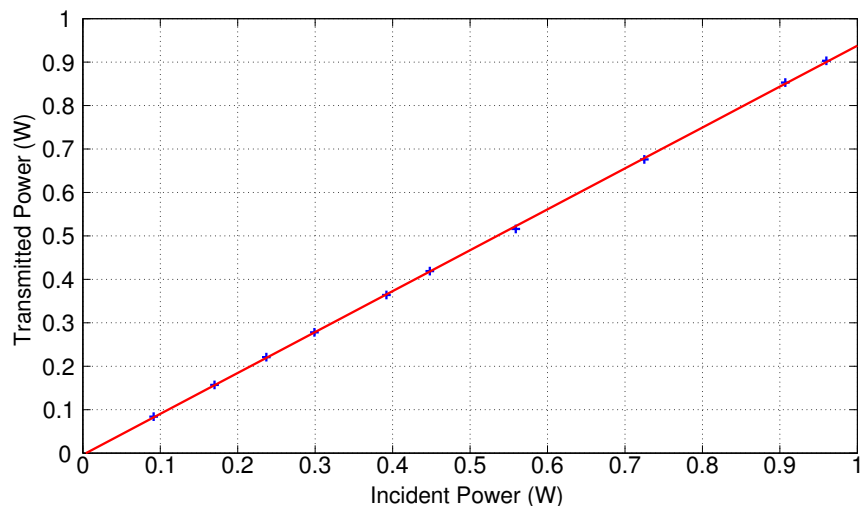


Figure 3.24: Average power transmitted through the gallium phosphide crystal as a function of incident average power. A clear linear trend is evident, with a slope suggesting a 6% linear loss, or $\alpha \simeq 20\text{m}^{-1}$.

that may occur if using the power amplifier pump diode current to vary the optical power. Further, the input field was horizontally polarised so as to minimise reflection losses from the crystal, which was placed at Brewster's angle. That the observed loss does not scale in the manner predicted by equation 3.64 can be seen from figure 3.24.

The $\simeq 6\%$ linear loss shown is greater than that suggested by fitting of the thermal expansion data but, in light of the assumptions made regarding thermal conductivity away from the interaction region, this is not surprising. A perhaps more satisfying conclusion is drawn from a comparison of this loss with the finesse data of section 3.7, where we considered a cavity that, without the nonlinear crystal, had a measured finesse of $\simeq 500$, such that one would expect an enhancement of $\simeq 300$ times. However, experimentally, the observed enhancement with the crystal in the cavity was only seven times, consistent with equation 3.12 for an additional parasitic loss of 7%.

In light of the linear dependence of the observed optical absorption of the nonlinear crystal on input optical power, it is therefore natural to ne-

glect optical losses from two photon absorption. Indeed, we note that the negligible contribution of two photon absorption processes is consistent with other works. See, for example, [53], and comments made in [54].

3.9.2 Characterisation of the Spectral Absorption of Gallium Phosphide

The observed below-bandgap optical absorption in gallium phosphide was further studied by measuring the linear transmission as a function of wavelength. This was achieved by illuminating the sample at normal incidence with narrow (0.9 nm) bandwidth light from a standard grating monochromator. The source used was a 100 W halogen lamp, and the detector was a silicon photodiode, found to have adequate response even at long wavelengths. The measured intensity transmission, I_t was converted to a measure of the absorption coefficient, α as defined in the well known Beer-Lambert law for a propagation length x ,

$$\frac{I_t}{I_{in}} = e^{-\alpha x}. \quad (3.65)$$

The expected reflection coefficient was determined using data from [33], and the transmission normalised to reference spectra. The resulting data is shown in figure 3.25.

Figure 3.25 clearly shows the abrupt change in absorption corresponding to the bandgap of gallium phosphide of 2.26 eV (549 nm). However, of particular interest is that the below bandgap absorption coefficient does not fall immediately to zero, but rather decays slowly in a manner superficially similar to that observed in other indirect bandgap semiconductors at room temperatures, [55] [56]. In these cases, this below bandgap absorption was attributed to the phonon-assisted production of electron-hole pairs. Indeed, a study of the temperature dependence of the intrinsic absorption edge of gallium phosphide [57] attributed this below band-gap absorption at room temperatures to processes involving the absorption of longitudinal and transverse-optical and acoustic phonons. In the data considered here,

3.9. Linear Optical Loss of Gallium Phosphide

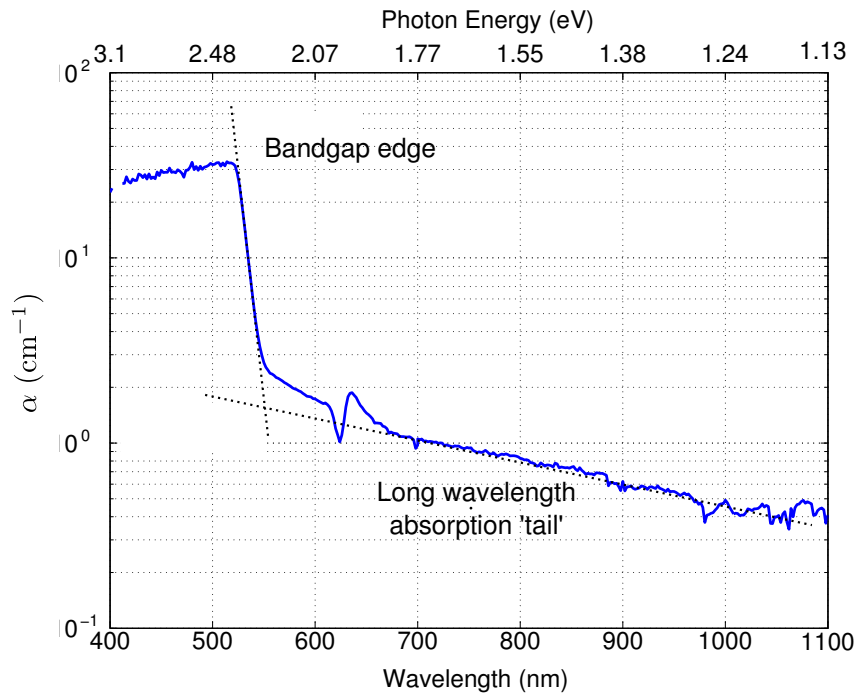


Figure 3.25: Spectral absorption of gallium phosphide, showing the abrupt bandgap edge at $\simeq 550$ nm, and the additional long ‘tail’ for long wavelengths out to 1100 nm, where the response of the silicon detector limits the measurement range.

this tail gives rise to an absorption coefficient of $\simeq 40\text{cm}^{-1}$ at 1030 nm for which, for the 2.1 mm propagation length in the enhancement cavity, one would expect $\simeq 8\%$ single pass loss.

Scattering from lattice defects may also be a contributing factor to this large absorption at wavelengths below bandgaps. Indeed, we note that the crystals had a specified etch pit density (EPD, commonly used as an indicator of the density of lattice defects) of $<(0.5-1) \times 10^5 \text{ cm}^{-2}$. Whilst this is typical of commonly available gallium phosphide substrates, it is a relatively large value when compared to other semiconductors (for example, gallium arsenide crystals are commonly available with an EPD of $\simeq 1 \times 10^4 \text{ cm}^{-1}$ [58]). Several authors have reported that higher densities of lattice defects give rise to increased broadening of the bandgap edge and, in particular, increased below bandgap absorption [59]. Whilst it is beyond the scope of the current work to study such effects in detail, it is, perhaps, possible that such effects may be mitigated should manufacturing processes improve to the point that gallium phosphide crystals with fewer lattice defects become available in the future.

3.10 Conclusions on the use of a Passive Enhancement Cavity for High Efficiency Generation of Terahertz Radiation

It is clear that the enhancements predicted by the modelling work of section 3.3 cannot be achieved unless the observed optical absorption of gallium phosphide can be overcome. As discussed above, it is possible that small reductions in the linear loss could be achieved by increasing the quality of the gallium phosphide substrates, such that scattering due to lattice defects are decreased. However, the data in figure 3.25 would suggest that the dominant loss mechanisms are phonon-assisted processes within the gallium phosphide lattice itself. This being the case, significant reductions in the linear optical loss can therefore only be realised in two ways. Firstly, by reducing the optical path length in the nonlinear crystal, such that the total

absorption is reduced, or changing the crystal material entirely.

In considering the possibility of alternative nonlinear materials, it is worth noting that Theuer et al. [60] were able to increase the efficiency of terahertz generation using a similar cavity configuration. In contrast to the work presented here, the authors of [60] generated terahertz radiation from Cherenkov-type optical rectification within a lithium niobate crystal. The crystal was placed within a passive enhancement cavity seeded with the 800 nm output of a titanium-doped sapphire glass oscillator. These authors achieved an 8-7 times enhancement in the optical power within the cavity, which in turn produced a 5 times enhancement in the terahertz field observed over that measured without the aid of the cavity. The enhancement of the cavity was again found to be limited by the $\simeq 3\%$ linear loss of the crystal, rising to $\simeq 8\%$ for higher intracavity optical powers, owing to increased two-photon absorption in lithium niobate. The lower linear losses of lithium niobate therefore make this method perhaps more appealing for enhancement cavity-based terahertz generation. However, the need to drive the crystal at 800 nm, due to phase-matching restrictions, necessitates seeding the cavity with titanium-doped sapphire oscillators. Ytterbium-doped fibre laser systems are inherently more power-scalable with high repetition rates, whilst maintaining the frequency comb structure. Further, the conical output geometry of the terahertz field in the Cherenkov-type optical rectification leads to complications in shaping the resulting terahertz beam. Other authors have reported successes using certain organic crystals for terahertz generation via optical rectification [61], [62] at optical wavelengths of 800 nm and 1550 nm respectively. Whilst these crystals can offer increased performance in terms of the effective nonlinear optical coefficient, to date no efforts have been made to reduce the linear optical loss at their respective pump wavelengths. As a result, the absorption coefficient for these crystals is typically greater than that measured for gallium phosphide at 1030 nm in section 3.9. Indeed, Brunner et al. quote an absorption coefficient of not more than 3 cm^{-1} for 2-cyclooctylamino-5-nitropyridine at 800 nm [61]. Continued research in this area may, however yield a crystal with low linear optical losses such that intracavity generation becomes more attractive.

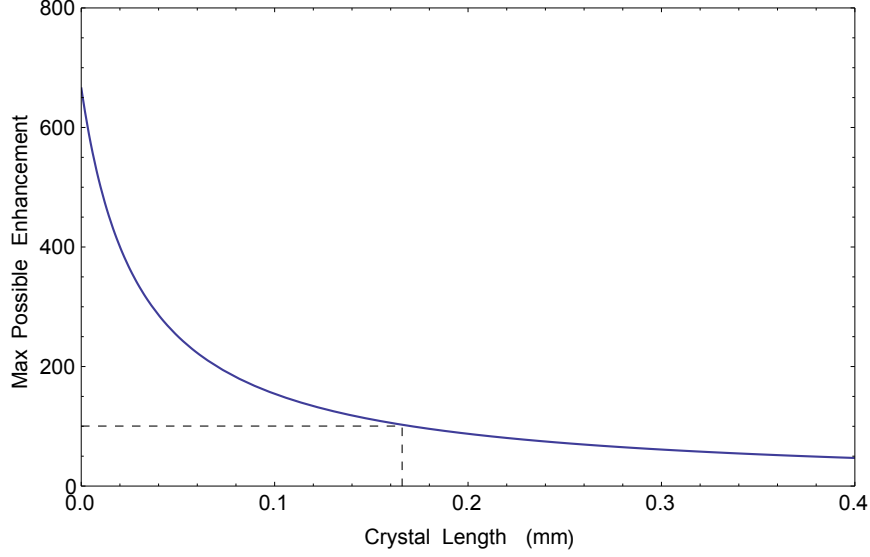


Figure 3.26: Maximum possible enhancement factor provided by an impedance-matched enhancement cavity containing a nonlinear crystal having absorption coefficient, $\alpha = 0.5 \text{ cm}^{-1}$ and varying length. The mirror reflectivity, $R = 0.9997^5$. The cavity is assumed to be perfectly tuned to resonance for all incident wavelengths, and the input Gaussian beam is assumed to perfectly-matched to that of the cavity, thereby providing an upper limit on the enhancement that can be obtained for given crystal length.

To illustrate the possibility of reducing the optical path length in the nonlinear crystal within the cavity, we rewrite equation 3.12 to include the crystal loss as

$$\frac{I_{max}}{I_{in}} = \frac{1 - R_{ic}}{(1 - \sqrt{RR_{ic}e^{-\alpha l}})^2} \quad (3.66)$$

where l is the optical path length in the nonlinear crystal. In this case, the impedance-matching condition, equation 3.13 becomes

$$R_{ic} = Re^{-\alpha l} \quad (3.67)$$

We plot in figure 3.26 the maximum possible enhancement predicted by equation 3.66 for varying crystal lengths, assuming a crystal absorption co-

3.10. Conclusions of Enhancement Cavity Work

efficient $\alpha = 0.5\text{cm}^{-1}$. It is seen that, in order for the cavity to provide a relatively modest enhancement factor of 100, the maximum crystal thickness is less than $200\ \mu\text{m}$. Equation 3.27 suggests that, for given optical power incident on the crystal, the terahertz power produced is a factor of 100 down on that expected from the 2 mm crystal used here. In light of emerging technology in the field of high power femtosecond combs [63], [64], it would therefore seem that driving a longer crystal with such a high-power comb in a single-pass configuration offers greater potential for the generation of high-power terahertz frequency combs.

Chapter 4

A Single Comb Terahertz Time-domain Spectrometer with Detection Using Conventional Electro-optic Sampling

4.1 Introduction

As discussed previously, there is significant interest in the use of terahertz radiation to characterise various molecules due to the fact that many rotational and vibrational molecular transitions occur in this wavelength range. The common technique to do this is known as terahertz time domain spectroscopy, (THz-TDS). In this technique, the terahertz field is used to interrogate the sample, whilst a portion of the optical beam used to generate the terahertz radiation is used to probe the transmitted terahertz pulse, most commonly using an optically gated antenna [65], or via electro-optic sampling (EOS) within a nonlinear crystal [34]. The delay between the two pulses is varied using a mechanical delay of one pulse, and the resulting trace of the terahertz electric field is recorded as a function of the delay. Frequency analysis is performed by taking a Fourier transform in a manner identical to conventional Fourier transform spectroscopy (see for example, [65]). As conventional THz-TDS uses a sample of the driving optical field to sample the terahertz field, we refer to this as single-comb THz-TDS (SC THz-TDS)

for clarity in later discussions where we use a separate laser oscillator to perform the sampling step.

We have built such a SC THz-TDS system, along the same design as [34], using free-space EOS to measure the terahertz field. In light of the results of Chapter 3, we use a gallium phosphide waveguide emitter of the type demonstrated in [66], giving an increased interaction length of the driving optical field and the generated terahertz radiation in the nonlinear crystal, so as to increase the power of the terahertz field for the available optical pump power. The following chapter discusses our experimental arrangement and results.

4.2 Experimental Arrangement

The experimental apparatus was arranged as in figure 4.1, following a design similar to [21]. In this conventional THz-TDS arrangement, both the ‘pump’ pulse used to generate the terahertz radiation in the nonlinear crystal, and the sampling probe pulse are derived from the same laser output. In our case, the $\simeq 3\text{W}$ output from the amplified fibre laser system described in section 2.4, and illustrated in figure 2.10a). The optical output pulses were compressed to 240 fs using the grating compressor arrangement described in section 2.4.2. We use a 10% beam sampling optic to provide up to $\simeq 300\text{ mW}$ in the probe beam used to sample the terahertz field. The high-power pump field is then sent through a mechanical delay stage to vary the delay between the pump pulse and the sampling probe pulse used to detect the terahertz field. This configuration gave up to 2.5W of optical power incident on the nonlinear crystal used for terahertz generation. At the laser output, the polarisation state of the light is optimised to that giving maximum diffraction efficiency for the grating compressor. A subsequent half-wave plate was used in both the pump arm and the probe arm to give the optimum linear polarisation orientation for both terahertz generation (as discussed in section 2.2) and EOS within the detection crystal.

Recall equation 2.29, where we saw that, under conditions of perfect phase-matching, the terahertz power generated through the optical rectifi-

4.2. Experimental Arrangement

cation process increases with interaction length in the nonlinear crystal. We therefore seek to maximise this interaction length by increasing the crystal thickness (note that, in the single-pass optical rectification scheme used here, we are not limited by the resulting increased dispersion and linear absorption of the optical field). In order to increase the interaction length of the optical rectification process, it is necessary to ensure that the driving optical beam remains collimated throughout the interaction volume. To understand this, we write the scaling of the radiated terahertz power, P_{THz} , as

$$P_{THz} = \eta_{dif} \mathcal{A} I_{THz}, \quad (4.1)$$

where \mathcal{A} is the THz-emitting area within the crystal, and η_{dif} is a dimensionless coefficient that accounts for diffraction due to the finite source area. The intensity of the driving optical field scales as

$$I_{opt} = \frac{P_{opt}}{\mathcal{A}} \propto \frac{P_{opt}}{r^2}. \quad (4.2)$$

where r is the radius of the optical beam. For large optical spot sizes, $r > \lambda_{THz}$, $\eta_{dif} \simeq 1$, and essentially all of the terahertz field is able to propagate into the far-field, resulting in the power of the terahertz field scaling as

$$P_{THz} \propto \frac{P_{opt}^2}{r^2}. \quad (4.3)$$

If $r < \lambda_{THz}$, however, diffractive effects reduce η_{dif} , and only part of the terahertz field will radiate into the far-field. Bethe et al. [67] showed that, for a general field of wavelength λ , $\eta_{dif} \propto r^4$ for $r \ll \lambda$. In the case of the terahertz field of wavelength λ_{THz} then,

$$P_{THz} \propto P_{opt}^2 r^2. \quad (4.4)$$

Equations 4.3, and 4.4 show that, for fixed optical pump power, the scaling of the emitted terahertz power scales as $\frac{1}{r^2}$ for large optical spot sizes, and as r^2 for small optical spot sizes. Xu et al. [68] showed experimentally that the maximum terahertz power is produced for an optical spot size roughly equal

4.2. Experimental Arrangement

in radius to the wavelength of the terahertz field. For a terahertz frequency of 1 THz, one obtains an optical beam radius of $300 \mu\text{m}$. In bulk crystals, such a spot size leads to strong divergence of the terahertz field, reducing the spatial overlap of the optical and terahertz fields. In order to overcome this, we use a gallium phosphide waveguide emitter of the type developed in [66]. Due to the large refractive index contrast, the waveguide emitter confines the terahertz field such that the spatial overlap between the two beams is maintained along the 6 mm length of the waveguide. The faces of the crystal were 0.4×0.6 mm. The optical spot diameter was $190 \mu\text{m}$, as per [66], and the Rayleigh range was determined to be in excess of 8 mm using the technique described in section 3.5.2, such that the waveguide structure guides only the terahertz beam. The output optical and terahertz beams then exit the crystal co-linearly. A schematic of this arrangement is shown in figure 4.2. The diverging terahertz field is collimated by a 1" focal length, aluminium coated off-axis parabolic mirror, and refocussed into the nonlinear detection crystal using a second, identical parabolic mirror. A piece of high-density PTFE was placed between the two mirrors to block the residual optical pump beam, whilst transmitting the terahertz radiation [69].

Two different detection crystals were used for this experiment. A 1 mm thick piece of $\langle 110 \rangle$ zinc telluride, and the 2 mm thick piece of gallium phosphide described in section 3.3. The probe pulse was coupled into the crystal using a nitro-cellulose pellicle beam splitter, such that the optical probe pulse was co-linear with the focused terahertz beam, and normally incident upon the nonlinear detection crystal. The 45% reflectivity of this pellicle splitter produced up to 200 mW of average power in the optical probe pulse incident on the nonlinear detection crystal. It was found that, despite the inferior phase-matching at the optical wavelength of 1030 nm, the zinc telluride crystal gave the better sensitivity when compared to the gallium phosphide crystal, on account of the larger nonlinear optical coefficient. In both the single comb case pictured in figure 4.1 and in the dual-comb case to be discussed later, two different detection schemes were utilised, both being based in EOS. The first of these employing a balanced detector and conventional ellipsometry, and the second, using a single channel detector.

4.2. Experimental Arrangement

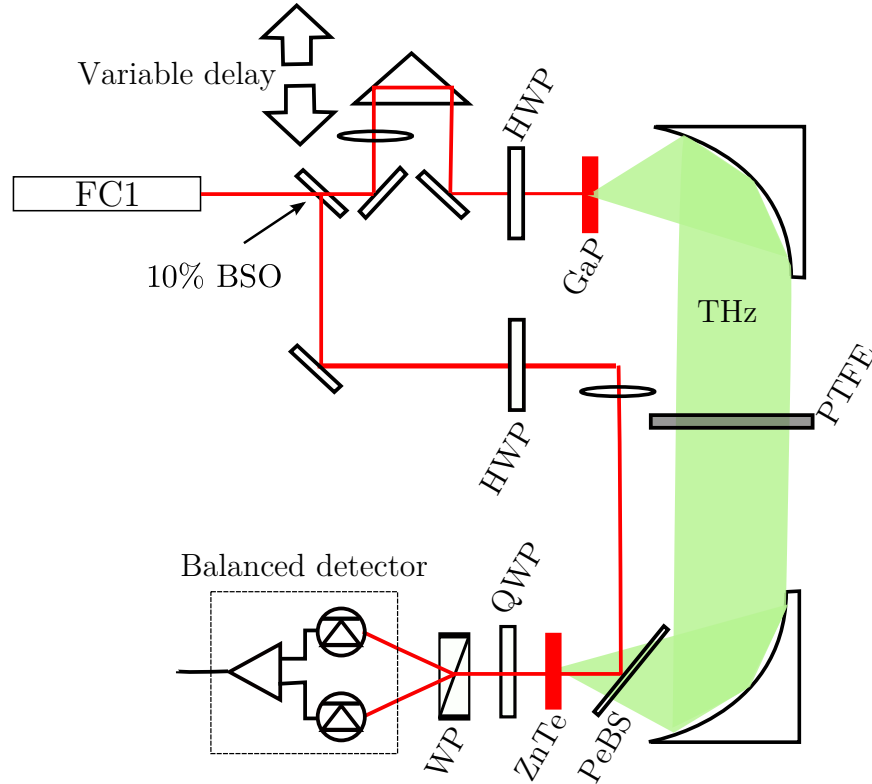


Figure 4.1: Experimental arrangement for the single-comb terahertz time-domain spectrometer used to characterise the terahertz output prior to demonstrating the dual-comb spectrometer of section 5. The apparatus uses a single optical frequency comb (FC1) from which 10% of the optical power is picked off using a beam splitting optic (BSO) to form the probe beam. The remaining optical power is used to drive the nonlinear crystal to generate the terahertz radiation. In this arrangement, a variable delay line in the pump arm allows the temporal overlap of the terahertz and optical probe pulses in the electro-optic detection crystal to be varied. The probe pulse is coupled into the detection crystal using a pellicle beam splitter (PeBS). Waveplates are used to optimise the polarisation states of the various beams so as to utilise the largest nonlinear coefficients, and a piece of polytetrafluoroethylene (PTFE) is used to block the residual optical beam after the generating crystal.

4.3. Detection of the Terahertz Frequency Comb via Electro-optic Sampling

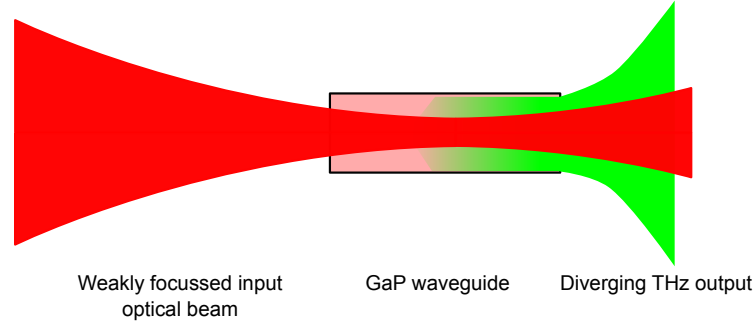


Figure 4.2: Beam propagation in the gallium phosphide waveguide structure. The optical beam is weakly focussed such that the Rayleigh range greatly exceeds the length of the crystal. In contrast, the terahertz beam diverges strongly by virtue of its longer wavelength. This is counteracted in the crystal due to the high refractive index contrast. The beam at the output face of the crystal diverges strongly, and is collimated using a 90° off-axis parabolic mirror.

A discussion of the operation and merits of each of these detection schemes follows.

4.3 Detection of the Terahertz Frequency Comb via Electro-optic Sampling

4.3.1 The Linear Electro-optic Effect

In order to detect the terahertz field, we use electro-optic sampling [70]. In this technique, the terahertz field is used to write a polarisation rotation onto an optical probe field via the linear electro-optic effect in a nonlinear detection crystal. For this work, we use two configurations to perform this task. The first of these splits the probe beam into orthogonal linear polarisation states and measures a change in the relative intensities of each state due to overlap of the probe and terahertz fields in the detection crys-

4.3. Detection of the Terahertz Frequency Comb via Electro-optic Sampling

tal. The second scheme uses a crossed polariser and single detector placed behind the detection crystal. The polariser is set such that a null signal is observed for zero overlap of the terahertz and probe fields. When the fields overlap, the polarisation of the probe is altered such that some small signal is observed. For both detection schemes lock-in detection is employed in the single comb spectrometer case so as to increase the signal to noise ratio. There follows a detailed analysis of the electro-optic detection process, followed by a discussion of the merits of each of the two detection schemes.

The terahertz and sampling optical probe fields are incident on the detection crystal in a collinear geometry. Wave-retarding plates are used to rotate the polarisation of the optical field transmitted by the crystal in such a way so as to give a null signal in the absence of the terahertz field. The effect of the terahertz field is to induce birefringence in the crystal according to the linear electro-optic effect such that a non-zero signal is detected in each of the detection schemes. In the absence of the terahertz field, the refractive index ellipsoid of the sampling crystal, that is, the surface over which the energy density, $w_e = \frac{1}{2} \vec{E} \cdot \vec{D}$ is constant, is defined by the relation

$$\frac{u_1^2}{\varepsilon_{11}} + \frac{u_2^2}{\varepsilon_{22}} + \frac{u_3^2}{\varepsilon_{33}} = 1. \quad (4.5)$$

Here, we define the dimensionless vector, \vec{u} according to the electric displacement vector, \vec{D} by

$$\vec{u} = \frac{\vec{D}}{\sqrt{2\varepsilon_0 w_e}}, \quad (4.6)$$

and ε_{ij} is the dielectric permeability tensor, which, when expressed in the principal basis of the crystal, is diagonal, hence $\varepsilon_{ij} = 0$ for $i \neq j$. To explain the change in this index ellipsoid in the presence of the terahertz field, we start by considering ε_{ij} , and assume that it can be written in the form of a power series in the strengths of the components, E_k , of the applied field as:

$$\frac{1}{\varepsilon_{ij}} = \frac{1}{\varepsilon_{ij}^{(0)}} + \sum_k r_{ijk} E_k + \sum_{kl} s_{ijkl} E_k E_l + \dots \quad (4.7)$$

where r_{ijk} is the linear electrooptic tensor, and s_{ijkl} describes the quadratic

4.3. Detection of the Terahertz Frequency Comb via Electro-optic Sampling

electrooptic effect. Typically, $s_{ijkl} \ll r_{ijk}$ and we consider only the linear effect here. Since ε_{ij} is real and symmetric, it is common to use the contracted index notation r_{hk} where

$$h = \begin{cases} 1 & \text{for } ij = 11, \\ 2 & \text{for } ij = 22, \\ 3 & \text{for } ij = 33, \\ 4 & \text{for } ij = 23 \text{ or } 32, \\ 5 & \text{for } ij = 13 \text{ or } 31, \\ 6 & \text{for } ij = 12 \text{ or } 21. \end{cases} \quad (4.8)$$

Relating the dielectric permeability tensor to the refractive index via

$$\frac{1}{n_h^2} = \frac{1}{\varepsilon_{ij}}, \quad (4.9)$$

we see that the deformation of the refractive index ellipsoid, that is, the lowest order changes to the optical constants $\left(\frac{1}{n^2}\right)_i$ are described by the relation

$$\Delta\left(\frac{1}{n^2}\right)_i = \sum_{j=1}^3 r_{ij} E_j. \quad (4.10)$$

For zincblende crystals of point group $\bar{4}3m$ such as gallium phosphide and zinc telluride, the electrooptic coefficients r_{ij} vanish except $r_{41} = r_{52} = r_{63}$ which, for zinc telluride has a value 4.04pm/V [71], and for gallium phosphide 0.97ppm/V [72]. The equality of the non-zero coefficients makes the crystal uniaxial, and hence, making the common definitions of the ordinary and extraordinary refractive indices, $n_o^2 = \varepsilon_{11} = \varepsilon_{22}$ and $n_e^2 = \varepsilon_{33}$, the index ellipsoid is described as

$$\frac{u_1^2}{n_o^2} + \frac{u_2^2}{n_o^2} + \frac{u_3^2}{n_e^2} = 1. \quad (4.11)$$

Under the influence of an applied electric field, $\vec{E}_a = E_{aX}\hat{i} + E_{aY}\hat{j} + E_{aZ}\hat{k}$,

4.3. Detection of the Terahertz Frequency Comb via Electro-optic Sampling

this ellipsoid is modified according to equation 4.10 such that

$$\frac{u_1^2}{n_o^2} + \frac{u_2^2}{n_o^2} + \frac{u_3^2}{n_e^2} + 2r_{41}(E_{a1}u_2u_3 + E_{a2}u_3u_1 + E_{a3}u_1u_2) = 1. \quad (4.12)$$

Both zinc telluride and gallium phosphide are cubic zincblende lattices and, owing to the high degree of crystal symmetry, are optically isotropic (show zero birefringence) for zero applied electric fields. In this case, we can therefore write $n_e = n_o$. Using the coordinate system definitions of figure 4.3 for the [110] cut crystals used here, we consider the terahertz field to be incident along the $-\hat{x}'$, or $[-1 -1 0]$ direction, linearly polarised at an angle α to the \hat{y}' direction. Alternatively, in the coordinate basis of the crystal lattice,

$$\vec{E}_a = \frac{E_a}{\sqrt{2}} \begin{pmatrix} -\cos \alpha \\ \cos \alpha \\ \sqrt{2} \sin \alpha \end{pmatrix}. \quad (4.13)$$

Equation 4.12 can then be written in matrix form as

$$\vec{u} \cdot \hat{\eta}(\vec{E}_a) \cdot \vec{u}, \quad (4.14)$$

where $\hat{\eta}(\vec{E}_a)$ is the field-dependent impermeability tensor

$$\hat{\eta}(\vec{E}_a) = \frac{1}{n_o^2} \begin{pmatrix} 1 & 0 & 0 \\ 0 & 1 & 0 \\ 0 & 0 & 1 \end{pmatrix} + r_{41} \frac{E_a}{\sqrt{2}} \begin{pmatrix} 0 & \sqrt{2} \sin \alpha & \cos \alpha \\ \sqrt{2} \sin \alpha & 0 & -\cos \alpha \\ \cos \alpha & -\cos \alpha & 0 \end{pmatrix}. \quad (4.15)$$

In order to find the principal axis of the crystal under the influence of this electric field, and the relevant refractive indices, we find the eigenvalues of the impermeability tensor, $\hat{\eta}(\vec{E}_a)$:

$$\lambda_{1,2} = \frac{1}{n_o^2} - \frac{r_{41}E_a}{2}(\sin \alpha \pm \sqrt{1 + 3 \cos^2 \alpha}), \quad \lambda_3 = \frac{1}{n_o^2} + r_{41}E_a \sin \alpha, \quad (4.16)$$

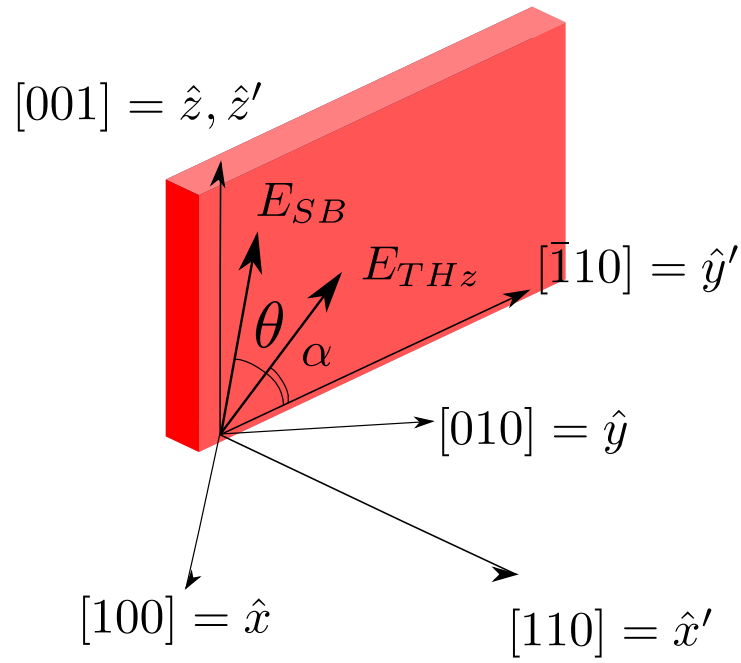


Figure 4.3: Crystal geometry for the electro-optic detection scheme. Both the terahertz and optical probe field are assumed to be incident along the $-x' = [\bar{1}\bar{1}0]$ direction, with the terahertz field polarised at an angle α with respect to the $y' = [\bar{1}10]$ direction.

4.3. Detection of the Terahertz Frequency Comb via Electro-optic Sampling

and the normalised eigenvectors

$$\begin{aligned}
 \mathbf{U}_1 &= \frac{1}{2} \sqrt{1 + \frac{\sin \alpha}{\sqrt{1 + 3 \cos^2 \alpha}}} \begin{pmatrix} -1 \\ 1 \\ \frac{2\sqrt{2} \cos \alpha}{\sqrt{1 + 3 \cos^2 \alpha} - \sin \alpha} \end{pmatrix} \\
 \mathbf{U}_2 &= \frac{1}{2} \sqrt{1 - \frac{\sin \alpha}{\sqrt{1 + 3 \cos^2 \alpha}}} \begin{pmatrix} 1 \\ -1 \\ \frac{2\sqrt{2} \cos \alpha}{\sqrt{1 + 3 \cos^2 \alpha} - \sin \alpha} \end{pmatrix} \\
 \mathbf{U}_3 &= \frac{1}{\sqrt{2}} \begin{pmatrix} -1 \\ -1 \\ 0 \end{pmatrix}.
 \end{aligned} \tag{4.17}$$

Under the effect of the applied electric field, the crystal principal axes are parallel to these eigenvectors, and the refractive indices are given by

$$n_i = \frac{1}{\lambda_i}, \tag{4.18}$$

which yields, to good approximation,

$$\begin{aligned}
 n_1 &= n_o + \frac{n_o^3 r_{41} E_a}{4} (\sin \alpha + \sqrt{1 + 3 \cos^2 \alpha}) \\
 n_2 &= n_o + \frac{n_o^3 r_{41} E_a}{4} (\sin \alpha - \sqrt{1 + 3 \cos^2 \alpha}) \\
 n_3 &= n_o - \frac{n_o^3 r_{41} E_a}{2} \sin \alpha.
 \end{aligned} \tag{4.19}$$

From equation 4.17, the vector \mathbf{U}_3 is perpendicular to the (110) crystal plane, or parallel to the direction along which the electric field is incident. The refractive index ellipsoid of the crystal can therefore be projected into the (110) plane, as shown in figure 4.4. The orientation of this ellipsoid is described by the angle ψ that the vector \mathbf{U}_1 makes with the [-110] crystal

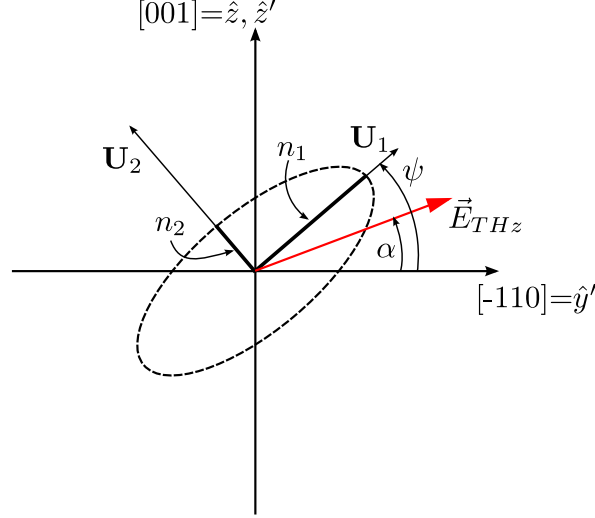


Figure 4.4: Deformation of the two-dimensional refractive index ellipsoid in the (110) crystal plane, upon which the applied dc field, E_a is incident with polarisation angle α with respect to the $[-110]$ crystal axis. The end result is a deformation of the index ellipsoid such that the fast and slow axis are along \mathbf{U}_1 and \mathbf{U}_2 respectively.

axis, which can be shown to be

$$\cos 2\psi = \frac{\sin \alpha}{\sqrt{1 + 3 \cos^2 \alpha}}. \quad (4.20)$$

The frequency of the optical probe pulse is far greater than that of the terahertz field. On the timescale of the probe field, the terahertz field therefore represents just such a dc electric field as E_a . If both the terahertz and optical probe fields are incident along the $[110]$ direction, the deformation of the index ellipsoid is such that the components of the optical probe along the principal axes $\vec{\mathbf{U}}_1$ and $\vec{\mathbf{U}}_2$ receive a relative phase shift of

$$\Gamma(\alpha) = \frac{\omega d}{c}(n_1 - n_2) = \frac{\omega d}{2c} n_o^3 r_{41} |E_{THz}| \sqrt{1 + 3 \cos^2 \alpha}, \quad (4.21)$$

4.3. Detection of the Terahertz Frequency Comb via Electro-optic Sampling

where d is the thickness of the crystal, ω is the angular frequency of the optical probe field, and $|E_{THz}|$ is the magnitude of the terahertz electric field. The polarisation of the optical probe beam is therefore altered in a manner that depends both on the polarisation and the magnitude of the terahertz field. This is exactly analogous to the linear Pockels effect.

The crystals used here are cut with one edge parallel to the $\hat{y}' = [\bar{1}10]$ direction, as shown in figure 4.3. Both the terahertz and optical probe beams are incident along the $\hat{x}' = [110]$ direction. In order to determine the effect of this relative phase shift on the orthogonal polarisation states of an arbitrary, but linearly polarised probe beam, we resort to the method of Jones calculus [73]. The optical probe field has complex amplitude E_{LO} with horizontal and vertical components described in matrix form by

$$\vec{E}_h = E_{LO} \begin{pmatrix} 1 \\ 0 \end{pmatrix}, \vec{E}_v = E_{LO} \begin{pmatrix} 0 \\ 1 \end{pmatrix}. \quad (4.22)$$

Upon propagating through the crystal, these components of the sampling optical probe field undergo a phase change described in the crystal principal axes system by the matrix

$$\mathbf{XT}(\alpha) = \begin{pmatrix} \exp(-in_1(\alpha)\omega d/c) & 0 \\ 0 & \exp(-in_2(\alpha)\omega d/c) \end{pmatrix}, \quad (4.23)$$

which we can rewrite in terms of the relative phase change, $\Gamma(\alpha)$ as

$$\mathbf{XT}(\alpha) = \exp(-i\phi) \begin{pmatrix} \exp(-i\Gamma(\alpha)/2) & 0 \\ 0 & \exp(+i\Gamma(\alpha)/2) \end{pmatrix}. \quad (4.24)$$

Putting together these matrix components, the effect of the nonlinear crystal on a horizontally polarised probe beam is therefore

$$E_{LO} \cdot \mathbf{R}(-\psi(\alpha)) \cdot \mathbf{XT}(\alpha) \cdot \mathbf{R}(\psi(\alpha)) \cdot \begin{pmatrix} 1 \\ 0 \end{pmatrix}. \quad (4.25)$$

where $\mathbf{R}(\psi(\alpha))$ is the matrix corresponding to the rotation of the coordinate

4.3. Detection of the Terahertz Frequency Comb via Electro-optic Sampling

system by an angle $\psi(\alpha)$ from the lab to that of the crystal principal axis.

4.3.2 Comparison of Detection Schemes

Up until this point, the analysis of the polarisation rotation of the optical probe beam has been independent of the detection method employed. We now consider the effect of analysing the beam using a single channel detector and crossed polariser configuration, versus the dual channel, balanced detector method illustrated in figure 4.1. In the first case, we use a half-wave plate to rotate the polarisation of the transmitted probe beam to be perpendicular to that transmitted by the polariser. The field of equation 4.25 after transmission through the polariser is then given by

$$E_{LO} \cdot \begin{pmatrix} 0 & 0 \\ 0 & 1 \end{pmatrix} \cdot \mathbf{R}(-\psi(\alpha)) \cdot \mathbf{XT}(\alpha) \cdot \mathbf{R}(\psi(\alpha)) \cdot \begin{pmatrix} 1 \\ 0 \end{pmatrix}. \quad (4.26)$$

Substituting in equation 4.24 and taking the square of the transmitted vertical component gives the intensity measured at a photodetector positioned behind this polariser:

$$S_{1Ch}(\alpha) = E_{LO}^2 \sin^2(2\psi(\alpha)) \sin^2\left(\frac{\Gamma(\alpha)}{2}\right). \quad (4.27)$$

Alternatively, the nominally horizontally polarised (in the absence of the crystal birefringence induced by the terahertz field) probe beam is passed through a quarter-wave plate at 45° to the horizontal, giving circular polarisation. This is then analysed using a polarising beam splitter to obtain orthogonal polarisation states, and a pair of photodiodes wired in a balanced configuration. The field transmitted by the crystal and quarter-wave plate arrangement is now obtained by multiplying equation 4.25 by

$$\mathbf{R}\left(\frac{-\pi}{4}\right) \cdot \mathbf{QWP} \cdot \mathbf{R}\left(\frac{-\pi}{4}\right) \quad (4.28)$$

where \mathbf{QWP} is the commonly known Jones matrix for a quarter-wave plate

4.3. Detection of the Terahertz Frequency Comb via Electro-optic Sampling

$$\begin{pmatrix} \exp(-i\pi/4) & 0 \\ 0 & \exp(i\pi/4) \end{pmatrix}. \quad (4.29)$$

One obtains, for the field incident on the polarising beam splitter,

$$\mathbf{R}\left(\frac{-\pi}{4}\right) \cdot \mathbf{QWP} \cdot \mathbf{R}\left(\frac{-\pi}{4}\right) \cdot E_{LO} \cdot \mathbf{R}(-\psi(\alpha)) \cdot \mathbf{XT}(\alpha) \cdot \mathbf{R}(-\psi(\alpha)) \cdot \begin{pmatrix} 1 \\ 0 \end{pmatrix}. \quad (4.30)$$

In the absence of any applied terahertz field $\Gamma(\alpha) = 0$, as predicted by equation 4.21, and $\mathbf{XT}(\alpha)$ is equal to the 2×2 identity matrix. In this case, equation 4.30 predicts equal magnitudes in both orthogonal polarisation states. Analysing the field of equation 4.30 using a polarisation beam splitter to detect each polarisation state on a balanced detector therefore produces a null signal. If the terahertz and optical fields overlap in the crystal, however, the transmitted optical polarisation is elliptically polarised. In particular, in the case where $\alpha = 0$ the relative phase delay between the polarisation states, $\Gamma(\alpha)$ is a maximum, and $\psi = \frac{\pi}{4}$. In this case, equation 4.30 gives, for the components of the detected field

$$\mathbf{E}_{det} = \frac{E_{LO}}{\sqrt{2}} \begin{pmatrix} \sin(\Gamma/2) - \cos(\Gamma/2) \\ i(\sin(\Gamma/2) + \cos(\Gamma/2)) \end{pmatrix}. \quad (4.31)$$

The output of the balanced detector then gives the difference in the intensities of each component

$$\begin{aligned} S_{bal} &= |E_{det,h}|^2 - |E_{det,v}|^2 \\ &= \frac{|E_{LO}|^2}{2} \left(\cos^2\left(\frac{\Gamma}{2}\right) + \sin^2\left(\frac{\Gamma}{2}\right) - 2 \cos\left(\frac{\Gamma}{2}\right) \sin\left(\frac{\Gamma}{2}\right) - \cos^2\left(\frac{\Gamma}{2}\right) \right. \\ &\quad \left. - \sin^2\left(\frac{\Gamma}{2}\right) - 2 \cos\left(\frac{\Gamma}{2}\right) \sin\left(\frac{\Gamma}{2}\right) \right) \\ &= \frac{|E_{LO}|^2}{2} \left(4 \cos\left(\frac{\Gamma}{2}\right) \sin\left(\frac{\Gamma}{2}\right) \right) \\ &= |E_{LO}|^2 \sin(\Gamma) \end{aligned} \quad (4.32)$$

4.3. Detection of the Terahertz Frequency Comb via Electro-optic Sampling

In the typical case of weak terahertz field $\Gamma \ll 1$, which means

$$S_{bal} \simeq |E_{LO}|^2 \Gamma \propto |E_{THz}| |E_{LO}|^2 \quad (4.33)$$

and we see the final result, that the difference signal is proportional to the magnitude of the terahertz electric field. That Γ is indeed much less than one can be seen by considering the values for r_{41} given earlier, and noting that $\Gamma = 1$ would require a terahertz field $\simeq 10^8$ V/m for a 1 mm crystal. Under the same conditions of $\alpha = 0$ and $\Gamma(\alpha) \ll 1$, equation 4.27 gives

$$S_{1Ch} = |E_{LO}|^2 \sin^2\left(\frac{\Gamma}{2}\right) \simeq \frac{E_{LO}^2}{4} \Gamma^2. \quad (4.34)$$

In both detection schemes, the power in the terahertz field, $P_{THz} \propto |E_{THz}|^2$ is modulated using a mechanical chopper at frequency f_{chop} , producing a corresponding modulation in the relative phase delay, Γ , between the optical probe field components along each of the crystal principal axes. A lock-in amplifier is then used to record only signal modulations at frequency f_{chop} , arising due to the dependence of the photocurrent on Γ in both cases. This further increases the signal to noise of the overall detection system. For our case, $f_{chop} \simeq 1$ kHz.

Comparing equations 4.33 and 4.34 shows that

$$\frac{S_{1Ch}}{S_{bal}} \simeq \frac{\Gamma}{4}, \quad (4.35)$$

and that, therefore, the balanced detection scheme gives greatly increased signal levels over those of the crossed polariser scheme. Indeed, it has been shown [74] that, for typical terahertz powers of several microwatts, the balanced detection scheme can provide signal levels three orders of magnitude greater than those from the crossed polariser scheme.

The proportionality in both cases to the power in the probe field should also be noted, as it allows the signal strength to be increased above the level of any instrument noise that may be present in the chosen detection system. Further, as the level of shot noise associated with this signal will

scale as the square root of the power in the probe, in the shot-noise-limited case the signal to noise ratio of the measurement system can be increased with increases in optical probe power, as is the case for direct detection of an optical field.

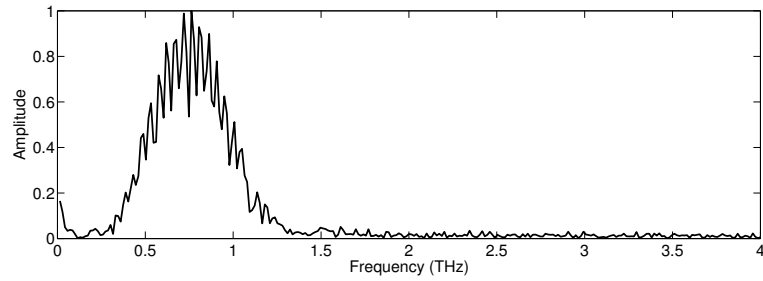
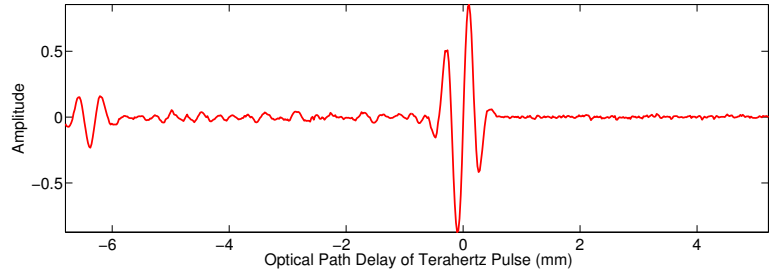
It is clear, therefore, that either a pair of photodiodes in a balanced configuration, or a single photodiode placed behind a crossed polariser allows the measurement of the induced polarisation rotation of the optical probe pulse due to the induced birefringence of the crystal in the presence of the terahertz field. As it is this terahertz field responsible for this change in birefringence, sweeping of the delay between the two pulses results in a direct measurement of the electric field, in contrast to conventional optical measurement techniques that are sensitive to only the intensity. As is common practice in terahertz time domain spectroscopy, the sensitivity of the apparatus is further increased through the use of lock in detection, whereby the optical pump beam is modulated at $\simeq 1.5$ kHz using a mechanical chopper, and the signal component at this modulation frequency is detected using a standard lock-in amplifier.

4.4 Results of Single Comb Detection Scheme

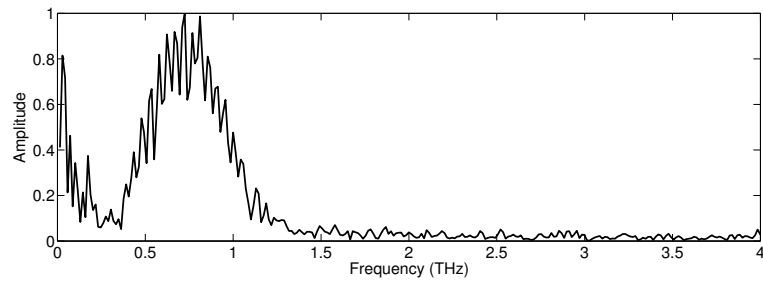
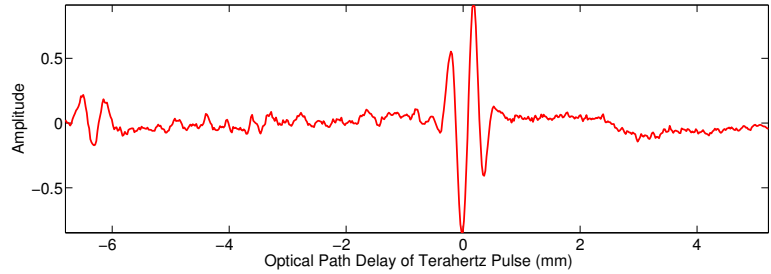
Figure 4.5 shows typical electro-optic sampling (EOS) traces of the terahertz electric field, obtained using the zinc telluride detection crystal and both the single channel (figure 4.5a) and balanced detection (figure 4.5b) schemes. In addition, the Fourier transform of the time-domain data traces are shown, indicating the spectral content of the terahertz field. In both cases, the time constant of the lock-in amplifier used was 30 ms. A measurement was recorded at changes in stage position of $20 \mu\text{m}$ in each case, and the amplifier allowed to settle for $\simeq 200$ ms for each reading.

Considering first figure 4.5a, one notes from the spectral form of the time domain trace a central frequency of $\simeq 0.75$ THz and a spectral bandwidth of $\simeq 0.5$ THz. The signal to noise ratio in the frequency domain is approximately 20 dB. Also of note is the secondary pulse, seen with a delay of approximately 6 mm from the main pulse, that can be attributed to

4.4. Results of Single Comb Detection Scheme



(a) Electro-optic sampling trace with single channel detector



(b) Electro-optic sampling trace acquired using balanced detection scheme.

Figure 4.5: Time-domain electro-optic sampling traces of the generated terahertz field, acquired with both a single channel detector and crossed polariser, and by balanced detection of orthogonal polarisation states, as explained in section 4.3. The spectral content of the signal is computed via Fourier transform.

4.4. Results of Single Comb Detection Scheme

etaloning effects of the terahertz pulse in the 1 mm zinc telluride detection crystal. That this is the case can be verified by calculating the optical path length corresponding to one roundtrip within the crystal, having a refractive index at the terahertz wavelength of $n(0.75 \text{ THz}) = 3.2$. Fresnel reflections at the crystal-air boundary due to the high refractive index contrast therefore cause a portion of the terahertz pulse to propagate through twice the thickness of the detection crystal, which will interfere with the optical probe pulse when the terahertz pulse is advanced with respect to the position of maximum signal by an optical path length $2 \times n(0.75 \text{ THz}) \times l \simeq 6.4 \text{ mm}$, where l is the thickness of the detection crystal. Likewise, the Fresnel reflections for such a refractive index contrast suggest that the pulse undergoing an additional two reflections at the crystal-air boundary is $\simeq \frac{1}{5}$ of the power of that passing straight through the crystal, in good agreement with the relative pulse amplitudes shown in figure 4.5a. That it is the terahertz pulse undergoing the additional reflections within the crystal, and not the optical pulse can be seen by the secondary pulse appearing for shorter delays of the terahertz pulse with respect to the optical probe. The Fourier transform of the time-domain EOS trace shows interference fringes as a result of this etaloning effect, with the fringes having spacing equal to the free spectral range of this ‘cavity’, or $\frac{c}{2n_{THz}l} \simeq 50 \text{ GHz}$.

Figure 4.5b shows an EOS trace obtained under similar experimental conditions to figure 4.5a, but using the balanced detection scheme described in section 4.3. The expected increase in signal level is not observed. This is attributed to difficulties with aligning the beam into the two detector channels and, in particular, with maintaining the coupling of each polarisation state into the photodiodes as the mechanical delay stage is swept. Indeed, the drift in dc signal level with mechanical delay is seen in the time domain trace, and this is reflected as a non-zero level of frequency components near dc in the Fourier transform.

4.4.1 Signal Scaling with Optical Probe Power

Equations 4.27 and 4.34 show that, in both the single channel and balanced detection schemes, the expected signal magnitude scales with the power in the optical probe field. In later work, we replace the sampling optical probe field with that from a separate mode-locked fibre laser. As this second laser lacks the high-power amplifier stage of that used here, we anticipate a reduction in the available optical power in the sampling field. We therefore seek to verify the scaling of the observed signal with optical probe power. To do this, the power in the probe beam was varied using standard neutral density optical filters, placed in the probe beam after the sampling plate used to pick off the probe pulse. The resulting time-domain traces can be seen in figure 4.6. That the photocurrent scales linearly with the intensity of the probe field, as predicted by equation 4.27, can be seen by plotting the magnitude of the peak of the non-normalised detected photocurrent signal with respect to the average power in the probe pulse, as in figure 4.7. It should be noted that this neglects any variation in the phase offset between the carrier wave of the terahertz field and the terahertz envelope. As seen from the shifting of the peaks of the carrier wave from the maxima of the envelope in figure 4.6, there is such a phase offset, likely due to the mismatch of the terahertz phase and group velocities in air. However, it is clear from figure 4.6 that this offset does not vary between scans, consistent with phase-group velocity mismatch over a fixed path length. Indeed, the only conditions that would give rise to a change in this offset would be a change in the total optical path length of the terahertz pulse. As this offset remains constant, it is reasonable to compare the peak of the electro-optic sampling signal between scans.

4.5 Conclusions

Our SC THz-TDS arrangement demonstrates signal to noise ratios of $\simeq 20$ dB for our available probe powers. In order to compare this to other work, we need to obtain a numerical estimate of the terahertz power of our system.

4.5. Conclusions

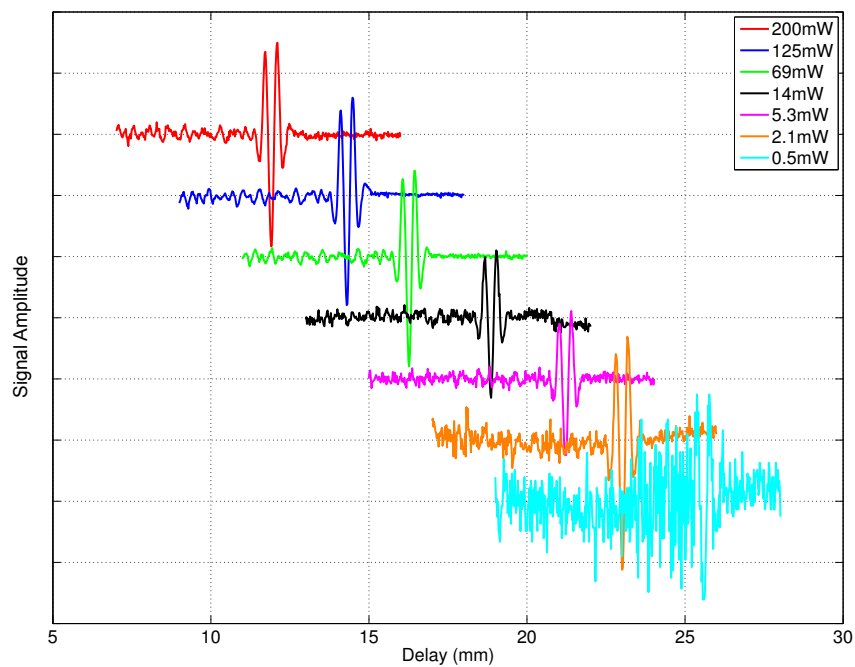


Figure 4.6: Resulting time-domain EOS traces for varying average powers of the optical probe pulse. The traces have been normalised to the peak signal of each trace and shifted in delay by 2 mm with respect to the preceding trace for clarity.

4.5. Conclusions

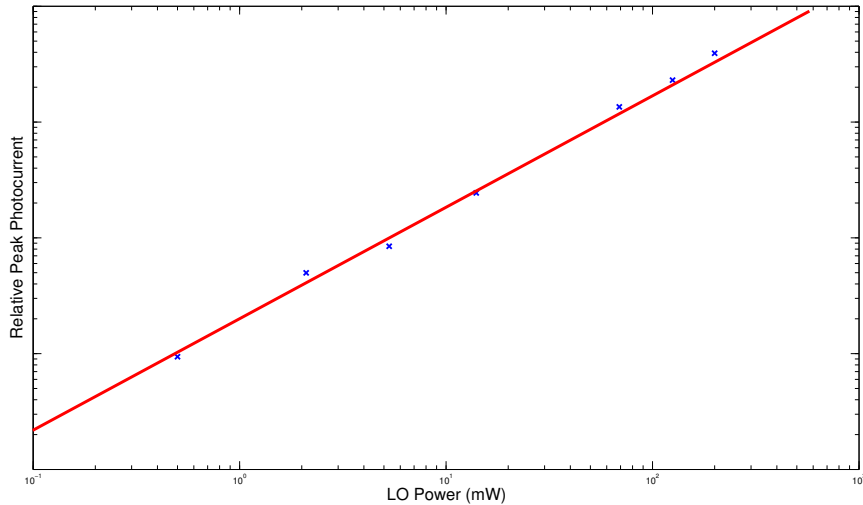


Figure 4.7: Scaling of the peak photocurrent observed from the single channel electro-optic sampling apparatus as a function of average power of the optical pulse. A dual logarithmic plot is used to overcome the difficulties in producing small changes in high average powers of the sampling pulse.

Such measurements are notoriously difficult, hence the prevalence of the electro-optic sampling technique used here, which produces a measurement of the terahertz electric field, but includes a response of the electro-optic material which is typically difficult to characterise sufficiently to allow an exact calibration [75], [76]. The most reliable way to produce an absolute measurement of the terahertz power is to use a helium-cooled bolometer, such as that used by [66]. Such instruments are slow and expensive to operate due to the need for helium cooling. Whilst solid state pyroelectric devices have been demonstrated [77], and indeed are now commercially available, these devices remain uncalibrated at frequencies lower than $\simeq 5$ THz. Further, the speed of these pyroelectric devices remains limited to around 5 Hz.

Rather than measure the terahertz power directly, we therefore extrapolate from the results of Chang et al. [66] who used an identical gallium phosphide wave guide emitter for terahertz generation via optical rectification. The terahertz power obtained in this case was $120 \mu\text{W}$ for a 14 W

4.5. Conclusions

optical pump. One notes that the central wavelength, observed terahertz spectrum, and driving optical wavelength are all comparable to our work, the only difference being additional amplification stages allowing higher optical pump powers. From equation 2.14, which states that the magnitude of the nonlinear polarisation at the difference frequency scales with the square of the driving electric field, one derives $P_{THz} \propto P_{opt}^2$, from which one estimates a total terahertz power of $2.5 \mu\text{W}$ for the experimental arrangement demonstrated in this thesis.

We now compare the performance of our SC THz-TDS system to the work of Hoffman et al. [78]. Whilst these authors use a different scheme for generation of the terahertz field, the result is comparable terahertz powers to that calculated above for our system. These authors use free-space electro-optic sampling in gallium phosphide to obtain signal to noise ratios of $\simeq 20$ dB, which is comparable to that observed in figure 4.5a.

In common with other THz-TDS experiments [21], [79], the need to sweep the mechanical delay line in our experiment results in difficulties maintaining the overlap of the optical and terahertz beams in the sampling crystal, and in long data acquisition times of four minutes for the data shown in figure 4.5. The following chapters discuss a method of overcoming these difficulties by eliminating the mechanical delay line.

Chapter 5

Dual-comb Spectroscopy in the Terahertz and Far-IR Region

5.1 Introduction

The use of mechanical delay lines in terahertz time domain spectrometry (THz-TDS) is fraught with drawbacks. Varying the optical path gives rise to changes in optical alignment and focussing which, in turn, will produce signal artefacts that are difficult to isolate from behaviour of the sample itself. Further, and perhaps more importantly, the speed with which the delay can be swept is limited, such that data acquisition is extremely time consuming. Note that the frequency resolution of such a spectrometer system depends on being able to vary the optical path length over large distances which, for the relatively slow velocities with which it is possible to vary the path delay, increases the required data acquisition time. For example, Mittleman and co-workers reported on a gas-sensing THz spectrometer that required tens of milliseconds in order to complete a single scan with adequate signal to noise [2].

The following chapter proposes a method of overcoming these drawbacks, whereby two mode-locked lasers, differing slightly in the pulse repetition rate, are used to provide the two required optical fields in a technique known as asynchronous electro-optic sampling (A-EOS) [80, 81]. In this method one mode-locked laser is amplified and used for generation of the terahertz field via either optical rectification [82] in a suitable nonlinear crystal, or by

driving a photoconductive antenna [80]. A second mode-locked laser is used to probe the terahertz field with a slight difference in pulse repetition rate, such that the pulse overlap between the terahertz and sampling field in the detection crystal is modulated at a frequency given by the repetition rate detuning, Δf_{rep} . In this way, all moving parts are eliminated, and the speed with which data can be acquired greatly increased [83].

Related techniques using detuned frequency combs have already been demonstrated at mid-to-near infrared wavelengths. For example, Schleiser et al. [84] demonstrated a Fourier transform spectrometer covering the spectral region 9-12 μm (25-33 THz) for real-time remote gas analysis. Further, Reinhardt et al. [85] have demonstrated such a system operating at near-IR wavelengths, in the spectral range 819-830 nm (362-368 THz) for spectroscopy of atomic transitions. More recently, the technique has been applied to the terahertz range. In particular, Bartels et al. [86], [83] have shown that asynchronous optical sampling of a terahertz frequency comb allows rapid acquisition of the spectral lines in water vapour. This system uses an electro-optic antenna to generate the terahertz pulse from a mode-locked titanium-sapphire oscillator operating at 800 nm, and a second sampling pulse from a similar oscillator to interrogate the terahertz field in a nonlinear zinc telluride crystal. The two oscillators have nominal pulse repetition rates of 1 GHz, but are detuned by $\Delta f_{rep}=10$ kHz by a system of rf electronic feedback to an intracavity piezo-electric actuator.

Barbieri et al. [87] recently showed that an optical femtosecond frequency comb (FFC) could be used to characterize a quantum cascade laser (QCL) operating at 2.5 THz. With a time domain analysis and subject to certain limitations on rf bandwidth, they showed that A-EOS can be used to map the THz frequency comb (THz FC) of a QCL to an rf photocurrent, demonstrating the comb nature of the QCL output.

In this section we complete a fully frequency domain analysis of A-EOS. Using this technique (which is a new form of dual-comb spectroscopy employing electro-optic sampling) our results indicate it is possible to pursue wideband precision spectroscopy in the far-IR and THz spectral regions by directly converting the far-IR/THz frequency combs to the rf domain. To

this end, we show that it is possible to significantly improve the frequency resolution of the technique developed in [80] such that the individual comb elements of the THz FC are recorded. Such a technique would allow the Hz-level frequency resolution [23] previously discussed (see section 1.1.3) to be of such interest at these frequencies.

Figure 5.1 outlines the key steps in the detection process. In the first step, the A-EOS process creates a comb of sidebands adjacent to each element of the optical local oscillator comb used to interrogate the THz FC. As shown in figure 5.1, each set of sidebands contains the full spectral information of the original THz FC and therefore represents a scaled copy of the THz FC. A subsequent direct heterodyne detection process on a fast photodetector beats each set of sidebands with the nearest LO comb element to produce the rf frequency spectrum shown in figure 5.1. We show, with a full frequency domain analysis and subject to appropriate limitations on the repetition rate detuning, that each of the resulting rf comb elements is produced by a single element of the THz FC. Further, the comb of rf beat frequencies is symmetrical about every half pulse repetition rate of the sampling optical comb. One can therefore recover the entire spectral information of the original THz FC by recording, for example, the frequency content between dc and half the pulse repetition rate, as illustrated in figure 5.1. Spectroscopy of a sample can be performed by repeating this measurement with and without the sample placed in the THz FC beamline.

We show here, with a fully frequency domain treatment, that optical rectification of an optical FFC results in a THz FC and, further, that asynchronous electro-optic sampling of this THz FC with a second, detuned local oscillator (LO) FFC writes a comb of rf phase sidebands onto the sampling optical pulse. Subsequent heterodyne beating of this modulated optical comb gives rise to a comb of rf frequencies, with the crucial characteristic that each rf comb element is produced by beating processes involving one and only one element of the original terahertz comb. In this manner, a single, unique copy of the original terahertz field is created at readily detectable rf frequencies.

The nature of each frequency comb at each stage of the experimental

5.1. Introduction

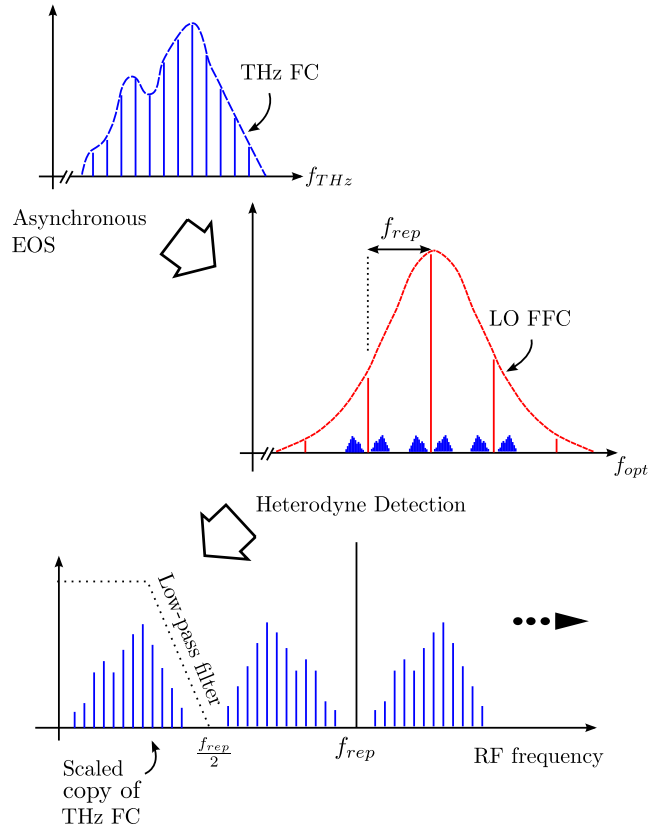


Figure 5.1: Overview of the multi-frequency heterodyne detection scheme for the dual-comb terahertz spectrometer. Asynchronous electro-optic sampling (A-EOS) results in a scaled copy of the original THz frequency comb (THz FC) being created adjacent in frequency to each element of the local oscillator (LO) optical comb. Further mixing of these sidebands with the LO comb during the direct heterodyne detection process produces a comb of rf frequencies, periodic in the pulse repetition rate of the LO comb and symmetric about half the pulse repetition rate. Careful analysis (see text) shows that each rf comb element arises from a single THz FC comb element, such that the full spectral content of the original THz FC is contained within a frequency range less than half the LO pulse repetition rate, where it may be recovered electronically.

arrangement is shown in figure 5.2. A THz FC is generated by difference frequency generation (DFG) from an optical FFC with a repetition rate $f_{rep} + \Delta f_{rep}$. In the case where the THz FC is generated using a single optical comb the former necessarily has a zero offset frequency, as explained in section 2.1. This distinction is made as recent work [88] has demonstrated that DFG between two optical FFCs can extend the bandwidth of the difference frequency comb up to the mid-infrared. In this case, the following theory still applies, but one must be careful to include the resulting offset frequency of the difference frequency comb.

The generated THz FC is used to probe a sample that imparts phase and amplitude changes onto this comb. It is this terahertz spectroscopic data that we seek to transfer into the rf region of the spectrum, where it may be easily detected and analysed using conventional electronics. This is achieved by using a second optical FFC, the LO FFC. The THz FC has a repetition rate that is detuned from that of the LO FFC, f_{rep} , by an amount Δf_{rep} . Upon mixing with the terahertz comb in a second nonlinear crystal, referred to henceforth as the electro-optic sampling (EOS) crystal, a polarisation modulation is produced by the EOS process. Due to the differing repetition rates of the two combs, this results in a set of polarisation modulation sidebands being written onto each comb element of the LO FFC. As we show in the following section, direct detection of the LO FFC produces a comb of rf frequency modulations, each frequency element of which correspond uniquely to a particular terahertz comb element, allowing recovery of both the phase and amplitude spectroscopic data.

5.2 Mapping of a Terahertz Frequency Comb to the Radio Frequency Spectral Region via Asynchronous Electro-optic Sampling

In the frequency domain EOS can be viewed as sum frequency generation (SFG) and DFG [89] between the LO FFC (serving as the probe) and the

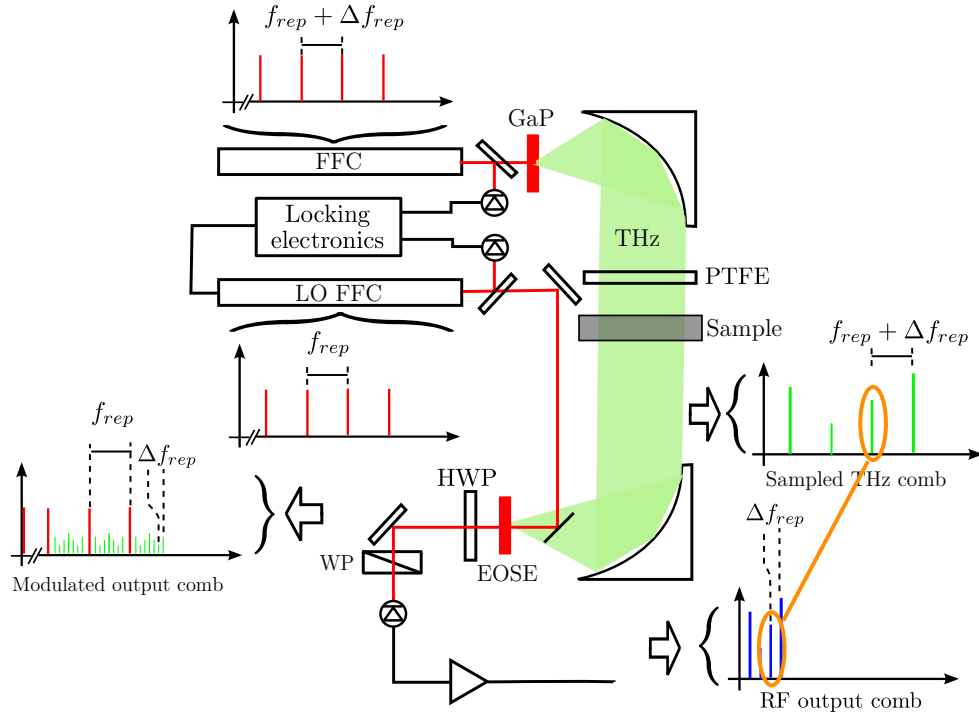


Figure 5.2: Schematic of a terahertz spectrometer where the pump femtosecond frequency comb (FFC) and local oscillator (LO FFC) frequency combs differ in pulse repetition rate by an amount Δf_{rep} . The terahertz frequency comb (THz-FC) is generated by difference frequency generation in a nonlinear crystal (GaP). After passing through the sample to be studied, the terahertz comb is electro-optically sampled using the detuned LO frequency comb in a second nonlinear crystal, the electrooptic sampling element (EOSE). Following a polariser, direct detection of the sampled LO frequency comb completes an element-by-element mapping from the terahertz frequency range to the rf domain.

THz FC². In the following section, we show that the SFG and DFG processes of asynchronous electro-optic sampling create sidebands adjacent to each element of the LO FFC, within each set of which is contained the full spectral and amplitude information of the original THz FC, as in figure 5.3a) and c). We refer to these sidebands as A-EOS sidebands. Subsequently, we will show that the beating process arising from direct detection of the A-EOS sidebands with the original LO FFC on a fast photodetector creates an rf photocurrent, itself having many comb elements, each corresponding to a unique element of the original THz FC, as illustrated in Fig 5.3b).

We begin our analysis by considering the polarization rotation imparted via SFG and DFG onto the LO FFC through the asynchronous electro-optic sampling process. The fields incident on a polarisation beam splitter placed behind the nonlinear detection crystal consist of the original LO FFC, as well as those fields produced through SFG and DFG with the THz FC³. We write these latter two fields as $\vec{E}_{EOS}^{SFG}(t)$ and $\vec{E}_{EOS}^{DFG}(t)$ respectively. The total incident field at time t can then be written

$$\vec{E}_{tot} = \vec{E}_{LO}(t) + \vec{E}_{EOS}^{SFG}(t) + \vec{E}_{EOS}^{DFG}(t). \quad (5.1)$$

Let the transmission axes of the polarising beam splitter be denoted \hat{x} and \hat{y} . The fields along these axes are then

$$\vec{E}_{tot}(t) = E_{tot,x}(t)\hat{x} + E_{tot,y}(t)\hat{y}, \quad (5.2)$$

where

$$\begin{aligned} E_{tot,x}(t) &= E_{LO,x}(t) + E_{EOS,x}^{SFG}(t) + E_{EOS,x}^{DFG}(t) \\ E_{tot,y}(t) &= E_{LO,y}(t) + E_{EOS,y}^{SFG}(t) + E_{EOS,y}^{DFG}(t). \end{aligned} \quad (5.3)$$

²Whilst it is intuitive to think of A EOS as the mixing of differing frequency elements, the same can be seen to be true of conventional EOS employing a swept mechanical delay by realising that the effect of the mechanical delay is to Doppler-shift the frequency elements of the portion of the optical FFC used as the LO by an amount $2f_{rep}\frac{v}{c}$, where v is the sweep velocity of the mechanical delay [25].

³Of course, the THz FC itself propagates through to the detector also, but as our detector is not sensitive to such long wavelengths we need not include it here.

5.2. Terahertz to RF Comb Mapping

We follow the procedure of [89] and rewrite these polarisation components as

$$\begin{aligned} E_{tot,x}(t) &= E_{LO,x}(t) (1 + i\varphi_x(t)) \\ E_{tot,y}(t) &= E_{LO,y}(t) (1 + i\varphi_y(t)) \end{aligned} \quad (5.4)$$

where the phase modulations, $\varphi_x(t)$ and $\varphi_y(t)$ are given by

$$\begin{aligned} \varphi_x(t) &= \frac{E_{EOS,x}^{SFG}(t) + E_{EOS,x}^{DFG}(t)}{iE_{LO,x}(t)} \\ \varphi_y(t) &= \frac{E_{EOS,y}^{SFG}(t) + E_{EOS,y}^{DFG}(t)}{iE_{LO,y}(t)}. \end{aligned} \quad (5.5)$$

For reasonable field amplitudes $\varphi_x, \varphi_y \ll 1$ thus equation 5.4 can be well approximated by

$$\begin{aligned} E_{tot,x}(t) &= E_{LO,x}(t) \exp(i\varphi_x(t)) \\ E_{tot,y}(t) &= E_{LO,y}(t) \exp(i\varphi_y(t)). \end{aligned} \quad (5.6)$$

The effect of the SFG and DFG fields is therefore to create an amplitude modulation in the orthogonal polarisation states of the measured LO field. This amplitude modulation can be recorded either directly using a crossed-polariser geometry, or by using ellipsometry involving balanced detection of orthogonal polarizations, analogous to the schemes demonstrated in section 4.3. The simultaneous mixing of multiple comb elements via both SFG and DFG necessitate careful consideration in order to verify the unique mapping of the THz FC elements to a corresponding heterodyne beat in the rf domain of the resulting signal. We will show that, in the case where the LO and THz fields are of the form of broadband, detuned FCs, the resulting amplitude modulation can be described by phase modulation sidebands of the original LO FFC.

5.2. Terahertz to RF Comb Mapping

The mode-locked oscillator used as the LO FFC can be described by,

$$E_{LO}(z, t) = \sum_M A_{LO}(z, \omega_M) \exp(-i\omega_M t) \quad (5.7)$$

where $A_{LO}(z, \omega_M)$ is the complex spectral amplitude of the frequency component at frequency ω_M and location z respectively. We include within the complex spectral amplitude the spectral phase of the LO FFC. The discrete comb elements are indexed by M ,

$$\omega_M = 2\pi(Mf_{rep} + f_0) \quad (5.8)$$

where f_{rep} is the laser pulse repetition rate, f_0 is the carrier-envelope offset frequency, and M runs over the bandwidth of the laser. The THz FC, generated via DFG with an optical FFC that has an element spacing (repetition rate) of $(f_{rep} + \Delta f_{rep})$ can be described by,

$$E_{THz}(z, t) = \sum_N A_{THz}(z, \Omega_N) \exp(-i\Omega_N t) \quad (5.9)$$

Again, the complex spectral amplitude $A_{THz}(z, \Omega_N)$ includes within it the spectral phase of the N^{th} THz comb element. As this THz FC is assumed to be generated by DFG of optical comb elements having the same offset frequency, there is zero offset frequency of the THz FC comb elements. The comb elements are indexed by N and, further

$$\Omega_N = 2\pi N(f_{rep} + \Delta f_{rep}). \quad (5.10)$$

The nonlinear polarization produced by a single THz FC element at frequency Ω_N due to the SFG process is given by,

$$P_{\Omega_N}(z)^{\omega_M + \Omega_N}(z) = \chi^{(2)}(\omega_M + \Omega_N; \omega_M, \Omega_N) A_{LO}(z, \omega_M) A_{THz}(z, \Omega_N) \quad (5.11)$$

and, for the DFG process,

$$P_{\Omega_N}(z)^{\omega_P - \Omega_N}(z) = \chi^{(2)}(\omega_P - \Omega_N; \omega_P, \Omega_N) A_{LO}(z, \omega_P) A_{THz}^*(z, \Omega_N) \quad (5.12)$$

5.2. Terahertz to RF Comb Mapping

where the index P is introduced to index the LO FFC during DFG. Throughout this discussion, we use a frequency superscript to indicate a quantity that varies in time with the indicated frequency, whilst a subscript argument indicates the frequency of the THz FC element producing the particular LO sideband. $P_{\Omega_N}^{\omega_M + \Omega_N}(z)$ therefore represents a nonlinear polarization at frequency $(\omega_M + \Omega_N)$ produced by the SFG process between the THz FC line at frequency Ω_N and the optical LO FFC element at frequency ω_M , whilst $P_{\Omega_N}^{\omega_P - \Omega_N}(z)$ represents the nonlinear polarization due to the DFG process between the LO FFC element at frequency ω_P and the THz FC line at frequency Ω_N .

We now follow the principals of section 2.1 and assume that the field radiated as a result of the nonlinear polarisation of equations 5.11 and 5.12 satisfies the slowly varying amplitude approximation. That is, the amplitude of the radiated field varies slowly on the scale of the wavelength. The radiated field amplitude, A_{EOS} , of the sampled LO FFC at frequency $\omega_M + \Omega_N$ at position z in the nonlinear detection crystal due to SFG therefore satisfies a wave equation of the form of equation 2.19,

$$\left[\frac{\partial}{\partial z} + \beta(\omega_M + \Omega_N) \right] A_{EOS}(z, \omega_M + \Omega_N) = \frac{2\pi i (\omega_M + \Omega_N)^2}{c^2 k'(\omega_{M+N})} P_{\Omega_N}^{\omega_M + \Omega_N}(z) \exp(i\Delta k'_+ z - [\beta(\Omega_N) + \beta(\omega_M)] z). \quad (5.13)$$

Similarly for DFG,

$$\left[\frac{\partial}{\partial z} + \beta(\omega_P - \Omega_N) \right] A_{EOS}(z, \omega_P - \Omega_N) = \frac{2\pi i (\omega_P - \Omega_N)^2}{c^2 k'(\omega_{P-N})} P_{\Omega_N}^{\omega_P - \Omega_N}(z) \exp(i\Delta k'_- z - [\beta(\Omega_N) + \beta(\omega_P)] z), \quad (5.14)$$

where $\Delta k'_+ = k'(\omega_M) + k'(\Omega_N) - k'(\omega_M + \Omega_N)$ and $\Delta k'_- = k'(\omega_P) - k'(\Omega_N) - k'(\omega_P - \Omega_N)$ correspond to the wavevector mismatches in the SFG and DFG cases respectively. For consistency with [89], we use $k = k' + i\beta$ such that k' represents the real part of the wavevector, and β the absorption coefficient.

5.2. Terahertz to RF Comb Mapping

Substituting in the previously derived nonlinear polarizations of Eqs. 5.11 and 5.12, and integrating over the length, l of the nonlinear crystal, we obtain

$$\begin{aligned}
 A_{EOS}(l, \omega_M + \Omega_N) &= \frac{2\pi i (\omega_M + \Omega_N)^2}{c^2 k'(\omega_{M+N})} \chi^{(2)}(\omega_M + \Omega_N; \omega_M, \Omega_N) \\
 &\times \frac{\exp(i\Delta k_+ l) - 1}{i\Delta k_+} \exp(-\beta(\omega_M + \Omega_N)l) \\
 &\times A_{LO}(\omega_M) A_{THz}(\Omega_N), \tag{5.15}
 \end{aligned}$$

for the SFG term, and

$$\begin{aligned}
 A_{EOS}(l, \omega_P - \Omega_N) &= \frac{2\pi i (\omega_P - \Omega_N)^2}{c^2 k'(\omega_{P-N})} \chi^{(2)}(\omega_P - \Omega_N; \omega_P, \Omega_N) \\
 &\times \frac{\exp(i\Delta k_- l) - 1}{i\Delta k_-} \exp(-\beta(\omega_P - \Omega_N)l) \\
 &A_{LO}(\omega_P) A_{THz}^*(\Omega_N), \tag{5.16}
 \end{aligned}$$

for the DFG term. We make the undepleted pump approximation and assume $A_{LO}(z, \omega)$ and $A_{THz}(z, \Omega)$ to be constant in z . Substituting the frequency equations 5.8 and 5.10, and summing over the LO FFC elements gives the total field due to the THz FC element at frequency $\Omega_N = N(f_{rep} + \Delta f_{rep})$

$$\begin{aligned}
 E_{EOS, \Omega_N}^{SFG}(l, t) &= \sum_M \left[\frac{2\pi i (\omega_M + \Omega_N)^2}{c^2 k'(\omega_{M+N})} \chi^{(2)}(\omega_M + \Omega_N; \omega_M, \Omega_N) \right. \\
 &\times \frac{\exp(i\Delta k_+ l) - 1}{i\Delta k_+} \exp(-\beta(\omega_M + \Omega_N)l) \\
 &\times A_{LO}(\omega_M) A_{THz}(\Omega_N) \\
 &\left. \times \exp(-2i\pi ((M + N)f_{rep} + N\Delta f_{rep}) t) \right], \tag{5.17}
 \end{aligned}$$

and

$$\begin{aligned}
 E_{EOS,\Omega_N}^{DFG}(l, t) = & \sum_P \left[\frac{2\pi i (\omega_P - \Omega_N)^2}{c^2 k'(\omega_{P-N})} \chi^{(2)}(\omega_P - \Omega_N; \omega_P, \Omega_N) \right. \\
 & \times \frac{\exp((i\Delta k_- l)) - 1}{i\Delta k_-} \exp(-\beta(\omega_P - \Omega_N)l) \\
 & \times A_{LO}(\omega_P) A_{THz}^*(\Omega_N) \\
 & \left. \times \exp(-2\pi i ((P - N)f_{rep} - N\Delta f_{rep}) t) \right]. \quad (5.18)
 \end{aligned}$$

Focussing solely on the time dependence of the above expressions, it can be seen that each THz FC line of frequency Ω_N produces a sideband on every LO FFC element (at frequency ω_M for the SFG case, and ω_P in the DFG case), with the spacing of that sideband from the LO FFC element from which it is derived being equal to the THz frequency $\Omega_N = N(f_{rep} + \Delta f_{rep})$. As this spacing is not a multiple of f_{rep} (the spacing of the LO FFC elements themselves) each THz sideband is displaced from an LO FFC element other than that used in its generation by an amount $N\Delta f_{rep}$. Further, we note that this is true for both the SFG and DFG cases, with the THz sideband being greater or lesser in frequency than the nearest LO FFC element in the SFG or DFG cases respectively. By considering the SFG and DFG processes within the same LO FFC spectral interval, we note that that the $M + N + 1^{th}$ LO FFC element in the SFG case corresponds to the $P - N^{th}$ LO FFC element in the DFG case. This enables us to express equations

5.2. Terahertz to RF Comb Mapping

5.17 and 5.18 as a single sum,

$$\begin{aligned}
E_{EOS,\Omega_N}(l,t) = & \frac{2\pi i}{c^2} \sum_M \left[\left[\frac{(\omega_M + \Omega_N)^2}{k'(\omega_{M+N})} \chi^{(2)}(\omega_M + \Omega_N; \omega_M, \Omega_N) \right. \right. \\
& \times \frac{\exp(i\Delta k_+ l) - 1}{i\Delta k_+} A_{LO}(\omega_M) A_{THz}(\Omega_N) \\
& \left. \left. \times \exp(-2\pi i ((M + N)f_{rep} + N\Delta f_{rep}) t) \right] \right. \\
& + \left[\frac{(\omega_{M+2N+1} - \Omega_N)^2}{k'(\omega_{M+N+1})} \chi^{(2)}(\omega_{M+2N+1} - \Omega_N; \omega_{M+2N+1}, \Omega_N) \right. \\
& \times \frac{\exp(i\Delta k_- l) - 1}{i\Delta k_-} A_{LO}(\omega_{M+2N+1}) A_{THz}^*(\Omega_N) \\
& \left. \left. \times \exp(-2\pi i ((M + N + 1)f_{rep} - N\Delta f_{rep}) t) \right] \right] \quad (5.19)
\end{aligned}$$

It is important to note this sum represents the sidebands resulting from a single THz FC element, specifically the N^{th} element. When we consider the THz FC in its entirety, we find the final result that a sideband corresponding to each element of the THz FC is created both above and below every single LO FFC element, as shown in figure 5.3, and we refer to these sidebands as A-EOS sidebands. In general, these sidebands will have a different polarization to that of the LO FFC. In order to observe a heterodyne beat between these field components, we use either an optical polarizer to take parallel projections of the original LO FFC and A-EOS sidebands, or a quarter waveplate and balanced detection of orthogonal polarization states, as in the case of ellipsometry discussed in [89].

Having fully described the nature of the A-EOS sidebands written onto the LO FFC by the THz FC, and henceforth referring to this modulated comb as the sampled LO FFC, we now consider the direct detection process of this modulated comb, using a polariser to take parallel projections of the modulation sidebands and the original LO elements.

With a judicious choice of Δf_{rep} the direct detection process produces rf modulation frequencies in the four main bands as shown in figure 5.3 b). First we start with the A-EOS SFG sidebands, connected graphically

5.2. Terahertz to RF Comb Mapping

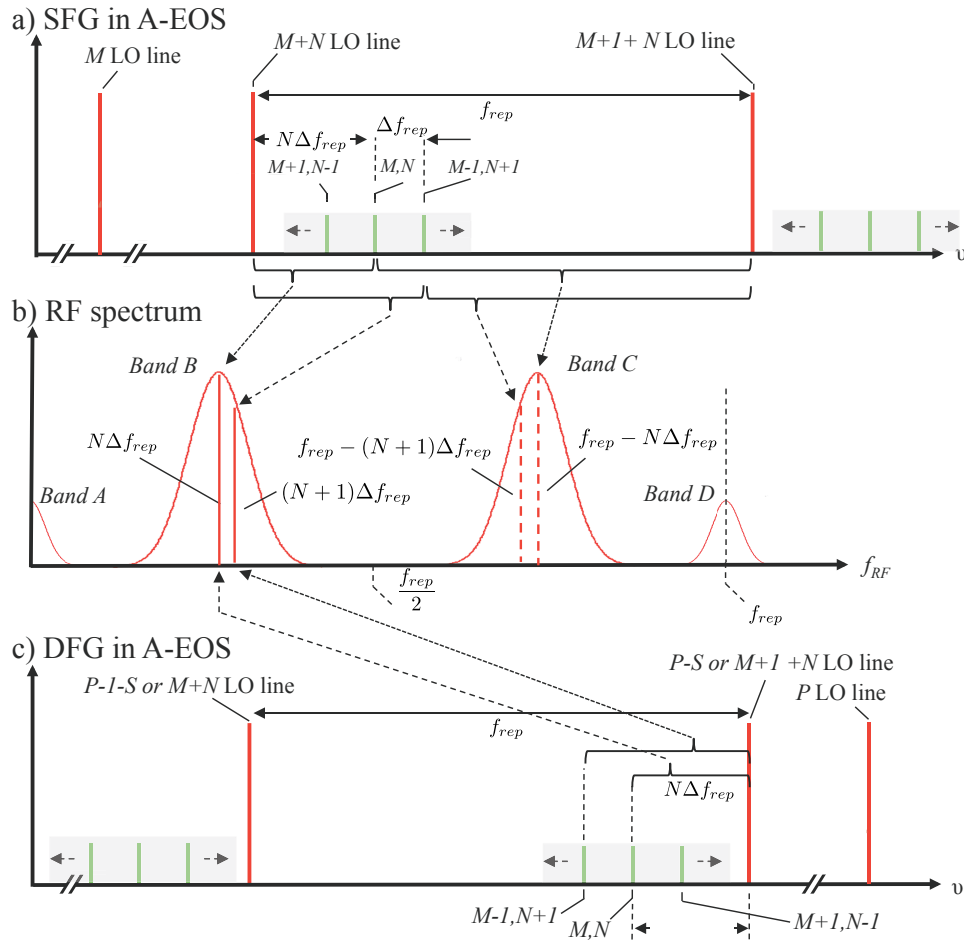


Figure 5.3: a) Optical frequency spectrum of the LO FFC after SFG with the THz FC. In the SFG process, the N^{th} THz FC element writes a sideband onto the M^{th} LO FFC element, producing a modulation at a frequency near the $(M + N)^{\text{th}}$ LO FFC element. b) RF spectrum of directly-detected photocurrent due to the modulated LO FFC obtained through asynchronous optical sampling. Four bands of heterodyne beats are formed. Of interest are the middle two bands (which are conjugate pairs) as each rf beat within these bands is created by a unique element of the THz FC. c) Optical spectrum of the LO FFC after difference frequency generation (DFG). Similar to SFG, the process of DFG writes a group of sidebands onto the LO FFC and, after direct detection of the sampled LO, there is the same unique mapping of a particular THz FC element to a unique rf heterodyne beat as shown in b).

between panels a) and b). *Bands A* and *D* result from the intra-A-EOS sideband beating and as they are very low in power they are not considered further. Of more interest is the range of beat frequencies due to beating of the M^{th} group of A-EOS SFG sidebands with the $(M + N)^{th}$ LO FFC element (*Band B*). A third group of beat frequencies (*Band C*) is due to the M^{th} group of A-EOS SFG sidebands mixing with the $(M + N) + 1^{th}$ LO element as shown in figure 5.3b). This group of beats is a mirror image of *Band B*, reflected about $f_{rep}/2$. Continuing this analysis shows each group of sidebands beats with its nearest and next nearest LO elements and contributes an identical beat structure to the rf spectrum shown in figure 5.3 b).

The DFG sidebands will also contribute to the photodetector's rf signal generating a similar set of bands of rf frequencies within the range dc to f_{rep} in the photodetection signal. In the central two bands, the N^{th} A-EOS DFG sidebands will appear as an rf beat at exactly the same frequency as the N^{th} A-EOS SFG sidebands. This overlap is shown pictorially in figure 5.3 b). Similar to the SFG case, each group of A-EOS DFG sidebands beats with its nearest and next nearest LO elements. Herein lies the key point: for A-EOS to be employed as a detection method for multi-frequency heterodyne THz spectroscopy each rf beat must result from one and only one THz FC element. Indeed this is the case, as the N^{th} mode of THz FC is the only element responsible for generating the rf beat at $N\Delta f_{rep}$ from both SFG and DFG sidebands. Limits on Δf_{rep} necessary to produce this unique mapping are discussed below.

The photocurrent due to the simultaneously incident A-EOS sidebands and LO fields is proportional to the square of the electric field described by equation 5.1 [90],

$$S(l, t) \propto |\vec{E}_{LO}(t) + \vec{E}_{EOS}^{SFG}(l, t) + \vec{E}_{EOS}^{DFG}(l, t)|^2. \quad (5.20)$$

Neglecting the dc photocurrent terms corresponding to each of the LO and A-EOS fields incident on the detector individually, and subject to the bandwidth limitations discussed, one obtains the time-varying term due to the

5.2. Terahertz to RF Comb Mapping

mixing of the LO field with the A-EOS sideband.

$$S_{\Omega_N}(l, t) \propto E_{EOS, \Omega_N}^{SFG}(l, t) E_{LO}^*(l, t) + E_{EOS, \Omega_N}^{DFG^*}(l, t) E_{LO}(l, t). \quad (5.21)$$

Substituting in equations 5.7, 5.8, 5.17 and 5.18 yields,

$$\begin{aligned} S_{\Omega_N}(l, t) \propto & \frac{2\pi i}{c^2} \sum_M \left[\left[\frac{(\omega_M + \Omega_N)^2}{k'(\omega_{M+N})} \chi^{(2)}(\omega_M + \Omega_N; \omega_M, \Omega_N) \right. \right. \\ & \times \frac{\exp(i\Delta k_+ l) - 1}{i\Delta k_+} A_{LO}(\omega_M) A_{THz}(\Omega_N) A_{LO}^*(\omega_{M+N}) \\ & \times \exp(-2\pi i [((M + N) - (M + N)) f_{rep} + N\Delta f_{rep}] t) \left. \right] \\ & + \left[\frac{(\omega_{M+2N+1} - \Omega_N)^2}{k'(\omega_{M+N+1})} \chi^{(2)}(\omega_{M+2N+1} - \Omega_N; \omega_{M+2N+1}, \Omega_N) \right. \\ & \times \frac{\exp(i\Delta k_- l) - 1}{i\Delta k_-} A_{LO}^*(\omega_{M+2N+1}) A_{THz}(\Omega_N) A_{LO}(\omega_{M+N+1}) \\ & \left. \left. \times \exp(-2\pi i [((M + N + 1) - (M + N + 1)) f_{rep} + N\Delta f_{rep}] t) \right] \right]. \end{aligned} \quad (5.22)$$

Upon simplifying the time dependence in the exponential terms, and taking relevant terms outside the sum, the true characteristics of this heterodyne comb become clear:

$$\begin{aligned} S_{\Omega_N} \propto & A_{THz}(\Omega_N) \exp(-2\pi i N \Delta f_{rep} t) \\ & \frac{2\pi i}{c^2} \sum_M \left[\left[\frac{(\omega_M + \Omega_N)^2}{k'(\omega_{M+N})} \chi^{(2)}(\omega_M + \Omega_N; \omega_M, \Omega_N) \right. \right. \\ & \times \frac{\exp(i\Delta k_+ l) - 1}{i\Delta k_+} A_{LO}(\omega_M) A_{LO}(\omega_{M+N}) \left. \right] \\ & + \left[\frac{(\omega_{M+2N+1} - \Omega_N)^2}{k'(\omega_{M+N+1})} \chi^{(2)}(\omega_{M+2N+1} - \Omega_N; \omega_{M+2N+1}, \Omega_N) \right. \\ & \left. \times \frac{\exp(i\Delta k_- l) - 1}{i\Delta k_-} A_{LO}(\omega_{M+2N+1}) A_{LO}^*(\omega_{M+N+1}) \right]. \end{aligned} \quad (5.23)$$

5.3. Effect of Spectral Phase on Heterodyne Beat Signal

The term outside the sum can be rewritten

$$A_{THz}(\Omega_N) \exp(-2\pi i N \Delta f_{rep} t) = A_{THz}(\Omega_N) \exp\left(-i\Omega_N \frac{\Delta f_{rep}}{f_{rep}} t\right). \quad (5.24)$$

Comparison with equation 5.9 therefore shows that the final result of equation 5.23 is analogous to a map of the original THz FC, but scaled in frequency by a factor $\frac{\Delta f_{rep}}{f_{rep}}$ and weighted by the amplitude and phase of the LO FFC, as well as the phase-matching and nonlinear susceptibility terms due to the optical mixing processes. Recalling that the dc photocurrent terms corresponding to the photocurrents measured if any of the fields E_{LO} , E_{EOS}^{SFG} or E_{EOS}^{DFG} are detected independently were neglected in deriving equation 5.21, the final signal can be seen to have the form of, in the time domain, the sum of these dc photocurrents, upon which is written an amplitude modulation at rf frequencies described by equation 5.23. With appropriate rf filtering, only those modulations at frequencies within the range of *Band B*, as indicated in figure 5.3 will be observed.

Assuming the strong dc portion of the signal to be removable with conventional electronic filtering techniques, we now turn our attention to an analysis of the factors affecting the magnitude of the rf modulation. The sum over the optical LO FFC elements will vary with the spectral phase of the input fields, and with the wavevector mismatch in the nonlinear material used for the EOS crystal. If the SFG and DFG signal components generated by a single THz FC element at frequency Ω_N have opposite phases, for example, one can expect significant degradation of the heterodyne beat signal at frequency $N\Delta f_{rep}$. The effect of the LO FFC spectral phase, and the wavevector mismatch on the magnitude of the heterodyne beat signal forms the basis of the following section.

5.3 Effect of Spectral Phase on Heterodyne Beat Signal

Consider again equation 5.23. There is, contained within the complex spectral amplitude A_{LO} of the local oscillator a spectral phase associated with

5.3. Effect of Spectral Phase on Heterodyne Beat Signal

each and every optical comb element. Whilst a given rf comb element is produced by the beating of many optical sidebands with their respective nearest neighbour, it is seen from equation 5.23 that every single sideband contributing to a given rf comb element is produced by a single terahertz comb element, allowing the full structure of the THz FC to be retrieved using commonly available rf electronics. The amplitude of any given rf comb element will, however, depend on the phase distribution of the many optical sidebands involved in its generation, and of the LO FFC elements with which they are mixed. This can be understood by considering the spectral phase terms within the sum of equation 5.23. If the spectral phase of the optical comb is flat, such that all the terms within the sum have the same phase, the amplitude of the signal will be a maximum. In contrast, any spectral chirp to the optical LO comb will reduce the amplitude of the heterodyne beat, due to the phase mismatch between contributions to the single rf frequency. Here we consider the effect of various contributions to the spectral chirp of the LO comb on the heterodyne beat signal.

In general, the output pulse from a fibre oscillator such as that used to provide the LO comb in this work will exhibit a non-uniform spectral phase distribution due to the combined effects of material and waveguide dispersion, as described in section 2.4.2, as well as the nonlinear phase shift resulting from the intensity dependence of the material refractive index. Recall expression 2.36 describing the propagation of an optical pulse in a dispersive medium:

$$E(z, t) = e^{i\omega_c t} \int \tilde{E}(0, \Omega) e^{i(\Omega t - \beta(\omega_c + \Omega)z)} d\Omega, \quad (5.25)$$

and the Taylor expansion of the propagation constant $\beta(\omega_c + \Omega)$ thus,

$$\beta(\omega_c + \Omega) = \beta(\omega_c) + \left. \frac{d\beta}{d\omega} \right|_{\omega_c} \Omega + \frac{1}{2} \left. \frac{d^2\beta}{d\omega^2} \right|_{\omega_c} \Omega^2 + \frac{1}{6} \left. \frac{d^3\beta}{d\omega^3} \right|_{\omega_c} \Omega^3 + \dots, \quad (5.26)$$

where ω_c and Ω are the optical carrier frequency and $\omega = \omega_c + \Omega$, as defined in section 3.3.3. The electric field of the local oscillator comb, having propagated a distance z in the silica fibre components composing the oscillator

5.3. Effect of Spectral Phase on Heterodyne Beat Signal

and subsequent amplifier stages, can therefore be rewritten

$$E(z, t) = e^{i\omega_c t} \int \tilde{E}(0, \Omega) \exp(+i\Omega t - ikz - \frac{i}{2}\beta_2\Omega^2 z - \frac{i}{6}\beta_3\Omega^3 z) d\Omega, \quad (5.27)$$

where $\beta_i = \frac{d^i\beta}{d\omega^i}$ and β_2 and β_3 are the GVD and TOD parameters respectively. $\beta_2 z$ is the total second order group delay dispersion (GDD). The combined effect of material and waveguide dispersion is therefore to write onto the electric field a spectral phase consisting of terms proportional to increasing powers of the optical frequency Ω .

As a specific example for illustration, we consider here the effect of a non-uniform spectral phase of the LO FFC on the heterodyne beat signal resulting from the N^{th} THz FC element and assume perfect phase-matching, the subject of which forms the basis of the following section. We choose an LO FFC centered at 1030 nm and a THz FC element at 0.85 THz ($N = 8500$ for $f_r = 100$ MHz) based on recent successes producing these THz frequencies using ytterbium-doped fiber lasers [65].

We plot in figure 5.4 the effect of spectral phase terms up to quadratic and cubic dependence on the optical frequency, corresponding to group velocity and third order dispersion are included. The effect of fourth order dispersion was also calculated but found to have no significant effect on the calculated signal amplitude. Figure 5.4 shows that the signal falls off relatively quickly as the pulse is temporally broadened due to GVD. Indeed, the point at which the signal falls to half its expected peak, for a total group delay of $\simeq 1.5 \times 10^4$ fs², corresponds to an optical pulse duration of 170 fs², $\simeq 10\%$ longer than the transform limit of 160 fs. It is therefore necessary to compensate for the effects of GVD in the local oscillator field so as to maintain the heterodyne beat signal predicted by equation 5.23. Among others, Treacy et al [37] showed that the second order spectral phase shift due to GVD could be compensated for using a pair of diffraction gratings, as described in section 2.4.2. A second grating compressor, similar to the design of that used to compress the optical pulse used to generate the terahertz radiation, was therefore used to compensate for the effects of GVD

5.3. Effect of Spectral Phase on Heterodyne Beat Signal

in the local oscillator pulse. Utilizing such an arrangement, it is possible to minimise the signal reduction as a result of GVD in the LO pulse, and it is anticipated that, providing careful attention is paid to compensation of GVD, TOD will have the greater effect on signal degradation.

In contrast, the effect of a spectral phase profile that is cubic in optical frequency, as for third order dispersion (TOD) is observed to have a more modest effect. The signal remains within 50 % of the expected maximum (obtained for the initially transform limited pulse duration of 160 fs) for total third order delays of up to $7 \times 10^6 \text{ fs}^3$, or pulse durations up to 500 fs, in the presence of TOD alone. Typical values of the third order dispersion coefficient, β_3 for single mode fibers at 1030 nm are $\simeq 0.05 \times 10^6 \text{ fs}^3/\text{m}$, and hence the LO pulse would have to propagate in an unreasonably large ($\simeq 100 \text{ m}$) amount of such fibre for the heterodyne beat signal to be significantly degraded due to the effects of TOD alone. That TOD has little effect on the calculated signal amplitude may be expected due to the asymmetrical spectral phase profile that results from TOD, giving a flatter spectral phase profile at the central optical frequency than is observed for the GVD case. It is worth noting that techniques have been demonstrated that allow independent compensation of GVD and TOD [39], but the efficiency of these methods is such that the power in the LO pulse is reduced, and overall signal level will decrease. To date, such methods have therefore not been employed in the experimental work discussed here.

In addition to the contribution to the spectral phase due to material and waveguide dispersion, there will be a nonlinear phase shift, owing to the intensity dependence of the material refractive index and the short optical pulses used. As a result of such an optical Kerr effect, it is appropriate to write the refractive index in fused silica fibre as

$$n = n_0 + n_2 I \tag{5.28}$$

where I is the intensity of the beam, n_0 is the material refractive index in the limit of infinitesimal low intensities, and n_2 is the optical Kerr coefficient in units of m^2/W . As a result, the temporal form of the pulse is distorted

5.4. Effect of Phase-matching on the Heterodyne Beat Signal

according to

$$E(z, t) = E_0 e^{i((n+n_2)\frac{c\varepsilon}{2}|E_0|^2)kz - \omega t}. \quad (5.29)$$

Wise et al. [63] showed that, for typical fibre lasers of the design used here, a nonlinear phase shift of the order of π leads to significant spectral distortion of the optical pulse, in the form of increased energy in the spectral wings. The resulting non-uniform spectral phase profile significantly limits one's ability to re-compress the pulse using a grating compressor. That we do not observe such spectral distortion serves to verify that an upper bound of the peak nonlinear phase shift of π is appropriate for this discussion. In order to calculate the effect of such a nonlinear phase shift on the signal magnitude predicted by equation 5.23, a phase shift proportional to the instantaneous intensity of the Sech² pulse envelope is applied in the time domain, before Fourier transforming back to the Fourier domain to calculate the new spectral phase of each frequency element. Upon substituting the resulting spectral phase profile into equation 5.23 we see that the heterodyne beat signal remains within 50% of the predicted peak value for total nonlinear phase shifts of $\simeq \pi$. Such a nonlinear phase shift would result in optical pulses many times longer in duration than the predicted transform limit, [91] and may be avoided using standard techniques of chirped pulse amplification [92]. We therefore do not expect a significant reduction in the heterodyne beat signal resulting from the nonlinear phase shift of the optical pulse.

5.4 Effect of Phase-matching on the Heterodyne Beat Signal

In addition to a variation in signal strength with the spectral phase of the LO comb, equation 5.23 shows that there is a dependence of the signal strength on the wavevector mismatch of the terahertz comb line and the optical comb line with which it mixes to produce the A-EOS sideband. In order to study the effect of the phase-matching term of equation 5.23, we

5.4. Effect of Phase-matching on the Heterodyne Beat Signal

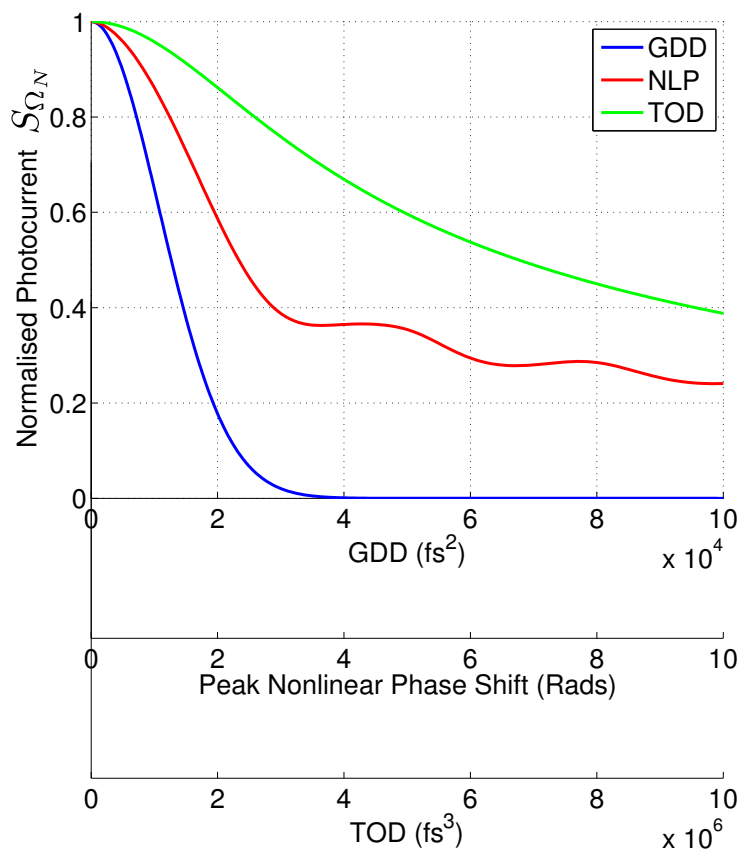


Figure 5.4: Effect of various spectral phase contributions on the expected signal magnitude predicted by equation 5.23, for the local oscillator described in section 2.4. the input spectral bandwidth is 6.9 nm at a central wavelength of 1029 nm, giving a transform limited sech^2 pulse duration of 160 fs.

5.4. Effect of Phase-matching on the Heterodyne Beat Signal

assume the spectral phase of the LO FFC to be flat, and compute the dependence on the wavevector mismatch, Δk_+ and Δk_- of the total SFG and DFG contributions respectively. Figure 5.5 shows the spectral phase and amplitudes of the polarization sidebands written onto the LO FFC, as a function of the optical wavelength. The nonlinear crystal used for detection is ZnTe, with complex refractive index data taken from [93].

For frequencies greater (shorter wavelengths) than the central frequency of the LO FFC, the A-EOS sidebands are produced mainly via the SFG process, due to the larger amplitude of the LO comb elements involved. Likewise, at frequencies lower (longer wavelengths) than the central frequency of the LO FFC, the A-EOS sidebands are dominated by the DFG process. For this reason, the spectral phase of the A-EOS sidebands follows that calculated via the SFG term of equation 5.23 at shorter wavelengths, and that of the DFG term at longer wavelengths.

For a ZnTe crystal of length 0.4 mm, it is seen that the phases of the LO sidebands vary by $\lesssim \frac{\pi}{2}$ across the optical bandwidth of the LO FFC. The rf photocurrents produced by the beating of each LO sideband with its nearest-neighbor LO FFC element therefore also display minimal variation in phase, giving no degradation of either the SFG or DFG contributions to the rf signal. Further, note that the average phases of the SFG and DFG sidebands differ by less than $\frac{\pi}{2}$ such that the contributions to the heterodyne beat from the SFG and DFG sidebands add in phase. Under these conditions, the phase-matching is therefore optimal.

In contrast to figure 5.5, extending the nonlinear crystal to 0.8 mm, as shown in figure 5.6, produces an increased difference in the average spectral phase of the SFG and DFG A-EOS sidebands. This is due to the increased phase contribution of the wavevector mismatch term in equation 5.23, giving a greater phase difference between the SFG and DFG components. The LO sidebands therefore transition in phase from that of the SFG terms at short wavelengths, to that of the DFG terms at longer wavelengths. When the contribution of the entire LO spectrum to the rf heterodyne beat is calculated, the opposing phases of these sidebands gives partial cancellation of the rf photocurrent at $\Omega_N \frac{\Delta f_r}{f_r}$.

5.4. Effect of Phase-matching on the Heterodyne Beat Signal

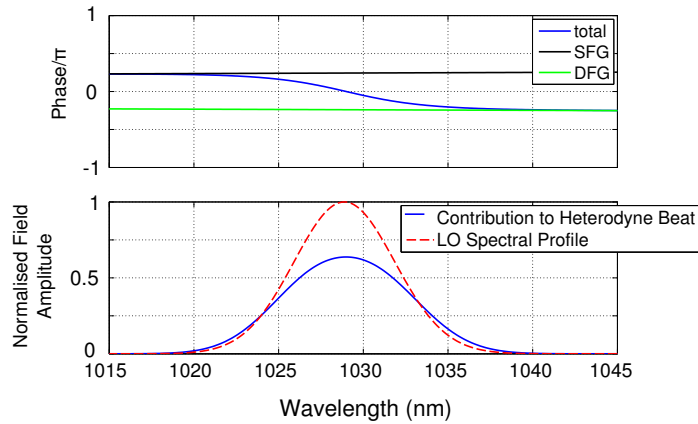


Figure 5.5: Variation of phase (top) and amplitude (bottom) of A-EOS sidebands as a function of optical wavelength for a ZnTe detection crystal of 0.4 mm length. The spectral phase is shown for the sidebands produced through the SFG and DFG processes, as well as the sum of both, weighted by the amplitude contribution predicted by equation 5.23.

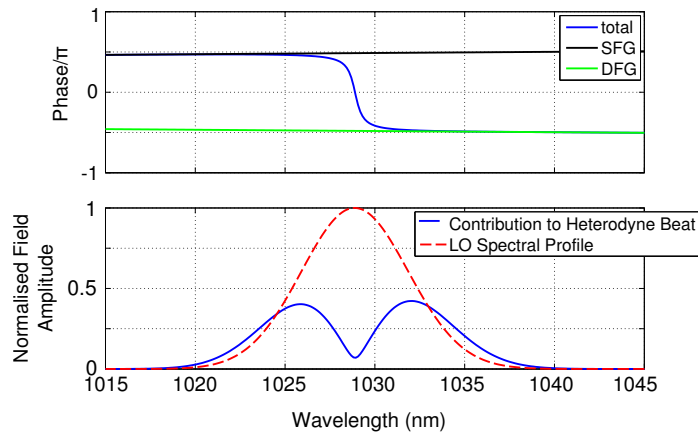


Figure 5.6: Variation of phase (top) and amplitude (bottom) of A-EOS sidebands as a function of optical wavelength for a ZnTe detection crystal of 0.8 mm length. Compared to that of figure 5.5, the difference in phase between the SFG and DFG A-EOS sidebands at similar wavelengths leads to partial cancellation of the heterodyne beat signal. The amplitude of the contribution to the heterodyne beat is normalised with respect to that in figure 5.5.

5.4. Effect of Phase-matching on the Heterodyne Beat Signal

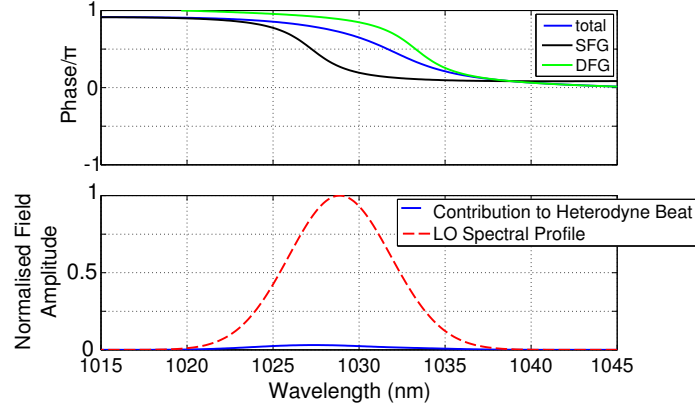


Figure 5.7: Variation of phase (top) and amplitude (bottom) of A-EOS sidebands as a function of optical wavelength for a ZnTe detection crystal of 1.6 mm length. With the longer crystal, the A-EOS sidebands themselves are reduced in amplitude due to the wavevector mismatch between the optical LO and THz comb elements. Again, the amplitude of the contribution to the heterodyne beat is normalised with respect to that in figure 5.5.

Further increasing the crystal length varies the expected signal in a periodic manner similar to that observed in other nonlinear optical processes, as shown in figure 5.8. We see, for example, that a crystal length of 0.4 mm is the optimum choice for the experimental conditions shown, whilst a crystal length of 0.8 mm produces SFG and DFG terms that are nearly opposite in phase, giving near total cancellation of the heterodyne beat signal, as illustrated in figure 5.6. It should be noted that, for the SFG and DFG processes individually, one calculates a coherence length of 1.6 mm in ZnTe for these frequency conditions, due to dephasing of the optical and THz fields, as shown in figure 5.7. It is the dephasing of the SFG and DFG components with respect to each other that reduces the effective coherence length for the heterodyne beating process responsible for the mapping of the THz FC to the rf frequency range.

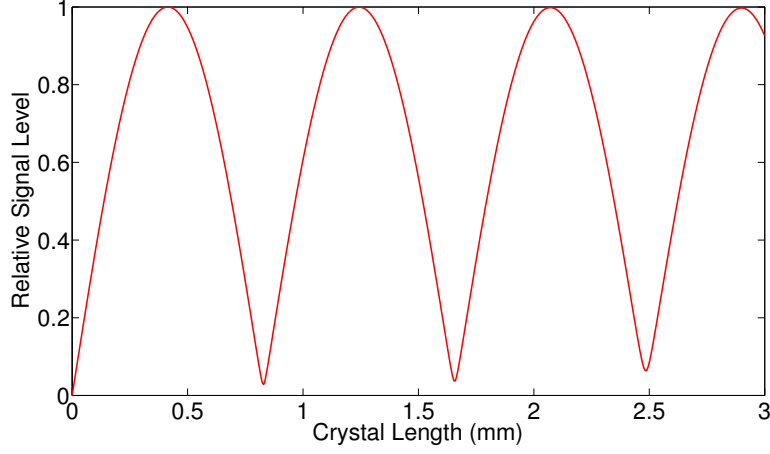


Figure 5.8: Calculated heterodyne beat signal for a THz frequency of 0.85 THz, as a function of nonlinear crystal length for a ZnTe detection crystal, and an LO FFC of 7 nm bandwidth, centred at 1030 nm.

5.5 Bandwidth and Choice of Detuning

As mentioned previously, in order that the bands of rf heterodyne beats do not overlap, it is necessary that $N\Delta f_{rep} \ll \frac{f_{rep}}{2}$. This places restrictions on the useful frequency bandwidth of the terahertz spectrometer, and raises consideration for laser design and data acquisition. For a given system design, the maximum terahertz frequency that can be measured is given by

$$\Omega_N \ll 2\pi \frac{f_{rep}^2}{2\Delta f_{rep}}. \quad (5.30)$$

Figure 5.9 shows the maximum terahertz frequency one can hope to resolve for realistic values of pulse repetition and detuning frequencies. The choice of repetition rate detuning (Δf_{rep}) sets an upper limit on the resolution bandwidth required to resolve distinct spectral elements in the rf frequency range, which in turn sets a lower limit on the required acquisition time, t_{acq} as $t_{acq} \simeq \frac{1}{RBW}$. Again, figure 5.9 shows that t_{acq} can vary from 0.1 to 250ms for reasonable performance parameters. A larger detuning allows for shorter acquisition times but limits the maximum frequency that can be measured,

5.5. Bandwidth and Choice of Detuning

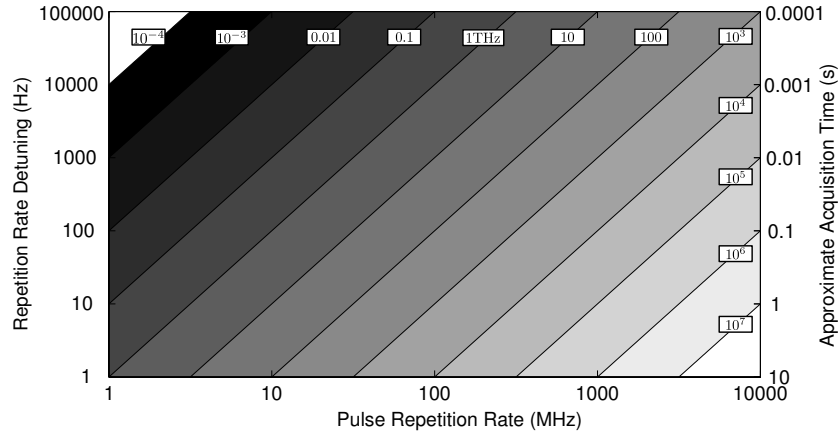


Figure 5.9: Map of the expected bandwidth performance one can reasonably expect from the terahertz heterodyne spectrometer system for given constraints in oscillator design and acquisition methods. The maximum terahertz frequency one can hope to measure before the heterodyne beats overlap at $\frac{f_{rep}}{2}$ is labelled in units of terahertz on the contour lines. Note that, for a laser pulse repetition rate of 100 MHz, and a reasonable detuning of 1 kHz, one can expect a terahertz bandwidth of >10 THz, with data acquisition times $\simeq 10$ ms.

similar to the constraints of a conventional Fourier transform spectrum analyser. Conversely, smaller detunings allow greater terahertz bandwidths to be resolved, but data must be acquired over longer time intervals, and increased constraints are placed on the stability of the relative pulse repetition rates of the optical combs. From figure 5.9, it is seen that very respectable performance can be obtained for realistic design characteristics. For example, for a laser pulse repetition rate of 100 MHz, and a reasonable detuning of 1 kHz, one can expect a terahertz bandwidth of $\gg 10$ THz, with data acquisition times $\simeq 10$ ms. Further increases in the terahertz bandwidth can be obtained by going to higher repetition rate oscillators, as was noted in [83].

5.6 Signal to Noise Scaling

One final further aspect of this detection scheme is worthy of consideration. We note from equation 5.23 that the measured photocurrent is proportional to the square of the amplitude of the LO field, in contrast to conventional heterodyne detection where the photocurrent scales linearly with the LO field. This difference arises due to the LO FFC being involved twice in the beating process. Once to generate the phase modulation sidebands onto the LO FFC, and once in a beating process with these modulation sidebands to produce the rf heterodyne beat, as shown in figure 5.3. The power associated with this signal photocurrent then scales as

$$P_S \propto \langle i_S^2 \rangle \propto P_{THz} P_{LO}^2, \quad (5.31)$$

where $P_{THz} \propto A_{THz}^2$, $P_{LO} \propto A_{LO}^2$, and i_S is the signal photocurrent. The shot noise current, $\langle i_N \rangle$ associated with i_S is described by

$$\langle i_N \rangle = \sqrt{2ei_S \Delta f}, \quad (5.32)$$

where Δf is the bandwidth of the measurement, and e is the electronic charge. The signal to noise power ratio is then defined as

$$\frac{S}{N} = \frac{\langle i_S^2 \rangle}{\langle i_N^2 \rangle} \propto \sqrt{P_{THz} P_{LO}}. \quad (5.33)$$

Whilst the increase in shot-noise-limited signal to noise ratio increases with the square root of the power in the terahertz field, as in the case for both heterodyne detection of a weak optical field, and direct detection of an optical field, the increase in signal to noise ratio with power in the LO field is perhaps less expected. In conventional heterodyne detection, where the signal photocurrent scales linearly with the LO oscillator electric field, it is common to increase the LO power until one reaches the shot-noise limit, where the shot-noise power dominates above all other noise sources. At this point, further increases in LO power produce no benefit as the noise power amplitude increases with the signal amplitude. However, in the heterodyne

5.6. *Signal to Noise Scaling*

detection system here, the additional beating process means that, whilst the shot noise power level scales with the local oscillator power, the signal level will scale with the square of the local oscillator power, providing a potentially large increase in the signal to noise power ratio.

Chapter 6

Experimental Demonstration of Dual-comb Terahertz Spectroscopy

6.1 Coupling of Detuned Local Oscillator Pulse

In Chapter 4 we demonstrated a conventional, single-comb terahertz time-domain spectrometer (SC THz-TDS). We established the spectral content of the terahertz field being generated in the gallium phosphide waveguide. The effectiveness of the electro-optic sampling geometry is seen from the detection noise level of $\simeq 20\text{dB}$ in the scans of figure 4.5. We now move on to a discussion of the experimental efforts to detect this field using the dual-comb detection scheme outlined in Chapter 5.

The optical probe beam of Chapter 4 was replaced with the pulsetrain of a second mode-locked ytterbium-doped-fibre laser, henceforth the local oscillator comb (LO FFC). The $\simeq 200\text{ mW}$ output of the laser in figure 2.10b) was compressed to 250 fs pulse duration using the technique described in section 2.4.2. The polarisation of this beam was then adjusted to match that of the sampling beam found to give the maximum signal magnitude in the conventional, single-comb, time domain spectroscopy case using a half-wave plate. The LO FFC was coupled into the experimental arrangement as shown in figure 6.1 using a switchable mirror, such that the existing beam alignment was unperturbed. In this way, the LO FFC was coaxial with the sampling pulse used in the single-comb THz-TDS experiment of section 4. Alignment of the LO FFC pulse with the previous sampling pulse

was verified using mechanical apertures, and a CCD camera placed at the location of the nonlinear detection crystal. The LO FFC beam was focussed to a spot size of $50\mu\text{m}$ with a Rayleigh range in excess of 5 mm, verified using the technique described in section 3.5.2, such that the optical spot size remained smaller than that of the terahertz spot size throughout the interaction length of the crystal. In this way, the entire optical pulse is influenced by the change in refractive index due to the terahertz pulse. Due primarily to losses in the grating compressor and in the reflectivity of the pellicle beam splitter, the LO power incident on the nonlinear detection crystal was limited to 30 mW.

6.2 Controlling The Laser Repetition Rates

6.2.1 RF Locking Scheme

In order to detect the heterodyne comb predicted in section 5, it is necessary that each rf comb line have a width far less than the spacing of the rf comb lines, so as to ensure the heterodyne comb itself is not obscured by the widths of the individual comb lines. As the rf comb is produced by mixing of the optical LO FFC and terahertz combs, it is necessary to stabilise the relative frequencies of the LO FFC and the optical comb used to produce the THz FC. In order to do this, the difference in pulse repetition rate of the two laser oscillators of figure 2.10 is locked to a reference oscillator using the system of rf electronics shown in figure 6.2.

It is important to note the fact that the heterodyne beat between the LO FFC and the THz FFC is produced by the mixing of many optical and terahertz comb lines, centred at $\simeq 300$ THz and 1 THz respectively. The respective combs are therefore centred at approximately the 3×10^6 and 1×10^4 th harmonics of the $\simeq 100$ MHz repetition rate. As the rf heterodyne beat results from mixing of THz FC and LO FFC elements at $\simeq 1$ THz and 300 THz respectively, it is drifts in frequency between these comb elements that we wish to minimise in designing the locking scheme. Whilst locking of dual-combs at optical frequencies has been demonstrated [94], the tech-

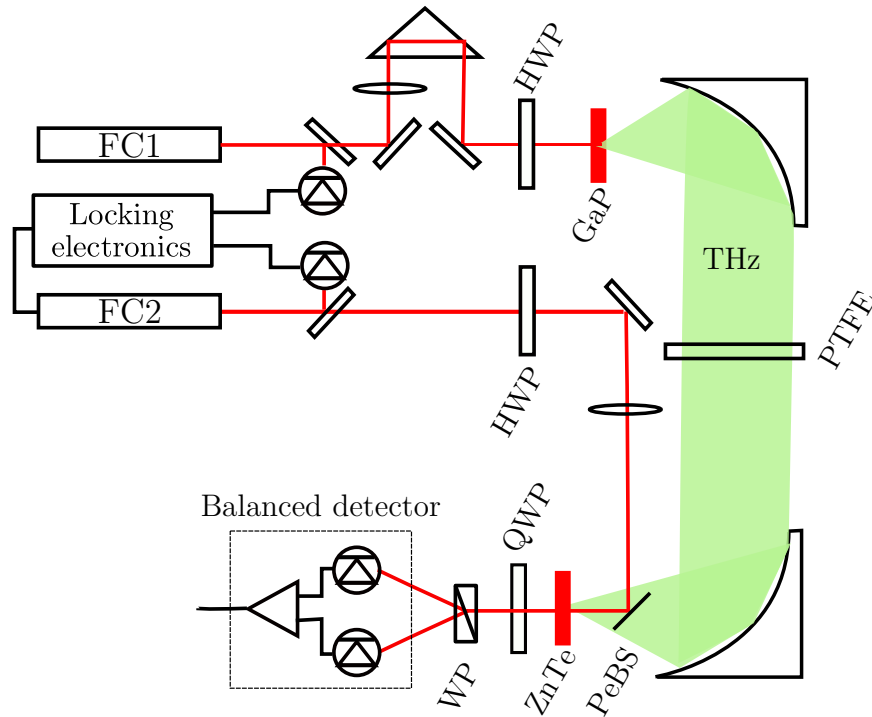


Figure 6.1: Experimental arrangement of the dual-comb terahertz spectrometer. In contrast to figure 4.1 the apparatus replaces the probe pulse with that from a second optical frequency comb (FC2), coupled into the experiment using a switchable mirror (SM) so as not to perturb the existing beam alignment. This second comb is detuned in repetition rate such that the delay between pulses from FC1 and FC2 varies in time. In this way the need to sweep the mechanical delay line is eliminated (the driving optical pulse still passes through the retro-reflector used to create the delay for reasons of alignment). As in figure 4.1, the sampling pulse is coupled into the detection crystal using a pellicle beam splitter (PeBS). Waveplates are used to optimise the polarisation states of the various beams so as to utilise the largest nonlinear coefficients, and a piece of PTFE is used to block the residual optical beam after the generating crystal.

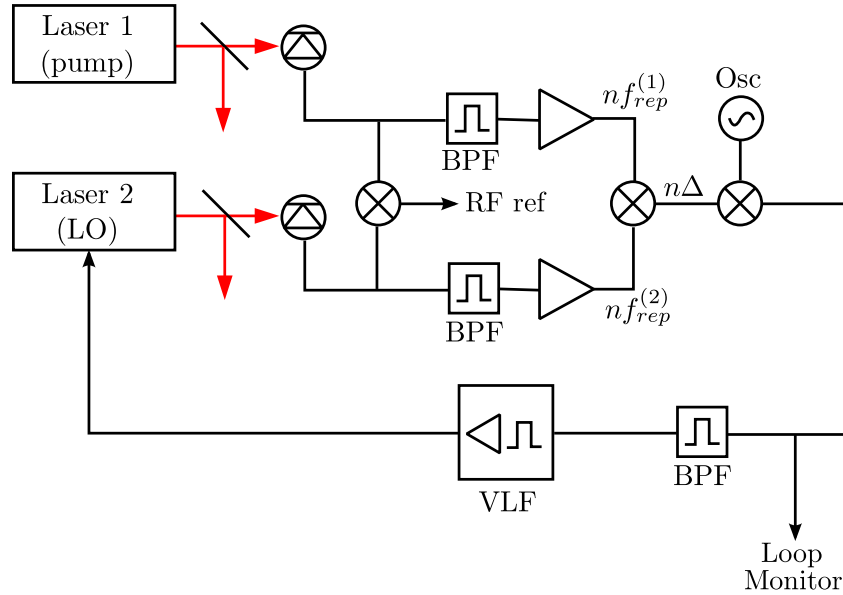


Figure 6.2: Schematic of the rf locking scheme used to control the pulse repetition rates of the two lasers. Optical paths (in fibre) in red, electrical paths in black. A 10% portion of each laser output is picked off using a fibre splitter. A fibre coupled fast (≈ 10 GHz) photodiode is used to detect the pulse train from each laser. Each resulting photocurrent signal is first filtered (BPF) at the n th harmonic of the nominal repetition rate of 104 MHz and amplified prior to combining the two signals in a double balanced mixer. The resulting mixer output is subsequently mixed with a reference oscillator (Osc) at $n\Delta$. Harmonics of the mixer output are removed using a third tuneable BPF before being fed to a variable loop filter (VLF). The VLF is essentially a two-pole device enabling tuning of the low frequency gain as well as the poles of each filter stage. The output of the filter is amplified and used to control the intracavity piezoelectric actuator in the laser used as the local oscillator, or probe laser. A signal (RF ref) at Δf_{rep} is provided for reference and triggering purposes. Similarly, a monitor of the residual noise on the error signal used to control the intracavity PZT is provided prior to the BPF and VLF stages for the purpose of system characterisation.

nique requires additional reference cavities and single mode lasers, greatly increasing the experimental complexity. Instead, it is common practice to lock the pulse repetition rates of lasers of this type by detecting harmonics of the repetition rate at more readily accessible rf frequencies.

In the work presented here, we lock at the 37th harmonic of the nominal pulse repetition rate, at a frequency of $\simeq 3.7$ GHz. Whilst we do not expect comparable performance to the optical locking techniques cited earlier, locking at a higher order harmonic of the repetition rate serves to reduce the broadening of the optical comb lines of concern due to residual jitter at the lock frequency. To understand this, consider the case where one locks the difference in fundamental of the laser pulse repetition rates, f_{rep} , such that the relative broadening of the repetition rate difference, the detuning, is $\Delta\nu$. In this case, the N th harmonic is broadened by an amount $N\Delta\nu$. In contrast, if the lock is performed at some higher harmonic of the repetition rate, at nf_{rep} , say, then the difference frequency of the beat between the n th harmonics is broadened by $\Delta\nu$, and the optical frequency at Nf_{rep} is broadened by an amount $\frac{N}{n}\Delta\nu$. It is therefore desirable to lock at the highest harmonic, n , of the repetition rate possible. The previously cited work of [94] benefits from locking at optical frequencies, where $n \sim 3 \times 10^6$. For the purposes of this thesis, the two laser combs were locked at the more readily accessible rf frequency of the 37th harmonic of the laser pulse repetition rate at 3.7 GHz. That is to say that $n = 37$ in figure 6.2. Efforts to optimise the locking scheme, so as to reduce the expected broadening of the rf heterodyne beat as well as determine the extent to which the performance of our locking scheme is expected to broaden the heterodyne comb, are examined in section 6.3.

6.2.2 Component Testing and Characterisation

For the purposes of the following discussion, we refer to the first mixing stage, and any preceding components as ‘high frequency’ rf, operating at $nf_{rep} \simeq 3.7$ GHz, and the following components as ‘low frequency’ rf, operating at $n\Delta \sim$ kHz frequencies. In order to reduce broadening of the

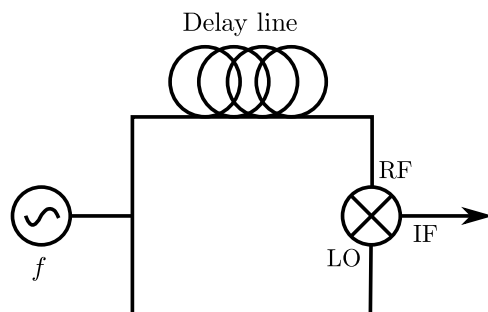


Figure 6.3: Arrangement for measuring of the noise floor of the available low frequency mixers. The frequency, f of an oscillator is varied such that the two signals combine at the mixer in quadrature for the (non-variable) delay, giving zero dc output. The mixer output is then observed on a spectrum analyser.

heterodyne beat frequencies due to lock instabilities, it is desirable that the noise floor of each component contributes as little as possible to the repetition rate detuning of the two combs. To this end, the noise floor of three available low frequency mixers was measured using the setup shown in figure 6.3, with the results shown in figure 6.4. It is seen that the Anzac models display both a lower noise floor, and reduced susceptibility to line harmonics, especially at higher frequencies. Where possible then, these mixers were favoured over the Maccorm model also tested.

A similar study was performed for the available high frequency mixers. Due to the difficulty in providing a reference signal at the necessary 3.7 GHz, the locking electronics were assembled and tested as shown in figure 6.2 with the various mixers in place. The residual noise on the control signal used to drive the piezo-electric actuator in the laser cavity was then measured prior to the band-pass filtering stage, as indicated in figure 6.2. The residual noise as a function of frequency for the various mixers is shown in figure 6.5. Note that this configuration actually compares the 37th harmonic of the repetition rate difference to the oscillator frequency, which is set to the 37th harmonic of the desired repetition rate difference. From figure 6.5, it is seen that the servo loop is effective at reducing noise on the control

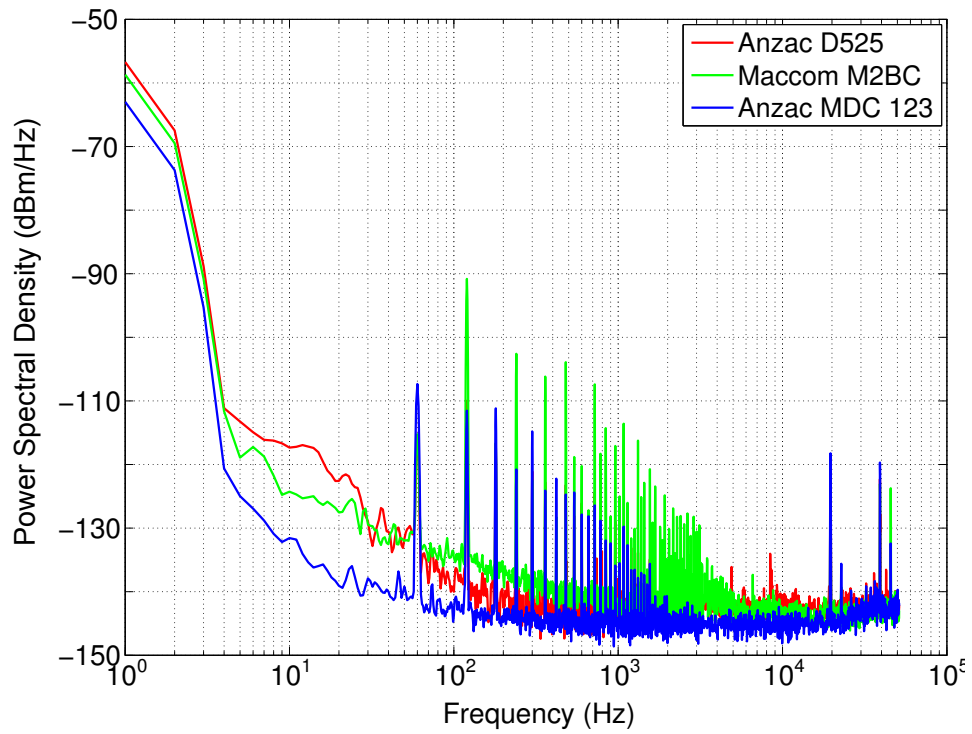


Figure 6.4: Measured noise floors for the three available low frequency mixers. Strong line harmonics remain, despite significant efforts to reduce these.

6.2. Controlling The Laser Repetition Rates

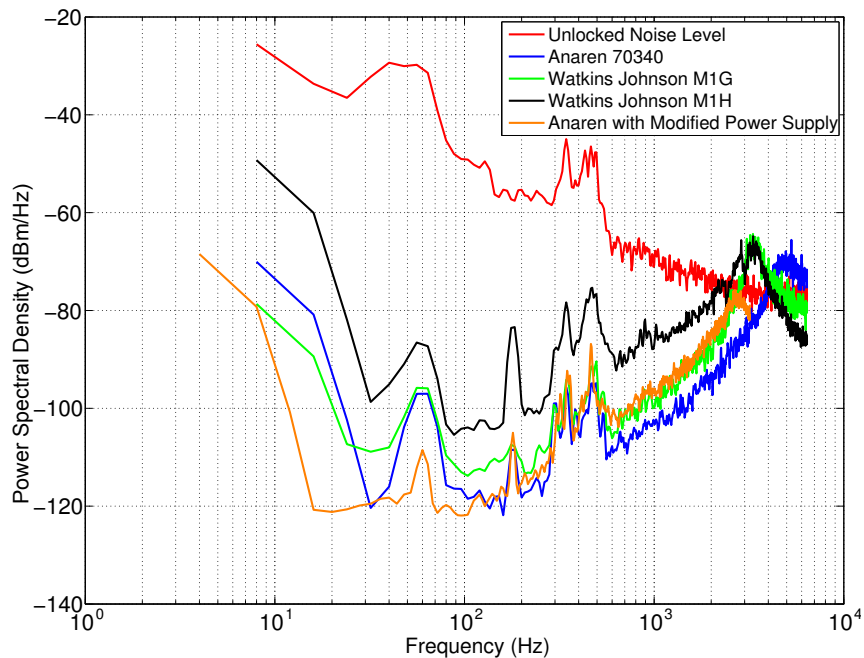


Figure 6.5: Spectrum of the residual noise on the error signal for the range of high frequency mixers available, together with a reference trace showing the noise level in the absence of any precise locking scheme. For this reference trace, the dc bias to the oscillator cavity PZT was manually controlled so as to maintain the difference in laser repetition rates in ‘close’ lock to the oscillator frequency, but no servo gain was employed. Data is also shown for the Anaren mixer following work to isolate ground loops and provide cleaner power supplies for the servo electronics and rf amplifiers. In general, the servo loop is seen to reduce the level of noise on the control signal for frequencies out to around 3 kHz, where the phase response of the servo loop is such that further increases in gain write on additional noise to the control signal, and the residual noise rises above that in the unlocked case.

signal out to frequencies around 3 kHz, where the phase response of the loop is such that increased loop gain writes additional noise onto the control signal. This results in the characteristic "servo bump" [95] at 3 kHz. The Anaren mixer shows the lowest residual noise floor. Further, the control signal displays residual line harmonics at 60 Hz and 180 Hz, regardless of the mixer used. Considerable effort was therefore put into modifying the power supply circuitry for both the servo electronics, and for the rf amplifiers used in the servo loop. In particular, all required supply voltages were derived from linear voltage regulators, and ground loops removed wherever possible. Figure 6.5 shows the results of this work for the Anaren mixer, with the reduction in 60 Hz noise clearly visible.

6.3 Cross Correlation of Laser Pulses to Verify Timing Jitter

Having taken steps to optimise the locking used to control the pulse repetition rate offset of the two laser oscillators, we now seek to verify the performance of this locking scheme by performing a measurement derived from the optical output of the lasers, independent of the control circuitry under study. This was done using a method similar to that documented in [86]. A cross-correlation measurement of the two laser pulses was acquired using non-collinear sum frequency generation in a β -Barium Borate (BBO) crystal as per the experimental arrangement shown in figure 6.7. The repetition rate difference of the two lasers is locked at Δf_{rep} . This causes the delay between the pulses, $\tau(t)$, to vary in time as shown in figure 6.6. If the two lasers have pulse repetition rates $f_{rep,1}$ and $f_{rep,2} = f_{rep,1} + \Delta f_{rep}$, and the delay between pulses is zero at time $t = 0$, then the delay can be written

6.3. Cross Correlation of Laser Pulses to Verify Timing Jitter

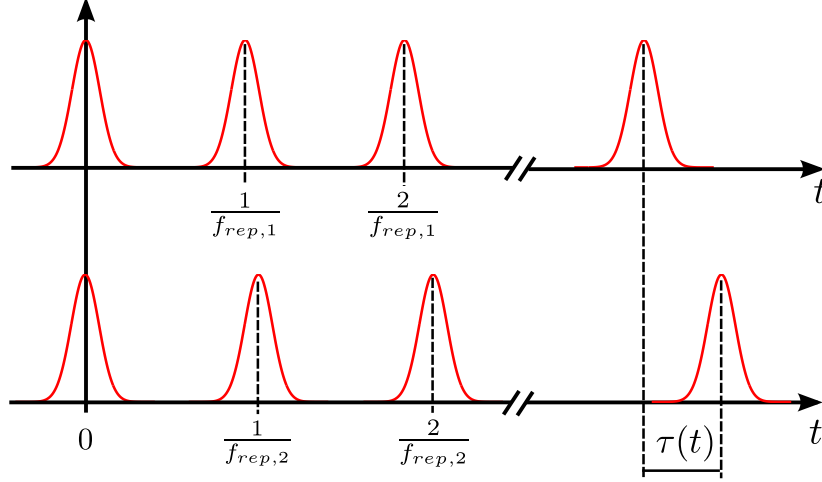


Figure 6.6: Pulse trains from two lasers, with pulse repetition rates $f_{rep,1}$ and $f_{rep,2} = f_{rep,1} + \Delta f_{rep}$. The delay $\tau(t)$ between pulses varies as $\tau(t) = t \frac{\Delta f_{rep}}{f_{rep}}$ where $t = 0$ corresponds to the time at which the pulses overlap perfectly.

as

$$\begin{aligned}
 \tau(t) &= t f_{rep,1} \left(\frac{1}{f_{rep,1}} - \frac{1}{f_{rep,2}} \right) \\
 &= t \left(\frac{\Delta f_{rep}}{f_{rep,1} + \Delta f_{rep}} \right) \\
 &\simeq t \frac{\Delta f_{rep}}{f_{rep}} \tag{6.1}
 \end{aligned}$$

Any fluctuations in the pulse repetition rate difference of the two lasers will result in fluctuations on the pulse delay, τ . In order to measure the fluctuations in τ , we provide an rf trigger at the average repetition rate difference by virtue of the port labelled ‘RF ref’ in figure 6.2 in order to trigger a 500 MHz digital storage oscilloscope. Due to the residual jitter in τ , averaging over many traces appears to broaden the measured pulse. We therefore average over a sufficiently long time period such that the averaged signal does not appear to broaden any further, at which point the duration

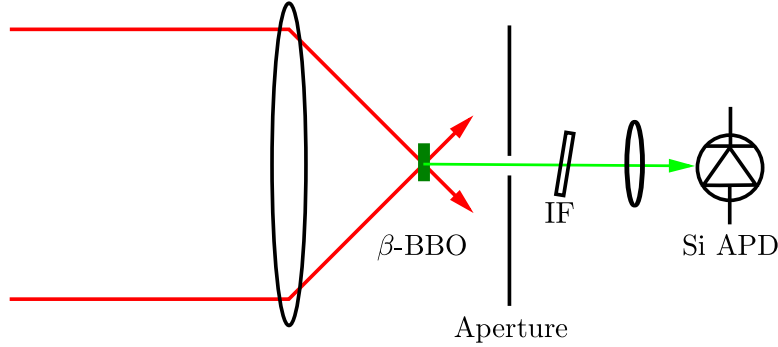


Figure 6.7: Experimental arrangement for the cross-correlation measurement. The two optical beams are focussed into a β -BBO crystal using an 80 mm focal length lens. The generated noncolinear sum frequency radiation is focused through an aperture onto a silicon avalanche photodiode (Si APD). In order to reduce the residual optical power reaching the photodiode an interference filter was used, angle tuned to the wavelength of the second harmonic light at 515 nm. Phase-matching in the BBO crystal is type II angle-tuned.

of the pulse represents the overall time resolution of this setup.

A typical trace where the repetition rate detuning is locked to 400 Hz is shown in figure 6.8. The data shown is an average of 128 measurements over an acquisition time of $\simeq 10$ ms, limited by the averaging function of the sampling oscilloscope. The observed signal has the form of a 100 MHz pulse train (governed by the nominal repetition rates of the lasers) modulated by an envelope with pulse full width half-maximum duration $\simeq 100$ ns and modulation frequency determined by the detuning, $\Delta f_{rep} = 400$ Hz. From the time axis, one calculates the delay between the two optical pulses according to $\tau(t) = t \frac{\Delta f_{rep}}{f_{rep}}$, from which one obtains a width of the averaged cross-correlation signal of $\simeq 400$ fs. The width of this envelope did not increase with increased averaging time, thus the residual jitter in the time base provided by this locking scheme is 400 fs. Such an envelope deconvolves to an actual sech^2 pulse width of 260 fs, which is comparable to the original optical pulse width, indicating minimal residual timing jitter due

6.3. Cross Correlation of Laser Pulses to Verify Timing Jitter

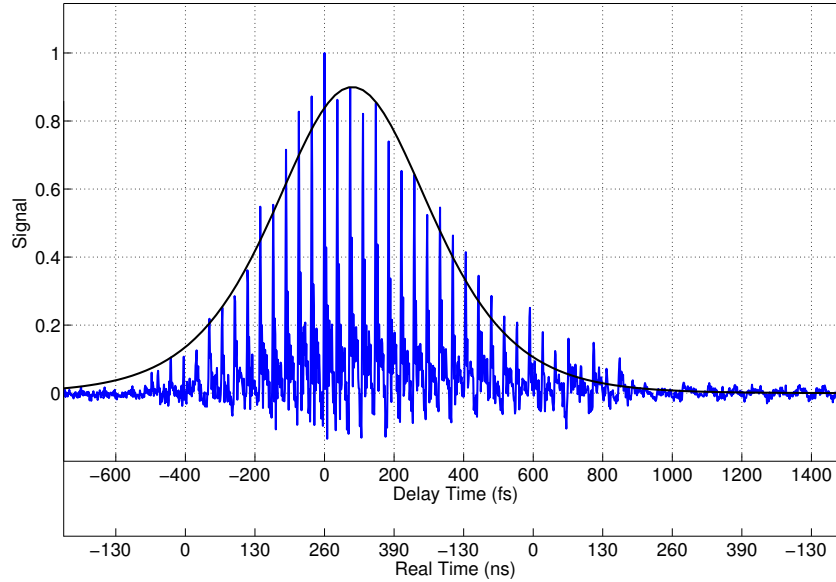


Figure 6.8: Blue: Cross-correlation trace of the femtosecond optical combs in β -BBO with the repetition rate detuning set to 400 Hz. Time axes are shown both for the real time (lower) and scaled by a factor $\frac{\Delta f_{rep}}{f_{rep}}$ to give the delay time. Black: Overlay of the sech^2 envelope corresponding to the cross-correlation signal expected from pulse widths of 260 fs.

to the phase noise of the electronic components used. Further verification of the lock performance was performed by reducing the repetition rate detuning to 15 Hz, and analysing the resulting frequency modulations in the cross-correlation signal using an rf spectrum analyser. The results are shown in figure 6.9. It is seen that the modulation of the cross-correlation signal remains resolvable for even such small detunings. Indeed, the broadening observed is comparable to that expected due to the limited 2 Hz resolution bandwidth of the instrument. The conclusion is therefore drawn that the broadening of the heterodyne beat between the two lasers is not so severe so as to prevent detection of the individual comb lines, and the lock is deemed to be working satisfactorily.

6.3. Cross Correlation of Laser Pulses to Verify Timing Jitter

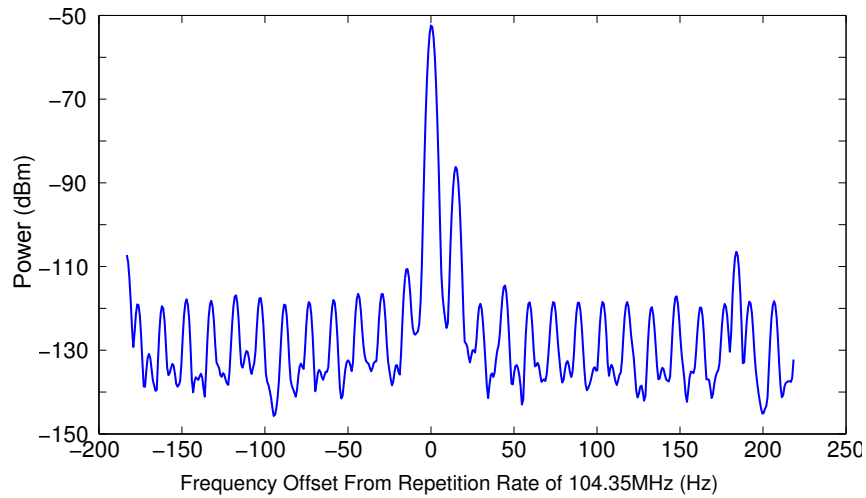


Figure 6.9: RF spectral output for the cross-correlation measurement depicted in figure 6.7. The detuning, Δf_{rep} has been reduced to 15 Hz, whilst the resolution bandwidth of the instrument is set to 2 Hz. The increased sidebands at $\simeq 180$ Hz due to instabilities in the output of the diode used to pump the power amplifier stage remain visible, as discussed in section 2.4.3.

6.4 Schemes for Detection of the Heterodyne Beat

6.4.1 High Gain Balanced Detector With High Extinction of Frequencies Greater than 80 MHz

The first attempt to detect the comb of heterodyne beats between the detuned terahertz comb and the optical local oscillator was performed using a custom designed balanced detector, giving a gain at 100 kHz of 8 V/mA, and a high frequency roll-off of $\simeq 40$ dB/8ve at 80 MHz in order to attenuate the large repetition rate signal at 104 MHz. In addition, a high pass filter of 50 dB/decade at 1 kHz was used to eliminate any dc component arising from slight errors in setting the balancing of the polarisation channels. A schematic of the detector circuit is given in figure A.1 in appendix A. The response of the detector to a balanced input is shown in figure 6.10.

For a terahertz comb and LO comb with repetition rate detuning Δf_{rep} one expects the terahertz frequency at $N(f_{rep} + \Delta f_{rep})$ to be mapped to an rf photocurrent signal of frequency $N\Delta f_{rep}$, as derived in section 5. For a terahertz comb centred at 0.75 THz, as in figure 4.5a, $N = \frac{f_{THz}}{f_{rep}} \simeq 7500$, so, for a typical detuning of 1 kHz, one expects the particular heterodyne beat due to the terahertz frequency at line centre to be at 7.5 MHz. It should, however, be noted that each comb element of the terahertz comb creates its own heterodyne beat, and that therefore there is, as explained in section 5, a comb of rf frequencies separated by Δf_{rep} . This comb extends from dc up to the bandwidth of the terahertz pulse, scaled by a factor $\frac{\Delta f_{rep}}{f_{rep}}$. The balanced detector, in conjunction with additional external filtering if necessary, therefore provides large gain of the frequencies at which we expect to observe the comb of heterodyne beats, whilst simultaneously reducing the rf power at 100 MHz, allowing the gain to be further increased without saturating the power spectrum.

The optical power giving shot-noise limited performance of this detector can be determined from the noise spectra of figure 6.11, which shows the unamplified detector response function for lower frequencies than that of

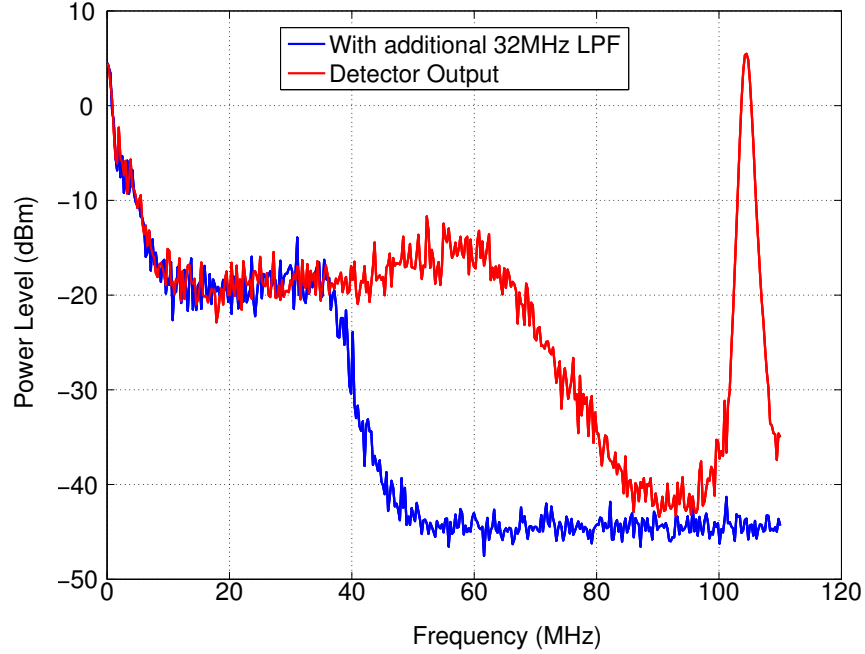


Figure 6.10: Output of the custom-designed balanced detector for a typical balanced input with additional 32dB external amplification. The band-edge is seen to attenuate the 104 MHz repetition rate signal such that the in-band noise-floor is only 25 dB below the 104 MHz peak. If necessary, additional filtering can be employed to further attenuate the repetition rate signal, as in the case shown where an additional 32 MHz low pass filter (LPF) has been used.

figure 6.10. One observes a pass-band noise level of -140 dBm. Compare this to the expected shot noise on the dc photocurrent, i_{DC} produced from the $0.3\mu\text{W}$ of optical power incident on a single channel. Using an on-board gain of 7.3 V/mA, the dc voltage drop across a $50\ \Omega$ load was observed in this case to be 2V, implying a photocurrent of 0.27mA. The shot-noise power associated with such a photocurrent is given by

$$\langle i_N \rangle^2 R = 2ei_{DC}, \quad (6.2)$$

where i_N is the noise current and R is the load. For this case, one obtains

6.4. Schemes for Detection of the Heterodyne Beat

a shot-noise power of $-144 \frac{\text{dBm}}{\text{Hz}}$, in good agreement with the noise floor of figure 6.11. Further, increasing the optical power incident on the detector produced a corresponding increase in the observed noise floor for frequencies within the pass-band. $0.3\mu\text{W}$ is a readily available optical power from the local oscillator, and therefore it is reasonable to expect shot-noise limited performance from this detector. Despite the considerable gain in the

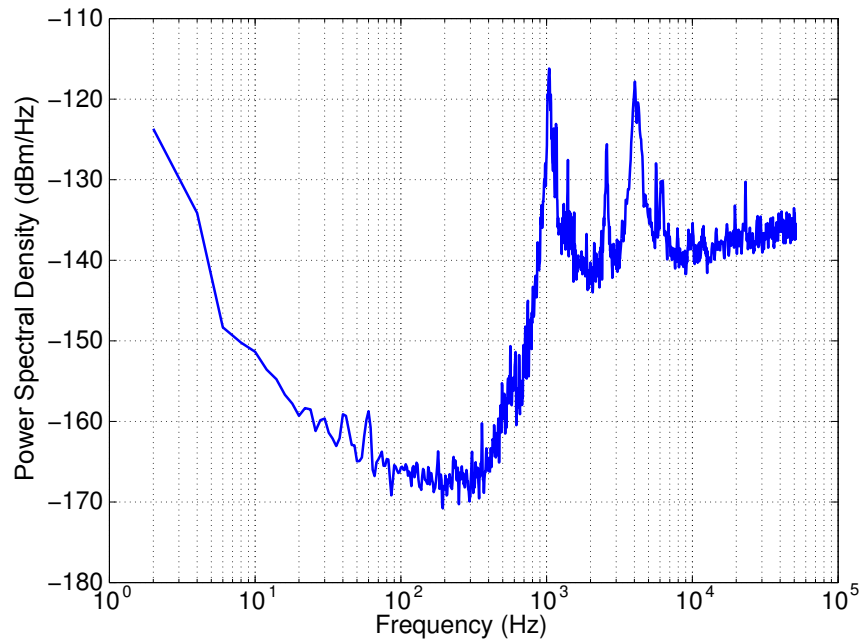


Figure 6.11: Noise spectrum for the high-speed balanced detector used for detection of the heterodyne beat signal. The incident optical power on a single channel in this case was $0.3\mu\text{W}$. The observed noise-floor in the pass-band of -140 dBm corresponds well to the expected shot noise on the observed dc photocurrent of 0.274mA . Note that, also visible, is the roll-off of the high pass filter at 1 kHz .

frequency range expected to contain the comb of heterodyne beat signals, efforts to resolve the predicted rf heterodyne comb at low frequencies using the bandwidth-limited balanced detector were unsuccessful. Whilst the measurement was indeed shot-noise limited, equation 5.33 suggests that, for

this detection scheme, increases in the signal to noise ratio can be expected by increasing the power in the LO field beyond that of the shot-noise-limited case. Unfortunately, further increases in LO power were not possible without adding additional high power amplification stages to the LO laser output, for which resources were not available. In light of this, an alternative detection scheme employing phase-sensitive detection of a single heterodyne comb element was employed. This forms the topic of the following section.

6.4.2 RF Heterodyne Detection Using VCO Reference

With the bandwidth limited balanced detector proving unsuccessful, an attempt was made to increase the signal to noise ratio of the expected rf heterodyne comb by employing a form of rf phase-sensitive detection. To do this, a voltage-controlled reference oscillator was locked to the N th harmonic of the repetition rate detuning using a servo loop in addition to that used to control the repetition rate detuning itself, as shown in figure 6.12. This oscillator signal was then used as the LO input to a double-balanced mixer, with the photodiode signal providing the rf input. In this way, a particular comb element of the rf heterodyne comb described by equation 5.23 is demodulated down to dc frequency. We choose this particular comb element to be near the centre of the predicted rf heterodyne comb so as to maximise the expected signal level.

Recall the rf signal corresponding to a THz FC element at frequency Ω_N varies in time as

$$S_{\Omega_N}(t) \propto A_{THz}(\Omega_N) \exp(-2\pi i N \Delta f_{rep} t), \quad (6.3)$$

where $A_{THz}(\Omega_N)$ is the complex spectral amplitude of the THz FC element at frequency Ω_N . Using the experimental arrangement of figure 6.12, we provide a reference signal at frequency $N\Delta f_{rep} = \frac{\Omega_N}{f_{rep}}$. By mixing this reference signal with the measured photocurrent in a double balanced rf mixer (DBM) the heterodyne beat corresponding to a terahertz comb element N at frequency Ω_N is mapped to dc frequency. Similarly, the heterodyne comb elements adjacent in frequency, corresponding to terahertz comb elements

at

$$\Omega_{N+R} = (N + R)f_{rep}, \quad (6.4)$$

where R is the order of the comb element with respect to the N^{th} element at frequency Ω_N , are mapped to rf frequencies $R\frac{\Delta f_{rep}}{f_{rep}}$. In order to observe the strongest heterodyne beats, we seek to set $\Omega_N = Nf_{rep}$ to the centre of the terahertz spectrum shown in figure 4.5. We then expect to observe a dc signal corresponding to the heterodyne beat at $N\Delta f_{rep}$, and a set of rf comb elements spaced by the repetition rate detuning, Δf_{rep} arising from the terahertz comb lines at Ω_{N+R} . A voltage controlled oscillator (VCO) was used to provide the necessary reference frequency. Component availability stipulated that the output frequency of the VCO, f_{VCO} was nominally 80 MHz, with a tuning range of ± 10 MHz. A frequency pre-scaler (UPB1509GV) was therefore used to divide this by four to obtain a reference at $\simeq 18$ MHz. A further pre-scaler was used to divide the frequency of a portion of this output by a factor of 256, such that a second double-balanced mixer could be used to generate a VCO control signal from comparison with the signal at $37\Delta f_{rep}$, picked off from the servo loop used to control the repetition rate detuning. This required the repetition rate detuning, Δf_{rep} , be set to 1.9 kHz. With this setup, the heterodyne beat mapped to dc corresponds to a terahertz frequency of

$$\Omega_N = 18\text{MHz} \frac{f_{rep}}{\Delta f_{rep}} = 0.9\text{THz}. \quad (6.5)$$

From figure 4.5a, it is seen that this is less than 50% down on the peak of the terahertz emission spectrum produced from the gallium phosphide waveguide. Limited component availability (and, crucially, the requirement that the pre-scalers used can only divide by a power of two) means that it was not possible to get closer to the terahertz band-centre.

In order to control the VCO frequency, an active filter was built consisting of an integrator and low-pass filter stage, a schematic of which is shown in figure 6.13. The poles of the filter were varied to give optimum performance, as determined by figure 6.14.

6.4. Schemes for Detection of the Heterodyne Beat

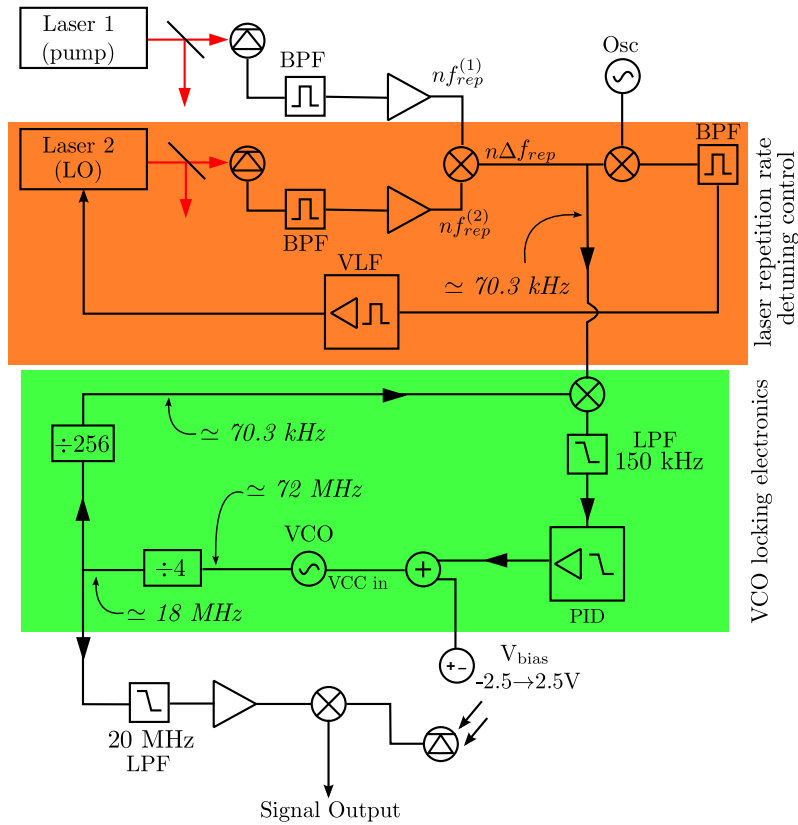


Figure 6.12: Schematic of the rf circuitry used to provide a reference signal at the expected rf heterodyne beat frequency. The output frequency of a voltage-controlled oscillator (VCO) is divided down by a factor of 4 to provide the required reference signal at 18 MHz. A small portion of this 18 MHz signal was then further divided by a factor of 256 so as to enable comparison to a portion of the repetition rate detuning signal at $n\Delta f_{rep}$ (≈ 70.3 kHz for a detuning of 1.9 kHz). The control signal of the VCO, $V_{CC\ in}$, is derived from the IF output of the mixer, using a servo loop, similar to that used to control Δf_{rep} , but using a purpose-built active filter (PID) in place of the loop filter used in the detuning locking case. A manually adjustable bias voltage, V_{bias} is provided for tuning of the VCO frequency, and is added to the control signal using a conventional adder circuit. The VCO output is low pass filtered to remove harmonics and amplified to provide the necessary rf power to be used as the reference in a mixing stage with the optical signal. Measurements were made using both a single fast photodiode configured as per the single-channel detection scheme in 4.3, or from the bandwidth-limited balanced photodiode described in section 6.4.1, configured as per the balanced detection scheme of section 4.3.

6.4. Schemes for Detection of the Heterodyne Beat

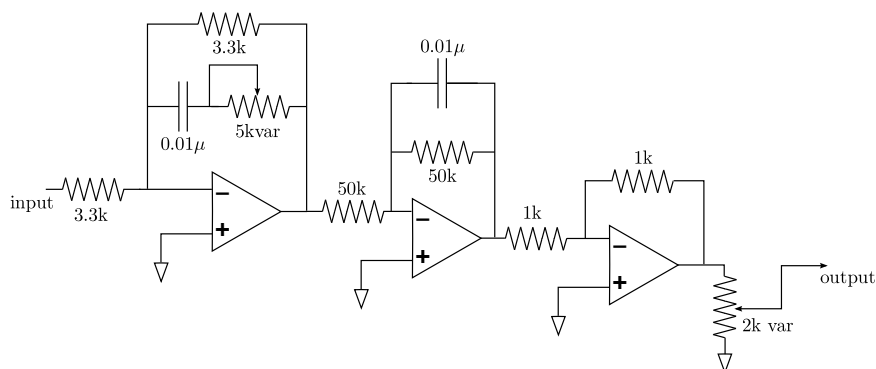


Figure 6.13: Circuit schematic for the active filter used to lock the voltage control oscillator (VCO) to the expected frequency of the heterodyne beat signal predicted by the analysis of Chapter 5. The component values shown were decided upon following analysis of the lock performance, as shown in figure 6.14. As shown, the filter consists of an initial integrator stage, with a pole at approximately 20 kHz, and a second low-pass filter with a pole at 315 Hz. A potentiometer is provided at the final output for varying the overall response.

Figure 6.14 shows the residual noise on the VCO control signal as a function of frequency. Prior to considering the performance of the feedback loop in locking the VCO frequency to that of the laser repetition rate detuning, the ability of the servo loop to lock the VCO frequency to a fixed reference oscillator (Hewlet-Packard model no. 8662A) is characterised by a flat noise floor out to the resonance of the integrator stage at $\simeq 20$ kHz. Whilst it was possible to change the configuration of the filter in figure 6.13 such that the calculated pole of the integrator stage was shifted to $\simeq 80$ kHz, such a broad bandwidth resulted in an unstable lock of the VCO to the reference oscillator, indicating a 180° phase roll-off in the response of other loop components. It should be noted here that identical VCOs are locked to reference frequencies with loop bandwidths approaching 100 kHz in other experiments in our lab. The limitations in bandwidth therefore are not attributed to the VCO itself, but other components in the loop highlighted in green in figure 6.12. In the absence of alternative loop components, the

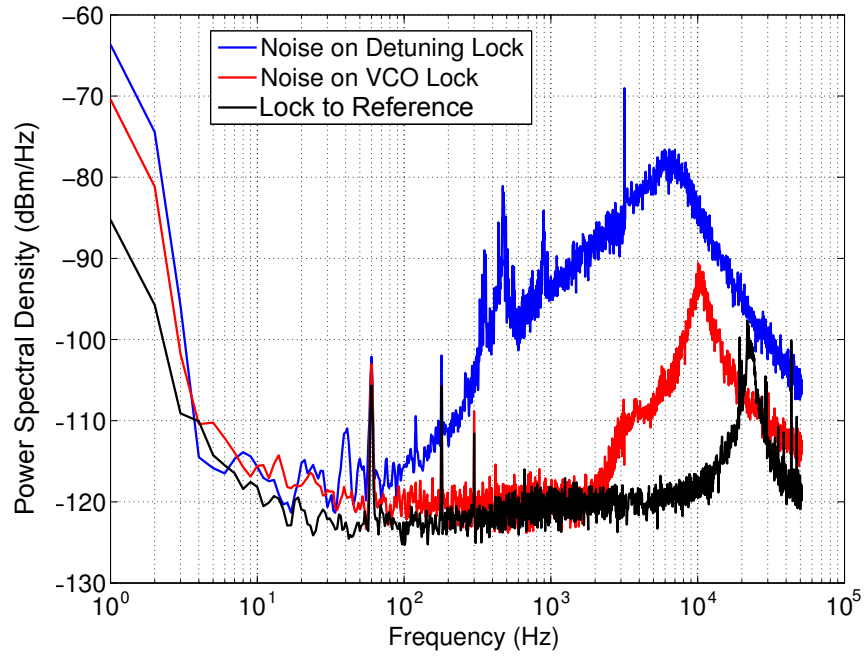


Figure 6.14: Measured residual noise level on the VCO control signal for locking of the VCO to the detuning (in red) and a reference oscillator (in black). The measured noise floor on the laser detuning lock (in blue) is shown for comparison.

6.5. Results and Conclusions from Dual-comb Spectroscopy Measurement

pole of the integrator stage was reduced in frequency so as to reduce the filter gain beyond 20 kHz, rather than thoroughly determine the root cause of this limited locking bandwidth.

Figure 6.14 shows that, when tracking the residual drift in the repetition rate detuning, Δf_{rep} , the loop is able to reduce the residual noise on the VCO control signal to that observed when locking to a reference oscillator for frequencies up to $\simeq 3$ kHz, but that there is an increase in the residual noise on the VCO control signal at $\simeq 6$ kHz, where the resonance of the detuning control loop, as previously observed in figure 6.5, writes additional noise onto the VCO control signal. However, below this resonance, the residual noise of the VCO lock is well below that of the locking signal used to control the repetition rate detuning, indicating that the VCO servo loop is able to tune the VCO frequency sufficiently fast to ‘track’ residual drifts in the detuning out to a bandwidth of $\simeq 6$ kHz.

Attempts to detect the expected rf heterodyne beat with the the described VCO reference signal were made using both the bandwidth-limited balanced detector described previously, and a fast single-channel detector in conjunction with a half wave-plate and crossed polariser, as described in section 4.3. In the latter case, the optical power after the nonlinear detection crystal was attenuated to $\simeq 1 \mu\text{W}$ so as to avoid saturating the on board amplifier circuitry. Neither of these methods proved successful. We therefore dedicate the remainder of this chapter to a discussion of where the current experiment might be improved, and a comparison to other works where appropriate.

6.5 Results and Conclusions from Dual-comb Spectroscopy Measurement

No comb elements were visible in the measured rf spectrum, despite additional amplification of the photodiode signal, such that the shot-noise limited noise floor of the output of the final mixer stage was $\simeq -10$ dBm, well above the total instrument noise level of $\simeq -130$ dBm. The following discussion

6.5. Results and Conclusions from Dual-comb Spectroscopy Measurement

outlines some of the experimental limitations, and, in particular, compares the current work to that of other authors who have been able to observe a beating of the two detuned combs, albeit with differing measurement and data acquisition schemes.

From equation 5.23 one sees that the magnitude of the contribution to the rf photocurrent observed at the heterodyne beat frequency due to a single A EOS sideband scales linearly with the amplitude of the terahertz field, $A_{THz} \propto \sqrt{P_{THz}}$, where P_{THz} is the total power of the terahertz field. Recall in section 4.5, we compared our experimental arrangement to that of [66], giving an estimate of the terahertz power in our work of $2.5 \mu\text{W}$. Given the 0.5 THz terahertz spectral bandwidth shown in figure 4.5 and the comb element spacing of $f_{rep} \simeq 104 \text{ MHz}$, one calculates a power per terahertz comb element of 0.3 nW for our apparatus.

Using this estimate of the terahertz power per comb element, we compare the signal to noise performance obtained by two works in particular. That of Bartels et al. (particularly [86], but see also [96]) and that of Barbieri et al. [97]. In [86], a total terahertz power of $40 \mu\text{W}$ is claimed from an electro-optic antenna, giving a power per terahertz comb line of $\simeq 30 \text{ nW}$. These authors use a similar detuned comb arrangement, acquiring many time-domain data-traces, each of approximately $100 \mu\text{s}$ duration. An average over $\simeq 10^7$ of these traces is then taken and Fourier transformed to allow the spectral content of the terahertz output to be analysed. This acquisition time corresponds to a range in pulse delay of 1 ns , as predicted by equation 6.1. This limited delay time gives rise to the frequency resolution of the experiment of 1 GHz , which meant that the authors were unable to resolve the individual comb lines of the terahertz spectrum, being themselves spaced by 1 GHz .

It is notable that such significant averaging was required, despite the higher power per terahertz comb line, due to residual instabilities in the locking scheme used to govern the repetition rate detuning of the two laser oscillators. From the measurements presented in section 6.3, we see that the residual timing jitter in our locking scheme is at least as good as that in [86] (the longer duration of our optical pulses prevents us from measuring any

6.5. Results and Conclusions from Dual-comb Spectroscopy Measurement

lower levels of timing jitter). However, we note that the larger repetition rate of [86] lessens the demand on the locking scheme, as the spacing of the rf heterodyne beats is increased. In the time domain, one can interpret this as an increase in sampling rate of the modulation due to the detuning of the two combs, which means that an average over a given number of traces is acquired over a shorter total acquisition time. For a total of 10^7 averages, Bartels et al. obtain a signal to noise ratio at line-centre of $\simeq 50$ dB. If one were to attempt a similar measurement with the 0.3 nW per terahertz comb line and 30 mW LO of our experiment, one would expect this to be reduced to 0 dB, highlighting the need for high-power combs with this technique.

Barbieri et al [97] demonstrated a mode-locked quantum cascade laser (QCL), producing 17 mW of total terahertz power at 13 GHz repetition rate over a narrow spectral bandwidth of 32 GHz. In this case, the terahertz spectrum contains only a few comb lines, giving a considerable average power per comb line of $\simeq 7$ mW. In contrast to Bartels et al. these authors acquired data in the frequency domain using a swept rf spectrum analyser with a resolution bandwidth of 100 kHz. In the work of Barbieri et al. the bandwidth of the lock used to control the repetition rate of the QCL was only a few hundred Hz. Such large resolution bandwidths and comparatively poor locking performance does not, in this case, affect the ability to resolve the individual terahertz comb lines due to the spacing of the latter by the large repetition rate. Barbieri et al. observe a signal to noise ratio of 20 dB for their experiment. Performing a similar comparison as that done for [86] above, one predicts a signal to noise ratio at terahertz line-centre of -55 dB for our power levels, due largely to the reduced terahertz power per comb line.

In order to increase the performance of the experimental arrangement presented in this thesis, there exists four options. Firstly, to reduce the residual relative timing jitter between the two optical pulse trains. The most likely method for achieving this would be to stabilise the relative pulse repetition rates at optical frequencies rather than at GHz frequencies, as discussed in section 6.2.1, and demonstrated in [94]. This requires considerable additional experimental complexity in the form of a high finesse

6.5. Results and Conclusions from Dual-comb Spectroscopy Measurement

optical reference cavity and CW laser sources, and was beyond the scope and resources of this project. The second possible option is to increase the pulse repetition rate of the fibre laser oscillators used, such that the comb line spacing is increased. Unfortunately, achieving pulse repetition rates greater than $\simeq 200$ MHz in fibre lasers involves significant engineering challenges due to the reliance of the nonlinear polarisation evolution modelocking mechanism on the induced birefringence of the fibre components [98]. The amount of polarisation rotation accumulated in a cavity roundtrip therefore decreases for higher repetition rate cavities, leading to instabilities in modelocking [99]. The third option for increasing the signal to noise ratio of the system presented here is to increase the power in the terahertz comb. The obvious way to achieve this is to increase the optical power with which the nonlinear generating crystal is pumped, requiring additional amplification stages in the fibre laser system, resources for which were not available. Finally, electro-optic antennas have demonstrated increased terahertz conversion efficiency at these powers. Indeed, Bartels et al. obtain their $40 \mu\text{W}$ of terahertz power from only a 500 mW optical pump. The trade off is saturation of the conversion efficiency for higher optical driving fields, and reduced terahertz spectral bandwidth owing to the time constants of the carrier dynamics within the crystal.

As a final area for improvement of the work presented in this thesis, we note that the magnitude of each term contributing to the rf photocurrent in equation 5.23 scales with the amplitude of two optical LO comb elements, $A_{LO}(\omega_M)$ and $A_{LO}(\omega_{M+N})$ for the SFG contribution and $A_{LO}(\omega_{M+2N+1})$ and $A_{LO}^*(\omega_{M+N+1})$ in the case of the DFG contribution. It was shown in section 5.6 that this gives rise to a scaling of the shot-noise-limited signal to noise ratio as $\propto P_{LO}$, in contrast to conventional heterodyne detection where one observes no benefit in terms of signal to noise ratio beyond the shot-noise-limit. It is worth noting that both of the works discussed above used greater LO powers, 400 mW in the case of [86] and 50 mW in the case of [97], than the 30 mW available for this work.

A final useful calculation is to estimate the signal to noise ratio expected in the dual-comb detection scheme from the measured performance of the

6.5. Results and Conclusions from Dual-comb Spectroscopy Measurement

single-comb detection scheme. The peak signal in figure 4.5a represents a voltage swing of 500 μV from the background-corrected mean value of zero. We assume the mechanical chopper to modulate the driving optical field with the form of a square wave, and that therefore the terahertz field also exhibits a square-wave modulation at the chopper frequency of $f_{\text{chop}} \simeq 1.5$ kHz. Considering a square wave as the sum of its Fourier components,

$$f(t) = \frac{4}{\pi} \sum_{n=1,3,5\dots} \frac{1}{n} \sin(n\omega t), \quad (6.6)$$

the 500 μV root-mean-square (rms) signal level measured at the fundamental chopping frequency corresponds to a peak-to-peak level of the total square wave signal of 900 μV . Further, the single-channel detector used in the acquisition of figure 4.5a had a power gain of 37.5 dB, and a transimpedance gain of 50 V/A, implying a photocurrent generated in the diode itself of approximately 340 nA. In the single-comb case, all of the rf heterodyne beat frequencies are mapped to an rf frequency of zero, and are therefore degenerate, by virtue of the zero value of Δf_{rep} . The resulting change in signal level is therefore due to the heterodyne beat frequencies from each of the $\simeq 5000$ THz rf comb elements summing at dc frequency. In the dual-comb case, where the non-zero detuning of the pulse repetition rates serves to lift the degeneracy and map each of the heterodyne beats to a unique rf frequency, each comb element is reduced in amplitude with respect to the single-comb case by, to a first order approximation, a factor given by the number of THz frequency comb elements. Using the above numbers, the photocurrent produced by each rf heterodyne beat is calculated to be 69 nA. Accounting for the transimpedance gain of 8000 V/A of the balanced detector shown in Appendix A, and feeding this signal through an rf power amplifier with 32 dB of power gain, this gives a signal level of 550 nV, or a power into a 50 Ω load of 9.5 pW, or -80 dBm. Significantly lower than the shot noise-limited noise floor of this balanced detector configuration, shown to be $\simeq -20$ dBm in figure 6.10. Due to the linear scaling of the signal strength with P_{LO} versus the scaling as $\sqrt{P_{THz}}$, the necessary 60 dB

6.5. Results and Conclusions from Dual-comb Spectroscopy Measurement

increase in signal strength is likely to be more readily obtained through increases in the local oscillator power. Indeed, achieving such an increase in signal strength through increases in terahertz comb powers alone would require an increase in P_{THz} of 12 orders of magnitude. Due to the large increases in signal required, it is highly likely that improvements will have to be made in all of the areas outlined above. That is, increases in both the local oscillator power and terahertz comb power, and a reduction in the relative timing jitter between the two laser pulse trains.

Consider now efforts to detect the expected heterodyne comb by providing an rf reference to an additional mixing stage, as described in section 6.4.2, where it was observed that the ability of the servo loop to track the laser repetition rate detuning was limited to a frequency bandwidth of $\simeq 6$ kHz, in contrast to loop bandwidths achieved elsewhere in our lab using the same design of voltage-controlled oscillator (VCO) and different loop architectures. Given sufficient time and resources, the components limiting this bandwidth could be identified and replaced and/or redesigned, and it is anticipated that the locking bandwidth of the VCO control loop could be increased to $\simeq 50$ kHz. Note however that this detection scheme inherently has the drawback of introducing additional instrumentation noise in the form of the noise floors of the components used, and that therefore, direct detection of the heterodyne beat is likely to offer the preferred solution.

A precise estimate of the benefit of these improvements, or indeed, an estimate of the necessary improvements required in order to attain a particular signal to noise ratio, is a difficult task owing to the complexity of the physical processes involved. Indeed, efforts to calculate the absolute terahertz power from the optical rectification process alone are rarely seen in scientific literature. Calculating the magnitude of the rf photocurrent from the asynchronous electro-optic sampling process is even more problematic due to the lack of numerical estimates of the nonlinear susceptibility at terahertz frequencies. In fact, it is possible that the technique presented here would allow such measurements in the future, with high spectral resolution.

Chapter 7

Final Conclusions

In this work, we have shown that significant technical challenges remain if a passive optical resonator is to be effective in increasing the efficiency of the nonlinear conversion process involved in terahertz generation via optical rectification. Namely, crystal materials must be developed that offer single pass conversion efficiencies comparable to those already available, but without the optical absorption observed for gallium phosphide. In the absence of such materials, high power terahertz frequency combs would therefore seem better served by conventional single-pass generation geometries. Such techniques may take better advantage of the long coherence lengths in readily available nonlinear materials at wavelengths that are conveniently produced by now well-established, high power fibre lasers.

We have shown analytically that asynchronous electro-optic sampling can provide a high-resolution terahertz frequency comb spectrometer. Further, we have derived the equations governing the resultant heterodyne comb using a fully frequency-domain analysis. To date, our experimental efforts to detect the expected heterodyne comb have been unsuccessful. This is in spite of the different detection geometries, large signal gain at the frequencies of interest, efforts to reduce noise on commercial electronics used, and considerable effort to stabilise the relative repetition rates of the two laser oscillators. The fact that, despite these measures, the heterodyne beat signal was still not observed only serves to highlight the need for high power frequency combs in this technique. However, in the course of this work other authors have detected similar heterodyne combs using higher power quantum cascade laser (QCL) terahertz sources. With the higher comb powers available with ever advancing fibre laser technology, this technique will likely warrant future interest for the purposes of high resolution terahertz spec-

troscopy, where the high cost and complex cooling of QCL terahertz sources cannot be justified.

Bibliography

- [1] Y Hu, XH Wang, LT Guo, and CL. Zhang. Terahertz time-domain spectroscopic study of carbon monoxide. *PubMed*, 26(6):1008–1011, 2006.
- [2] D.M. Mittleman, R.H. Jacobsen, R. Neelamani, R.G. Baraniuk, and M.C. Nuss. Gas sensing using terahertz time-domain spectroscopy. *Applied Physics B: Lasers and Optics*, 67:379–390, 1998. 10.1007/s003400050520.
- [3] Edward P J Parrott, J Axel Zeitler, Tomislav Fris, Michael Pepper, William Jones, Graeme M Day, and Lynn F Gladden. Testing the Sensitivity of Terahertz Spectroscopy to Changes in Molecular and Supramolecular Structure : A Study of Structurally Similar Cocrystals & DESIGN 2009. *Crystal Growth & Design*, 2009.
- [4] L. S. Rothman, I. E. Gordon, A. Barbe, Benner, P. F. Bernath, M. Birk, V. Boudon, L. R. Brown, A. Campargue, and J. P. Champion. The HITRAN 2008 molecular spectroscopic database. *Journal of Quantitative Spectroscopy and Radiative Transfer*, 110(9-10):533–572, June 2009.
- [5] P.H. Siegel. Terahertz technology. *Microwave Theory and Techniques, IEEE Transactions on*, 50(3):910 –928, mar 2002.
- [6] P.F. Taday, I.V. Bradley, D.D. Arnone, and M. Pepper. Using terahertz pulse spectroscopy to study the crystalline structure of a drug: A case study of the polymorphs of ranitidine hydrochloride. *Journal of Pharmaceutical Sciences*, 92(4):831–838, 2003.

- [7] Jeffrey Barber, Daniel E Hooks, David J Funk, Richard D Averitt, Antoinette J Taylor, and Dmitri Babikov. Temperature-dependent far-infrared spectra of single crystals of high explosives using terahertz time-domain spectroscopy. *The Journal of Physical Chemistry. A*, 109(15):3501–5, April 2005.
- [8] Feng Huang, Brian Schulkin, Hakan Altan, John F. Federici, Dale Gary, Robert Barat, David Zimdars, Minghan Chen, and D. B. Tanner. Terahertz study of 1,3,5-trinitro-s-triazine by time-domain and Fourier transform infrared spectroscopy. *Applied Physics Letters*, 85(23):5535, 2004.
- [9] Matthias Hoffmann, Bernd M. Fischer, and Peter U. Jepsen. Terahertz spectroscopy of rna and dna and spot array imaging. In *Optical Terahertz Science and Technology*, page WB2. Optical Society of America, 2005.
- [10] Paul A. George, Wallace Hui, Farhan Rana, Benjamin G. Hawkins, A. Ezekiel Smith, and Brian J. Kirby. Microfluidic devices for terahertz spectroscopy of biomolecules. *Opt. Express*, 16(3):1577–1582, Feb 2008.
- [11] P. Baron, J. Mendrok, Y. Kasai, S. Ochiai, T. Seta, K. Sagi, K. Suzuki, H. Sagawa, and Joachim Urban. AMATERASU: Model for atmospheric terahertz radiation analysis and simulation. *Journal of the National Institute of Information and Communications Technology*, 55:1, s. 109-121, 2008.
- [12] Wai Lam Chan, Jason Deibel, and Daniel M Mittleman. Imaging with terahertz radiation. *Reports on Progress in Physics*, 70(8):1325, 2007.
- [13] Herbert M Pickett and Dean B Peterson. Far-ir fabry-perot spectrometer for OH measurements. *Remote Sensing of Atmosphere Chemistry*, 1715:451–456 610, 1991.
- [14] Yihong Yang, Alisha Shutler, and D. Grischkowsky. Measurement of the transmission of the atmosphere from 0.2 to 2 THz. *Opt. Express*, 19(9):8830–8838, Apr 2011.

- [15] Benjamin S. Williams. Terahertz quantum-cascade lasers. *Nature Photonics*, 1:517–525, September 2007.
- [16] B.S. Williams, S. Kumar, Q. Hu, and J.L. Reno. High-power terahertz quantum-cascade lasers. *Electronics Letters*, 42(2):89 – 91, jan. 2006.
- [17] Mikhail A. Belkin, Federico Capasso, Feng Xie, Alexey Belyanin, Milan Fischer, Andreas Wittmann, and Jérôme Faist. Room temperature terahertz quantum cascade laser source based on intracavity difference-frequency generation. 92(20):201101, 2008.
- [18] D. H. Auston, K. P. Cheung, and P. R. Smith. Picosecond photoconducting hertzian dipoles. 45(3):284–286, 1984.
- [19] A. Bartels, A. Thoma, C. Janke, T. Dekorsy, A. Dreyhaupt, S. Winnerl, and M. Helm. High-resolution THz spectrometer with kHz scan rates. *Opt. Express*, 14(1):430–437, Jan 2006.
- [20] Georgi L. Dakovski, Brian Kubera, and Jie Shan. Localized terahertz generation via optical rectification in ZnTe. *Journal of the Optical Society of America B*, 22:1667, 2005.
- [21] Ajay Nahata, Aniruddha S Weling, and Tony F Heinz. A wideband coherent terahertz spectroscopy system using optical rectification and electro-optic sampling. *October*, 69(October):2321–2323, 1996.
- [22] Steven T Cundiff. Phase stabilization of ultrashort optical pulses. *Journal of Physics D: Applied Physics*, 35(8):R43, 2002.
- [23] Scott a Diddams, Leo Hollberg, and Vela Mbele. Molecular fingerprinting with the resolved modes of a femtosecond laser frequency comb. *Nature*, 445(7128):627–30, February 2007.
- [24] S Schiller. Spectrometry with frequency combs. *Optics letters*, 27(9):766–8, May 2002.
- [25] Julien Mandon, Guy Guelachvili, and Nathalie Picqué. Efficient Two-Comb Fourier Spectroscopy. pages 1–9, 2008.

- [26] A C Vutha, W C Campbell, Y V Gurevich, N R Hutzler, M Parsons, D Patterson, E Petrik, B Spaun, J M Doyle, G Gabrielse, and D DeMille. Search for the electric dipole moment of the electron with thorium monoxide. *Journal of Physics B: Atomic, Molecular and Optical Physics*, 43(7):074007, 2010.
- [27] J. J. Hudson, B. E. Sauer, M. R. Tarbutt, and E. A. Hinds. Measurement of the Electron Electric Dipole Moment Using YbF Molecules. *Phys. Rev. Lett.*, 89:023003, Jun 2002.
- [28] R Jason Jones and Jun Ye. Femtosecond pulse amplification by coherent addition in a passive optical cavity. *October*, 27(20):1848–1850, 2002.
- [29] Christoph Gohle, Thomas Udem, Maximilian Herrmann, Jens Rauschenberger, Ronald Holzwarth, Hans a Schuessler, Ferenc Krausz, and Theodor W Hänsch. A frequency comb in the extreme ultraviolet. *Nature*, 436(7048):234–7, July 2005.
- [30] R.W. Boyd. *Nonlinear Optics*. Electronics & Electrical. Academic Press, 2003.
- [31] M. Bass, P. A. Franken, J. F. Ward, and G. Weinreich. Optical rectification. *Phys. Rev. Lett.*, 9:446–448, Dec 1962.
- [32] X Zhanga and D H Auston. Optoelectronic measurement with femtosecond optics surfaces and interfaces. pages 326–338, 1992.
- [33]
- [34] Ajay Nahata, Aniruddha S. Weling, and Tony F. Heinz. A wide-band coherent terahertz spectroscopy system using optical rectification and electro-optic sampling. *Applied Physics Letters*, 69(16):2321–2323, 1996.
- [35] K. Kieu and F. W. Wise. All-fiber normal-dispersion femtosecond laser. *Opt. Express*, 16(15):11453–11458, Jul 2008.

- [36] M. Hofer, M. E. Fermann, F. Haberl, M. H. Ober, and A. J. Schmidt. Mode locking with cross-phase and self-phase modulation. *Opt. Lett.*, 16(7):502–504, Apr 1991.
- [37] E. Treacy. Optical pulse compression with diffraction gratings. *Quantum Electronics, IEEE Journal of*, 5(9):454 – 458, sep 1969.
- [38] R. L. Fork, C. H. Brito Cruz, P. C. Becker, and C. V. Shank. Compression of optical pulses to six femtoseconds by using cubic phase compensation. *Opt. Lett.*, 12(7):483–485, Jul 1987.
- [39] Miklos Stern, Jonathan P Heritage, and E W Chase. Grating compensation of third-order fiber dispersion. 2(12), 1992.
- [40] Oscar Eduardo Martinez. 3000 Times Grating Compressor with Positive Group Velocity Dispersion : Application to Fiber Compensation in 1.3-1.6 micron Region. *Quantum*, (1):59–64, 1987.
- [41] T. J. Hammond, Arthur K. Mills, and David J. Jones. Simple method to determine dispersion of high-finesse optical cavities. *Optics Express*, 17(11):8998, May 2009.
- [42] J. Z. Xu and X.-C. Zhang. Optical rectification in an area with a diameter comparable to or smaller than the center wavelength of terahertz radiation. *Opt. Lett.*, 27(12):1067–1069, Jun 2002.
- [43] P U Jepsen and S R Keiding. Radiation patterns from lens-coupled terahertz antennas. *Optics letters*, 20(8):807–9, April 1995.
- [44] Jesse Petersen. Terahertz generation via resonantly - enhanced optical rectification of ultrafast laser pulses. Internal Memo.
- [45] R. W. P. Drever, J. L. Hall, F. V. Kowalski, J. Hough, G. M. Ford, a. J. Munley, and H. Ward. Laser phase and frequency stabilization using an optical resonator. *Applied Physics B Photophysics and Laser Chemistry*, 31(2):97–105, June 1983.

- [46] B.E.A. Saleh and M.C. Teich. *Fundamentals of photonics*. Wiley series in pure and applied optics. Wiley-Interscience, 2007.
- [47] A.E. Siegman, M.W. Sasnett, and Jr. Johnston, T.F. Choice of clip levels for beam width measurements using knife-edge techniques. *Quantum Electronics, IEEE Journal of*, 27(4):1098–1104, apr 1991.
- [48] Jérôme Poirson, Fabien Bretenaker, Marc Vallet, and Albert Le Floch. Analytical and experimental study of ringing effects in a fabry–perot cavity. application to the measurement of high finesses. *J. Opt. Soc. Am. B*, 14(11):2811–2817, Nov 1997.
- [49] H. Bach and N. Neuroth. *The Properties of Optical Glass*. Schott Series on Glass and Glass Ceramics. Springer, 1995.
- [50] Micheal Thorpe, R Jones, K Moll, Jun Ye, and Ramin Lalezari. Precise measurements of optical cavity dispersion and mirror coating properties via femtosecond combs. *Optics express*, 13(3):882–8, March 2005.
- [51] Albert Schliesser, Christoph Gohle, Thomas Udem, and Theodor W Hänsch. Complete characterization of a broadband high-finesse cavity using an optical frequency comb. *Optics express*, 14(13):5975–83, July 2006.
- [52] P. Deus, U. Volland, and H. A. Schneider. Thermal expansion of GaP within 20 to 300 K. *physica status solidi (a)*, 80(1):K29–K32, 1983.
- [53] C.B. de Araujo and H. Lotem. New measurements of the two-photon absorption in GaP, CdS, and ZnSe relative to Raman cross sections. *Physical Review B*, 18(1):30, 1978.
- [54] Isao Tomita, Hiroyuki Suzuki, Hiroshi Ito, Hirokazu Takenouchi, Katsuhiko Ajito, Rakchanok Rungsawang, and Yuko Ueno. Terahertz-wave generation from quasi-phase-matched GaP for 1.55 μm pumping. *Applied Physics Letters*, 88(7):071118, 2006.
- [55] WC Dash. Intrinsic optical absorption in single-crystal germanium and silicon at 77 K and 300 K. *Physical Review*, 99, 1955.

- [56] Pallab Bhattacharya. *Semiconductor Optoelectronic Devices*. Prentice Hall, 2, illustr edition, 1997.
- [57] PJ Dean and DG Thomas. Intrinsic Absorption-Edge Spectrum of Gallium Phosphide. *Physical Review*, 150, 1966.
- [58] Japan Manufacturer's Society of Compound Semiconductor Materials (JAMS-CS). EPD measurements for low dislocation density GaAs and InP substrates. *III-Vs Review*, 12(6):32 – 37, 1999.
- [59] M Beaudoin, A J G Devries, S R Johnson, H Laman, and T Tiedje. Optical absorption edge of semi-insulating GaAs and InP at high temperatures. *Semiconductors*, 70(June):3540–3542, 1997.
- [60] M. Theuer, D. Molter, K. Maki, C. Otani, J. a. Lhuillier, and R. Beigang. Terahertz generation in an actively controlled femtosecond enhancement cavity. *Applied Physics Letters*, 93(4):041119, 2008.
- [61] Fabian D. J. Brunner, Arno Schneider, and Peter Gunter. Velocity-matched terahertz generation by optical rectification in an organic nonlinear optical crystal using a Ti:sapphire laser. *Applied Physics Letters*, 94(6):061119, 2009.
- [62] Jun Takayanagi, So Kanamori, Koji Suizu, Masatsugu Yamashita, Toshihiko Ouchi, Shintaro Kasai, Hideyuki Ohtake, Hiromasa Uchida, Norihiko Nishizawa, and Kodo Kawase. Generation and detection of broadband coherent terahertz radiation using 17-fs ultrashort pulse fiber laser. *Optics express*, 16(17):12859–65, August 2008.
- [63] F O Ilday, H Lim, J R Buckley, and F W Wise. Practical all-fiber source of high-power, 120-fs pulses at 1 micrometre. *Optics letters*, 28(15):1362–4, August 2003.
- [64] C K Nielsen. Using photonic bandgap fibers for dispersion control and pulse compression. *Optics Express*, 14(13):4368–4373, 2006.

- [65] Guoqing Chang, Charles J. Divin, Chi-Hung Liu, Steven L. Williamson, Almantas Galvanauskas, and Theodore B. Norris. Power scalable compact THz system based on an ultrafast Yb-doped fiber amplifier. *Opt. Express*, 14(17):7909–7913, 2006.
- [66] Guoqing Chang, Charles J Divin, Jun Yang, Malakeh a Musheinish, Steven L Williamson, Almantas Galvanauskas, and Theodore B Norris. GaP waveguide emitters for high power broadband THz generation pumped by Yb-doped fiber lasers. *Optics express*, 15(25):16308–15, December 2007.
- [67] H. Bethe. Theory of Diffraction by Small Holes. *Physical Review*, 66(7-8):163–182, October 1944.
- [68] J Z Xu and X-C Zhang. Optical rectification in an area with a diameter comparable to or smaller than the center wavelength of terahertz radiation. *Optics letters*, 27(12):1067–9, July 2002.
- [69] Paul D. Cunningham, Nestor N. Valdes, Felipe a. Vallejo, L. Michael Hayden, Brent Polishak, Xing-Hua Zhou, Jingdong Luo, Alex K.-Y. Jen, Jarrod C. Williams, and Robert J. Twieg. Broadband terahertz characterization of the refractive index and absorption of some important polymeric and organic electro-optic materials. *Journal of Applied Physics*, 109(4):043505, 2011.
- [70] Q Wu and X Zhang. Free-space electro-optic sampling of terahertz beams. 67(September):3523–3525, 1995.
- [71] Akhlesh Lakhtakia and Tom G Mackay. Electrical control of the linear optical properties of particulate composite materials. *Proceedings of the Royal Society A: Mathematical, Physical and Engineering Science*, 463(2078):583–592, 2007.
- [72] D. F. Nelson and E. H. Turner. Electro-optic and Piezoelectric Coefficients and Refractive Index of Gallium Phosphide. *Journal of Applied Physics*, 39(7):3337–3343, 1968.

- [73] R. CLARK JONES. A new calculus for the treatment of optical systems. *J. Opt. Soc. Am.*, 31(7):500–503, Jul 1941.
- [74] M Brunken and H Genz. Electro-Optic Sampling at the TESLA Test Accelerator : Experimental Setup and First Results. *TESLA Report*, 2003-11:1–24, 2003.
- [75] H. J. Bakker, G. C. Cho, H. Kurz, Q. Wu, and X.-C. Zhang. Distortion of terahertz pulses in electro-optic sampling. *Journal of the Optical Society of America B*, 15(6):1795, June 1998.
- [76] Q Wu and X Zhang. Free-space electro-optics sampling of mid-infrared pulses. *Society*, 71(September):1285–1286, 1997.
- [77] P Kaufmann. Uncooled Detectors of Continuum Terahertz Radiation. *Spectrum*, 10(1):288–294, 2011.
- [78] Matthias C Hoffmann, Ka-Lo Yeh, János Hebling, and Keith a Nelson. Efficient terahertz generation by optical rectification at 1035 nm. *Optics express*, 15(18):11706–13, October 2007.
- [79] Yihong Yang, Alisha Shutler, and D Grischkowsky. Measurement of the transmission of the atmosphere from 0.2 to 2 THz. *Optics express*, 19(9):8830–8, May 2011.
- [80] A. Bartels, A. Thoma, C. Janke, T. Dekorsy, A. Dreyhaupt, S. Winnerl, and M. Helm. High-resolution THz spectrometer with kHz scan rates. *Optics Express*, 14(1):430–437, January 2006.
- [81] Fritz Keilmann, Christoph Gohle, and Ronald Holzwarth. Time-domain mid-infrared frequency-comb spectrometer. *Opt. Lett.*, 29(13):1542–1544, Jul 2004.
- [82] Q. Wu and X.-C. Zhang. Free-space electro-optics sampling of mid-infrared pulses. *Applied Physics Letters*, 71(10):1285–1286, 1997.
- [83] a Bartels, R Cerna, C Kistner, a Thoma, F Hudert, C Janke, and T Dekorsy. Ultrafast time-domain spectroscopy based on high-speed

- asynchronous optical sampling. *The Review of scientific instruments*, 78(3):035107, March 2007.
- [84] Albert Schliesser, Markus Brehm, Fritz Keilmann, and Daniel van der Weide. Frequency-comb infrared spectrometer for rapid, remote chemical sensing. *Opt. Express*, 13(22):9029–9038, 2005.
- [85] S. Reinhardt, E. Peters, T. W. Hänsch, and Th. Udem. Two-photon direct frequency comb spectroscopy with chirped pulses. *Physical Review A*, 81(3):1–5, March 2010.
- [86] A. Bartels, A. Thoma, C. Janke, T. Dekorsy, A. Dreyhaupt, S. Winnerl, and M. Helm. High-resolution THz spectrometer with kHz scan rates. *Optics Express*, 14(1):430–437, January 2006.
- [87] Stefano Barbieri. Coherent sampling of active mode-locked terahertz quantum cascade lasers and frequency synthesis. *Nature Photonics*, 5(5):306, 2011.
- [88] Alexander Sell, Rudiger Scheu, Alfred Leitenstorfer, and Rupert Huber. Field-resolved detection of phase-locked infrared transients from a compact Er: fiber system tunable between 55 and 107 THz. *Applied Physics Letters*, 93(25):251107, 2008.
- [89] G. Gallot and D. Grischkowsky. Electro-optic detection of terahertz radiation. *J. Opt. Soc. Am. B*, 16(8):1204–1212, 1999.
- [90] P.C.D. Hobbs. *Building Electro-Optical Systems: Making It All Work*. Wiley Series in Pure and Applied Optics. Wiley, 2009.
- [91] Fatih Ö. Ilday and Frank W. Wise. Nonlinearity management: a route to high-energy soliton fiber lasers. *Journal of the Optical Society of America B*, 19(3):470, March 2002.
- [92] D Strickland and G Mourou. Compression of amplified chirped optical pulses. *Optics Communications*, 56(3):219–221, 1985.

- [93] E.D. Palik. *Handbook of Optical Constants of Solids*. Number v. 1 in Handbook of Optical Constants of Solids. Academic Press, 1985.
- [94] Ian Coddington, William Swann, and Nathan Newbury. Coherent Multiheterodyne Spectroscopy Using Stabilized Optical Frequency Combs. *Physical Review Letters*, 100(1):11–14, January 2008.
- [95] R.C. Dorf and R.H. Bishop. *Modern Control Systems*. Pearson Prentice Hall, 2008.
- [96] G Klatt, R Gebs, C Janke, T Dekorsy, and a Bartels. Rapid-scanning terahertz precision spectrometer with more than 6 THz spectral coverage. *Optics express*, 17(25):22847–54, December 2009.
- [97] Stefano Barbieri, Marco Ravarò, Pierre Gellie, and Giorgio Santarelli. Coherent sampling of active mode-locked terahertz quantum cascade lasers and frequency synthesis. *Nature Photonics*, 5(April), 2011.
- [98] M Hofer, M E Fermann, F Haberl, M H Ober, and a J Schmidt. Mode locking with cross-phase and self-phase modulation. *Optics letters*, 16(7):502–4, April 1991.
- [99] F Ilday, J Chen, and F Kärtner. Generation of sub-100-fs pulses at up to 200 MHz repetition rate from a passively mode-locked Yb-doped fiber laser. *Optics express*, 13(7):2716–21, April 2005.

Appendix A

Technical Information Regarding High Gain, Low-pass Filtered, Balanced Detector for Detection of the Heterodyne Beat in the Dual-comb Spectrometer Setup

Below is the circuit schematic for the high-gain, balanced photodetector used for detection of the heterodyne beat in the dual-comb terahertz spectrometer experiment. The detector provides strong attenuation of frequencies above 80MHz, as shown in figure 6.10. This circuit was designed and built by Pavel Trochtchanovitch at the University of British Columbia Department of Physics Electrical Shop specifically for this application.

Appendix A. Data for Bandwidth-limited Balanced Detector Used for Detection of Heterodyne Beat

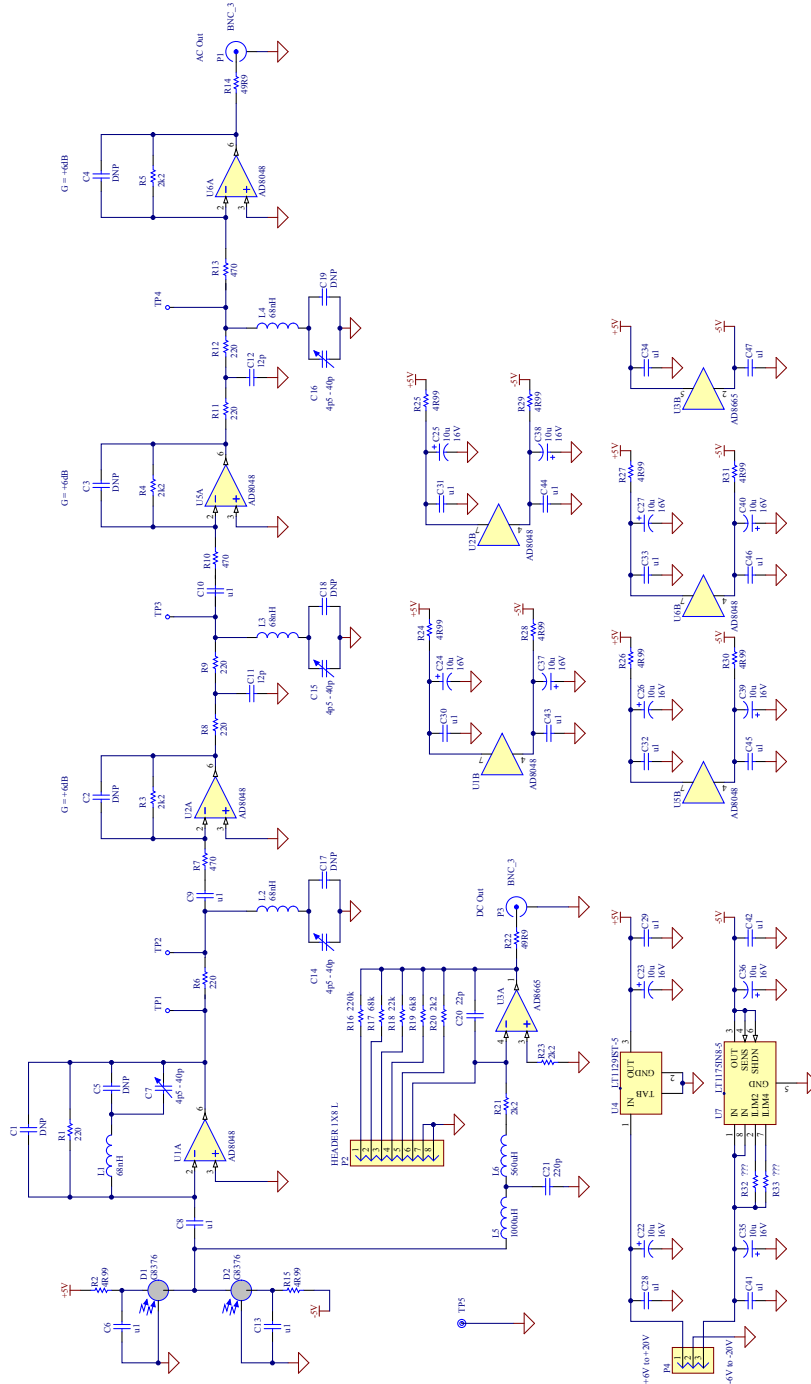


Figure A.1: Circuit schematic of the custom-designed, bandwidth-limited balanced photodetector. 189